Politechnika Poznańska

Wydział Budowy Maszyn i Zarządzania

Katedra Zarządzania i Inżynierii Produkcji

MASTER THESIS

Testing of materials dedicated for manufacture of a presurgical 3D model of a temporal bone with the use of Rapid Prototyping techniques

Beata WYSOCKA

Biomedical engineering

Medical and Rehabilitation devices

Supervisor:

Ph.D., B.Eng. Filip Górski

Poznań 2019

MIEJSCE NA KARTĘ PRACY DYPLOMOWEJ

I would like to express my sincere gratitude to the Promoter Ph.D., B.Eng. Filip Górski

for his scientific care, kindness and time devoted to me,

which contributed to the creation of my thesis.

Spis treści

Abstract

The paper presents a methodology for finding and testing material intended for the creation of a temporal bone model using additive manufacturing techniques. The model is intended for the pre-surgical training of surgeons. The bibliography contains information about the anatomy and diseases of the temporal bone and the ear, surgeries, and otological training. Also besides, it contains research on rapid prototyping methods, commercially available temporal bone models and mechanical tests performed on bone models. At the beginning of the methodological part, the research plan and requirements regarding the bone model were presented. Then, the right technology and the material for the temporal bone model were selected. Compression and drilling tests were carried out on samples manufactured using the chosen technology and the material to find its mechanical properties test cutting parameters. In the next stage, the behavior of the tested material was analyzed. Its properties were compared with the cortical temporal bone to verify the degree of recreation of the mechanical response of the material concerning for human bone.

Streszczenie

W pracy przedstawiono metodotykę znalezienia i testowania materiału przeznaczonego do stworzenia modelu kości skroniowej z wykorzystaniem technik wytwarzania przyrostowego. Model przeznaczony jest do przedoperacyjnego treningu chirurgów. Bibliografia zawiera informacje na temat anatomii, chorób kości skroniowej i ucha oraz operacji i treningu otologicznego. Ponadto zawiera badania związane z metodami szybkiego prototypowania, komercyjnie dostępnymi modelami kości skroniowej i testami mechanicznymi przeprowadzanymi na modelach kości. Na początku części metodologicznej przedstawiono plan badań i wymagania dotyczące modelu kości. Następnie wybrano odpowiednią technologię i materiał do modelu kości skroniowej. Testy ściskania oraz wiercenia przeprowadzono na próbkach wydrukowanych przy użyciu wybranej technologii i materiału w celu ustalenia jego właściwości mechanicznych i zbadania paramterów skrawania. W kolejnym etapie przeanalizowano zachowanie badanego materiału. Jego właściwości porównano z korową kością skroniową w celu zweryfikowania stopnia odtworzenia odpowiedzi mechanicznej materiału w stosunku do kości ludzkiej.

1. Introduction

Surgery requires skills that the surgeon can acquire during the proper practice. The golden standard for the education of surgeons is the study of human cadavers. Before 1992, there was no law for the use of cadavers for research, but now the access to them is limited and not available for everyone. Currently, the training models are supplemented by advanced physical and virtual simulators, allowing for unlimited practice in a repetitive and normalized environment [1, 2].

The use of additive manufacturing technologies (known popularly as 3D printing) to create a pre-operative temporal bone model is becoming increasingly popular. Models are based on medical imaging data, coming from CT and MRI. 3D printing is used in medicine due to many benefits. This does not require changing the machine between different products and allows for easier creation of personalized products. In addition, this technique is characterized by high accuracy of products and relatively short manufacture time [1].

Various tests are performed in both quasi-static and dynamic conditions to determine mechanical parameters such as elastic modulus, tensile and compression strength, flexural strength, density or hardness. In addition, it is important to examine the thermal response of the material, because the temperature can cause a variety of risks and complications. On the models of the temporal bone, such operations as drilling or milling with a special otic-drill are performed. When creating surgical simulators, the material response to these processes should be estimated and compared to the real bone response [3].

The mechanical properties of bones depend on many parameters, such as age, location, patient's history, type of loads it has been subjected to and many more. For this reason, while creating the temporal bone model, it is necessary to consider materials that have the most similar properties to this skull bone. The type of specimens taken from real human bones is also important, they can be samples of the cortical bone, the cancellous bone or sandwich structures containing both tissues. It depends on the purpose of the simulator to be created and on what structures it is supposed to reproduce [4].

Temporal bone models for surgical training are becoming more and more common and allow to improve the skills and confidence of surgeons taking into account difficult cases. Therefore, it is necessary to constantly search for new solutions to adapt the model to the real mechanical properties of human bone.

2. Aims and scope of work

The general objective of the work was to find the material intended to produce a model of a temporal bone additive manufacturing techniques, which reproduces the behavior of a real human bone as closely as possible, taking into account both the visual aspect and the mechanical response.

Specific aims include:

- review of literature on the properties of the temporal bone,
- review of literature on available 3D printing technologies and 3D printing materials in relation to the properties of human bones,
- finding the right technology for printing the multi-material temporal bone model,
- finding the right material for printing the multi-material temporal bone model,
- performing mechanical tests on samples of selected material and examination of its mechanical properties,
- comparing the mechanical properties of the selected material with temporal bone properties.

The work was carried out under the project "Development and validation of a new 3D artificial model of the temporal bone for otologic surgery training" on Ecole Nationale d'Ingénieurs de Metz and under supervision with Dr Cécile Parietti-Winkler.

3. Literature analysis

3.1. Otology

3.1.1. Ear anatomy

The ear is the organ of hearing and balance, which can be subdivided into the inner, middle and outer ear, separated from the middle by the tympanic membrane (Figure 3.1) [5].

The external ear can be divided into the ear and the auditory canal. The auricle consists of an irregularly shaped plaque with fibrous-elastic cartilage, which is covered by the skin. The auricle is supplied with blood vessels originating from the posterior auricular and superficial temporal arteries. Main nerves are the great auricular, supplies the cranial surface and the posterior part of the lateral surface and auriculotemporal nerves [5, 6].

The external auditory canal is also divided into two parts. Its length is about 2-3 cm for adults and runs from the auricle to the tympanic membrane The tympanic membrane is a thin, transparent structure about 1 cm in diameter with an oval shape and it is covered by thin skin and internally through the mucous membrane [5, 6].

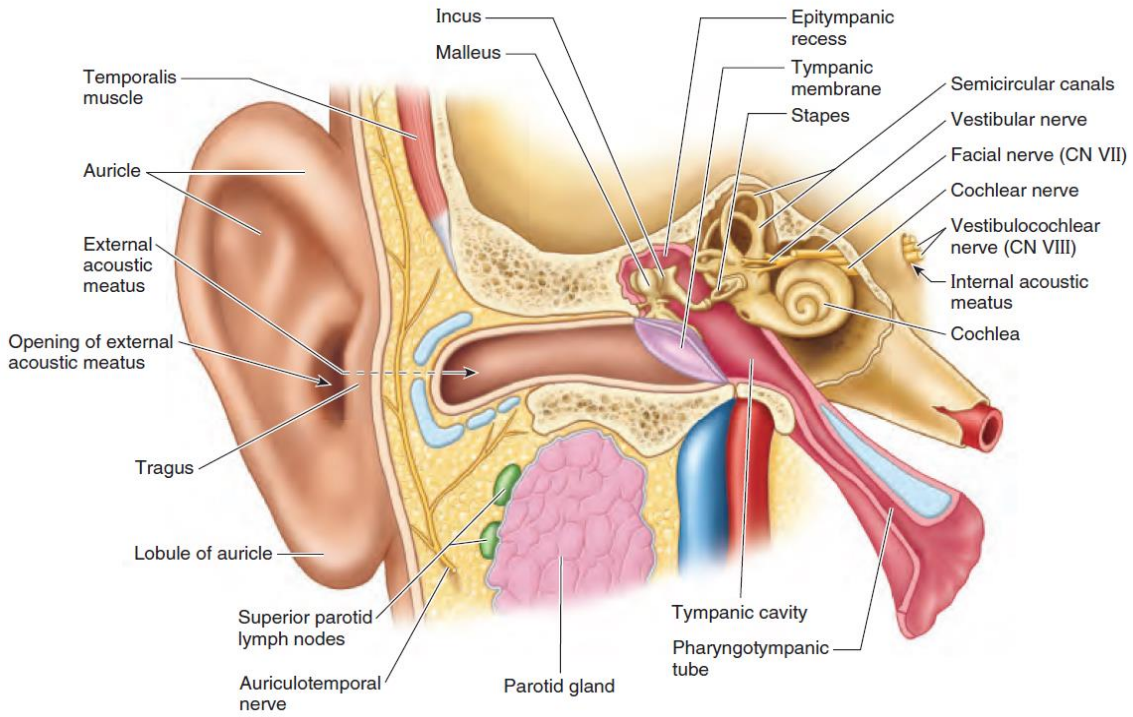

Figure. 3.1. Parts of the ear in the anterior view. A coronal section of the ear, with an accompanying orientation figure [5]

The middle ear is separated from the outer ear through the tympanic membrane and connects to the nasopharynx through the pharyngotympanic tube. The middle ear consists of auditory ossicles, stapedius, and tensor tympani muscles, tympanic plexus of nerves and Chorda tympani nerve (Figure 3.2). It is separated from the ear canal of the outer ear by the tympanic membrane [5, 6].

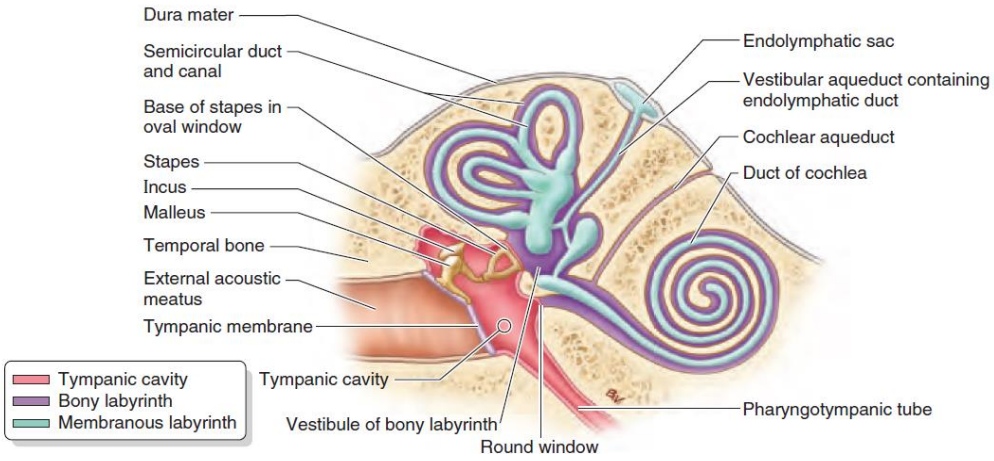

Figure. 3.2. Oblique section of the petrous temporal bone - the middle and internal parts of the ear [5]

The tympanic cavity includes elements such as auditory ossicles, their joints and ligaments, tendon of tensor tympani muscle, arteries and tympanic veins. It has six walls. In addition, it also contains ramus of the internal carotid artery, tympanic plexus, and nerves, lesser petrosal nerve and air. Pharyngotympanic tube, otherwise known as the auditory tube, connects the tympanic cavity with a cavity of the pharynx [5, 7].

Through the tympanic cavity passes the mobile chain created from three auditory ossicles. These ossicles are formed of dense bone and covered with mucous membrane. The malleus is attached to the tympanic membrane and consists of head, neck and handle. The next in the order between malleus and stapes is the incus, which consists of a body lying in the epitympanic recess and a short and long limb. The stapes consist of a base, a head, and a front and posterior limb. It is the smallest of the ossicles, and its base is much smaller than the tympanic membrane [5, 6].

The inner ear has a vestibulocochlear organ and it includes a bone labyrinth and a membranous labyrinth. The bony labyrinth consists of the vestibule, cochlea, and three

semicircular canals, which are located inside the otic capsule. The cochlea is the front part of the labyrinth, its core is the modiolus, around which the spiral of the canal of the cochlea is wrapped. The cochlea has the shape of a shell and contains the cochlear duct. The membranous labyrinth consists of semicircular ducts, utricle, saccule, endolymphatic duct, urticulosaccular duct, connecting cord, and cochlear duct. The main artery of the inner ear is a labyrinthine artery [7].

3.1.2. Ear pathologies

The anatomy could be distorted in either the external, middle or inner ear or, indeed, in all three in the same patient. Ear anomalies may occur spontaneously or in connection with other abnormalities that are associated with genetics [6, 8].

One of the most popular problems in the case of the external ear is an accessory skin tag, resulting from an abnormal fusion of the tubercles, which form a pinna. One of the more aesthetic problems is protruding ears. Another is dysplasia of the ear, which consists of the irregularity of shape and size caused by deformation of the cartilage scaffold. Three degrees of dysplasia is distinguished, and the treatment consists of the reconstruction of the pinna [6, 9].

Middle ear anomalies can be unilateral or bilateral and may be broadly classified into minor and major or into three degrees [9].

The diseases associated with the eardrum include myringitis or acute, traumatic perforation of the eardrum, which may be due to indirect or direct wounds. Another disorder of the middle ear is otosclerosis, the disease of the bony labyrinth with inflammatory resorption and bone remodeling. One of the inflammation is catarrhal sterile otitis media with the serous, mucosal exudate to the tympanic cavity or otitis media acute. The most frequently described inflammation is chronic otitis media (COM) and two forms are distinguished: otitis media mesotympanalis and otitis media epitympanalis called cholesteatoma. Chronic otitis media epitympanalis also occurs in dry and wet form and is the proliferation of squamous epithelium with damage to the bone ear of the middle ear, the structure of the inner ear and can reach up to the mastoid or skull base. The cholesteatoma is defined as an abnormal growth of the skin in the middle ear space behind the plane of the eardrum. Another disease of the middle ear is mastoiditis with stagnant purulent content that can lead to ostitis and bone damage. Other pathologies are dehiscence or displacement of the facial nerve, pneumatised mastoid, missing antrum and aberrant courses of arteries and veins [6, 7, 9].

The ear pathologies of the inner ear are hearing loss, inflammation or toxic otitis media. Deafness can also be caused by toxic otitis media, for example through antibiotics, cytostatics or even diuretics or by noise. In the case of noise, the higher the energy and its rapid increase, the more likely it is mechanical damage. This damage can be divided into chronic or acute, including acute acoustic trauma, explosive injury or acute hearing loss [6].

3.2. Otologic Surgery

3.2.1. Surgical procedures

Otologic surgery is used to treat various ear disorders such as otitis media, vertigo, conductive hearing loss or sensorineural hearing loss. One of the most common surgical interventions is placing a tube for otitis media, while the most popular disorders that require a surgeon's intervening are cholesteatoma and chronic serous otitis media (CSOM). Both diseases are treated using mastoidectomy [10].

Ear surgery is very complicated, which is why neuro-otologists have to cooperate with neuroradiologist who is able to identify radiological abnormalities in the anatomy of the temporal bone and its adjacent areas. The next task is to choose the right approach by the surgeon to the middle ear and base of the skull. This approach depends on the planned surgery and its purposes. A big difficulty during surgery is the position of the patient, who usually lies flat on the back with the head turned to the inoperable side and the fact that the surgeon is forced to move the microscope around the ear, which changes its direction and angle of a view (Figure 3.3) [9, 10, 11].

Fig. 3.3. Operating table with the patient [11]

The otological instrumentation is very important in temporal bone surgery. The operating room (OR) must be properly equipped and be sterile. The equipment includes an operating table where the surgeon must feel comfortable. In addition, each OR has a wall suction with all necessary tools and tubes, an electrocautery equipment, a surgical drill, and a microscope, which should be mobile [11].

Tympanoplasty is a laryngological operation whose aim is to improve hearing by recreating the sound conduction path in the middle ear, i.e. eliminating the perforation. Tympanic Membrane (TM) perforation leads to loss of hearing by disrupting the conversion of acoustic sound entering the external auditory canal into mechanical energy. This change is created by the movement of the ossicles that work with the tympanic membrane. In order for a patient to be qualified for surgery, certain criteria have to be met, for example, a patient to be free from infection and when in his case conservative medical treatment is not possible. The tympanoplasty treatment is also indicated for active people, in whom the use of water precautions affects their quality of life [9].

Tymplanoplasty usually consists of the reconstruction of the tympanic membrane (myringoplasty) and the ossicular chain (ossiculoplasty) (Figure 3.4). There are various types of surgical approach depending on the case of injury. One of them is the transcanal approach, which is performed for small perforations within the entire external auditory canal. Another example used most often in Europe is the endaural approach, in which the canal incision to the helical root is extended during the procedure. Its advantage is the possibility of using for all sizes of perforation if the pathology is not associated with other complications such as mastoid disease [9, 12].

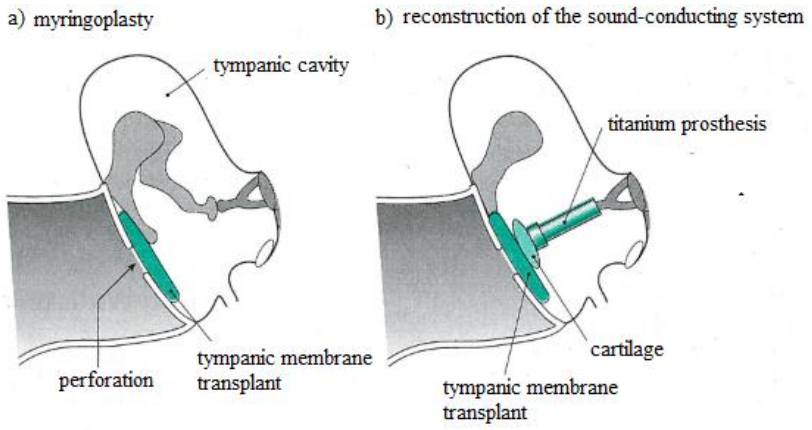

Fig. 3.4. Tympanoplasty: a) myringoplasty: placement of a transplant under the tympanic membrane, b) reconstruction of the ossicular chain: titanium prosthesis and preserved stapes [12]

The postauricular approach of allowing access to the anterior tympanic membrane through the incision in the postauricular sulcus is also performed with all types of perforations. Tympanoplasty can be combined with the mastoidectomy procedure, for example in the case of diseases such as chronic otitis media or cholesteatoma in the mastoid or attic [9].

Mastoidectomy involves removing the part of the temporal bone in the lateral base of the skull. The anatomical structures adjacent to the temporal bone are accessed through the entrance to the internal auditory auditory canal. There are different variants of approaches to surgery, but the most common is the translabyrinthine approach, where access is obtained by entering labyrinth [13, 14].

Mastoidectomy allows for the treatment primarily of diseases such as otitis media, cholesteatoma or facial nerve schwannoma. In cholesteatoma, this treatment is indicated during the mastoid involvement. There are “canal wall up” or “canal wall down” mastoidectomy depending on whether there drilled down. The canal wall down technique is preferred when mastoid is very narrow with sparse pneumatization and if there is no ventilation in the mastoid cavity may be expected. The operation consists in opening the mastoid process and removing its contents. To gain access to anatomic structures adjoining the temporal bone, the entrance to the internal ear canal is made [6, 9, 13].

Tympanomastoidectomy is the removal of the patient's tissue through surgical drilling of temporal bone fragments. Caution is very important because of the risk of damage to vital structures found in the temporal bone, such as the facial nerve. The facial nerve may also disintegrate which has been investigated in one of the experiments. Cholesteatoma changes normal anatomy and increases the risk of iatrogenic injury. According to histological and anatomy studies, up to 25% to 57% of cases are related to facial nerve dehiscence [6, 13, 15].

Under the typical surgeon procedure, see the operating area via a stereoscopic microscope and operate a high-speed burr, cutting the bones. In addition, the surgeon uses suction cups to remove excess water [14].

Stapes surgery is surgery with much more risk than other middle ear surgery due to the fact that the inner ear space is open (Figure 3.5). Then, the loss of hearing and deafness after surgery is more productive, so the surgeon must know very well the anatomy and the distances between the structures of the inner ear. The stapes piston cannot be inserted deeper than 0.5 mm from the vestibule. In the event that the piston meets the macula organs, the patient may suffer from abrupt vertigo [9].

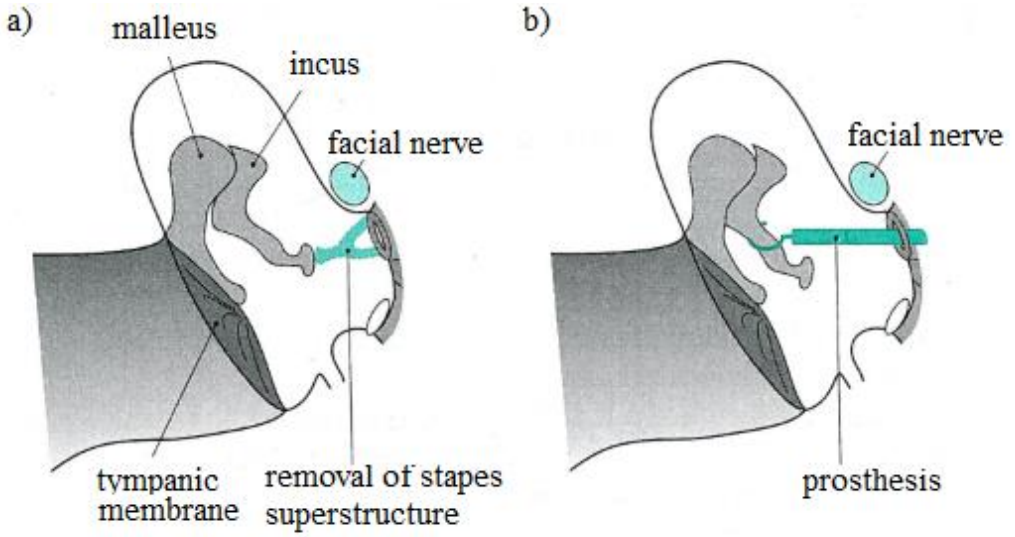

Fig. 3.5. Stapendostomy: a) removing the stapes superstructure and making an opening in the stapes plate, b) putting on a prosthesis [12]

During the procedure, it is always possible to refreeze and dislocate the stapes, which is a big obstacle during the operation. Also during this procedure damage to the facial nerve can occur, which is sometimes not covered by the bone in its canal. The soft structure around the operating area is treated as a nerve until it is proven otherwise. The theory is used for preventive purposes [9].

3.2.2. Surgical training

The anatomy of the temporal bone is very complex, and its understanding is very important for otolaryngologists and medical personnel who are involved in the treatment of hearing loss. The three-dimensional structure of bones is complicated, which is why learning on the basis of literature is not enough. The golden standard for the education of surgeons is the study of human cadavers [2, 16].

There are newer methods of otological surgeries, such as endoscopic ear surgery (EES). In this technique, surgeons use straight and angled endoscopes for middle ear visualization rather than a microscope (Figure 3.6). For endoscopic operations, there are not many options for ear training. An alternative approach is to supplement a realistic, high-quality preparation derived from cadaver with surgical task training. Such training models promote the acquisition of basic skills and hand-eye coordination with 2-dimensional visualization via efficient, repetitive practice. Studies clearly show that medical students without prior surgical

experience statistically significant improvement in performing tasks on an EES skills trainer following a repetitive practice. In some exercises, some students were able to get even an expert level by the end of the training [17, 18].

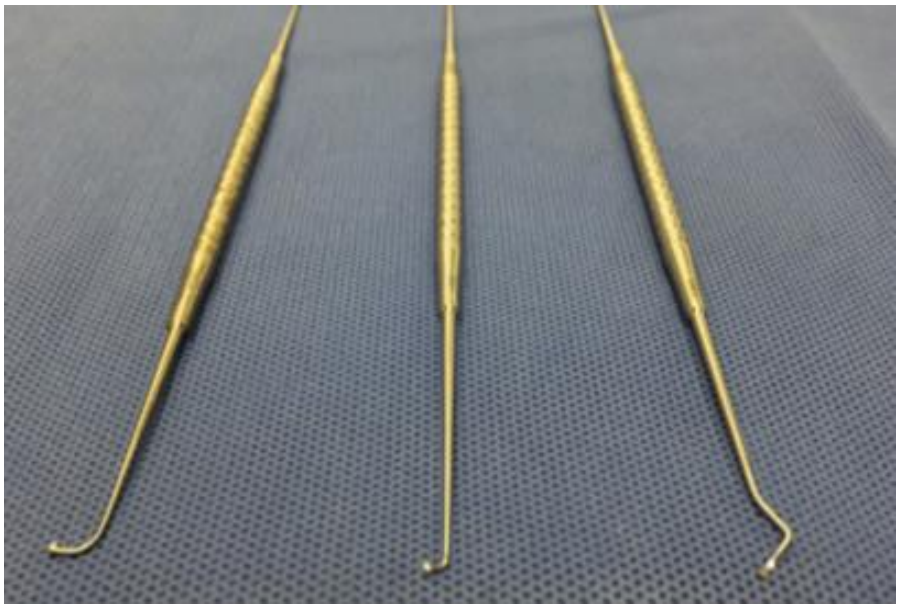

Fig. 3.6. Basic EES instruments: Curette (left) and short and long Thomassin dissectors [18]

There are various types of simulators in otology. They are divided into physical or virtual reality simulators (VR). Simulators should imitate various surgical techniques and the environment present during the procedure [19].

Physical simulators are models that imitate specific parts of the body. They can be directly touched, cut, drilled, manipulated and modified and are used in various fields of medicine, including otolaryngology. One of the most common treatments practiced by the novice group is myringotomy and an ear tube placement. Typically, simple physical models are used for the exercises, which are composed of cheap and available parts, such as syringes imitating the external auditory canal or gloves for the tympanic membrane [19].

Models for ear surgery are more difficult to do because the anatomy is very complex and complicated. Various bone models have been modified to allow for such procedures as stapedotomy, grommet insertion, ossiculoplasty, stapes surgery or tympanostomy [19].

An example of a physical temporal bone model is Pettigrew, which takes into account the ossicles, has marked landmarks and provides feedback and irrigation or suction. In addition, it contains a red irrigation fluid imitating blood, but its disadvantage is a bad inaccurate facial nerve. Another example is the model designed by Mori et al., which in addition to surface

elements, air cells, and inner bone structures includes cranial nerves, internal carotid artery, dura mater or venous sinuses [19, 20].

Another example of the temporal bone model for surgical training is the TF-ba model produced by PHACON (Figure 3.7). Human scans of the temporal bone with the use of micro-CT were used for its creation. The three-dimensional model of the bones was 3D printed from the casting powder using the binding agent in the appropriate concentration. The physical simulator was created layer by layer, and in the meantime, colors were added that formed different structures, helping to distinguish them. In an empty structure such as the mastoid process, the powder was removed, and structures such as arteries and nerves were manufactured as channels and filled with wires in different colors. To imitate the tympanic membrane and the dura mater, silicone was used and the ossicles were cast as a rigid and continuous structure. In addition to the TFba model, PHACON offers various models of temporal bone such as TF-bo, TF-bp, TF-bar, TF-ban, and others, which differ from each other in a slight way, for example, the material used for production [21, 22].

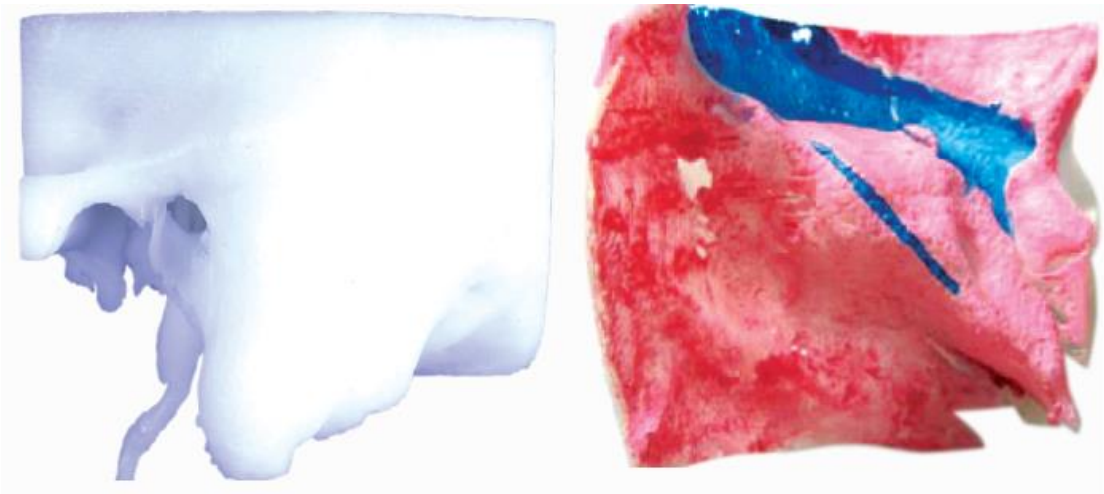

Fig. 3.7. PHACON model of the temporal bone [22]

The next model of the physical temporal bone model is the TEMP'OS model created by the French company COLLIN (Figure 3.8). It is a synthetic bone manufactured using an additive technique on a 1:1 scale that takes into account both the middle and the inner ear structures. In this case, colors were also used to mark the appropriate anatomical elements [23].

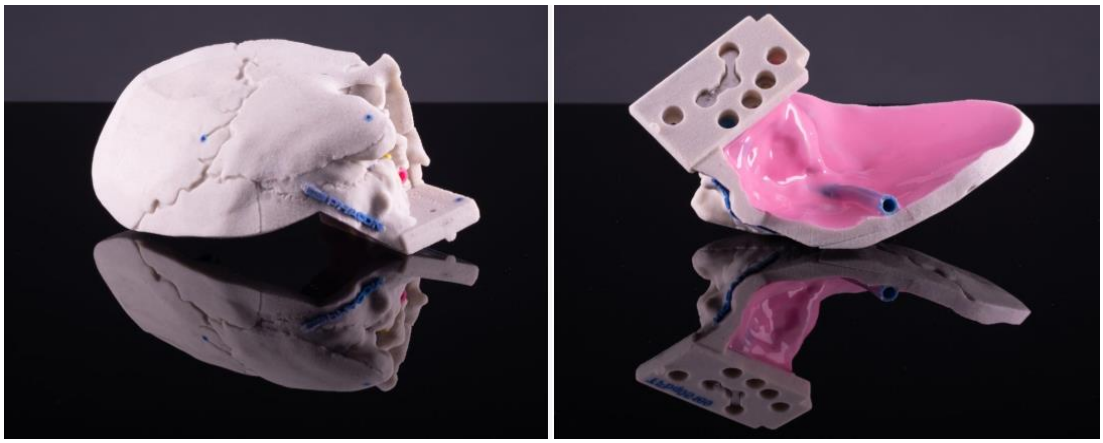

Fig. 3.8. TEMP'OS COLLIN model of the temporal [23]

Temporalogix also offers three-dimensional models for the training of otological surgeons (Figure 3.9). The company produces right and left-sided models based on the bone of a 10-month-old child or an adult. The next company which offers the Temporal bone models is the Japan company KEZLEX [24, 25].

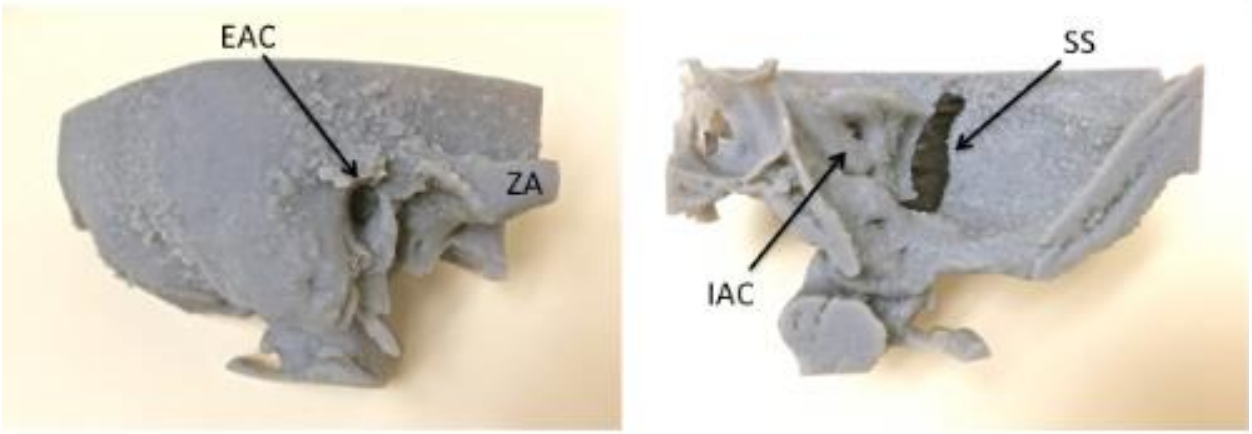

Fig. 3.9. Temporalogix temporal bone model [24]

Physical simulators have many advantages and are therefore easily available for training purposes. They are inexpensive and are easy to assemble and maintain. They can be made of various materials to manipulate their hardness. In addition, in more advanced technologies, they can be equipped with electronics and feedback. However, the models still have many disadvantages associated with perfect reproduction, in particular, mechanical properties. Therefore, except for commercially available products, many institutes and universities produce their own models looking for the optimal solution. Only a few manufacturers provide prices for their simulators. The price of the Phacon physical simulator varies between

120-750 € depending on the detail of the model. The most expensive transparent simulator of this company costs up to 1790 euros. For example, the price of the Pettigrew physical model is around 71 to 77 euros [19, 24, 26].

In otolaryngology, virtual reality simulators can include two-dimensional or three-dimensional surgical environments, and provide a computer-generated environment that has anatomical visual representations. The originator of the application of virtual reality (VR) simulation in surgical training was first proposed by Satava et al. in 1993. Surgical training through repetitive, proctored sessions has been shown to improve the detection and analysis of surgical errors [19, 27].

Haptic simulation allows for the three-dimensional representation in a real-time, thanks to which a user who sees graphic representations of the temporal bone has the ability to feel it using a manipulator held in the hand like an otic-drill. The end of the manipulator imitates the tip of the drill, so when the bone is drilled, the deeper structures appear in sequence. This allows familiarizing with the entire surgical procedure, which ensures the acquisition of self-confidence and the learning of interaction between the bone and the drill. An additional advantage of virtual simulators with the feedback is an auditory input, which makes the experience even more realistic. The advantages of this kind of simulators are the lack of consequences in the error mistake, the possibility of repeating the procedure, the lack of biological materials or a wide range of different anatomical variants [19, 28].

The most known virtual simulators of the temporal bone are VOXEL-MAN Temposurg, Mediseus, Ohio State University simulator and Stanford surgical simulator [19].

The VOXEL-MAN Temposurg developed at the University of Hamburg uses an absolute resolution of volume images of the temporal bone (Figure 3.10). During exercises, the user is equipped with specialized glasses that allow a 3D vision and controls the virtual drill with a foot pedal. The simulator uses a volumetric cutting method so that real-time drilling changes the appearance of the temporal bone. A virtual otoscope drilling works on the basis of the haptic feedback so that the user feels pressure changes from the cut the bone material. It is also possible to adjust the direction of the drill and an angle of the view and a magnification [28].

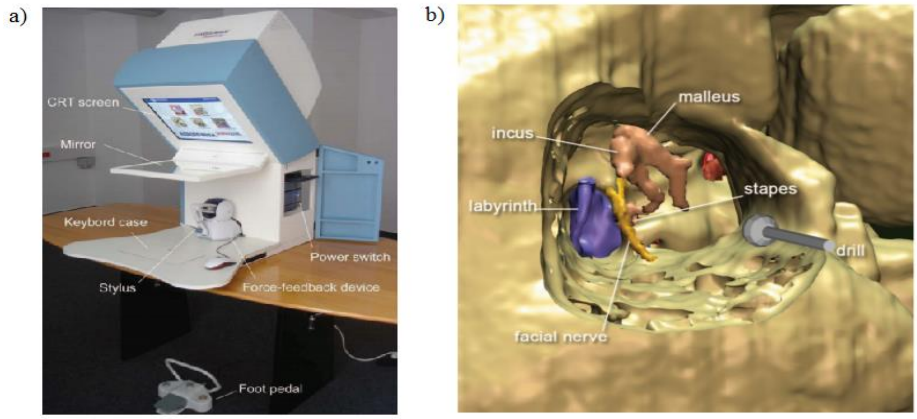

Fig. 3.10. a) The Voxel-Man TempoSur, b) The image provided by the Voxel-Man TempoSurg is modified in real-time as the operator drills [28]

The Mediseus simulator consists of a microscope with two projected images slightly offset, which creates a three-dimensional environment (Figure 3.11). The bone model was created on the basis of CT scans and it is possible to change such properties as color or hardness. Zhao et al. have checked the application of the Mediseus Surgical Drilling Simulator (SDS), examining the effect of the training on simulators on the level of surgical experience. The study included 27 people, had to perform a part of the mastoidectomy operation. The results showed that the experts completed the simulation by 23 minutes faster than novices and 8 minutes earlier than the residents. The strength dredged on the bone model by the novice group resulted in damage to critical structures. Research confirms that both novices and experts training on virtual simulators of the temporal bone allows improving skills, and thus reduce the risk of making a mistake during a real operation [19, 29].

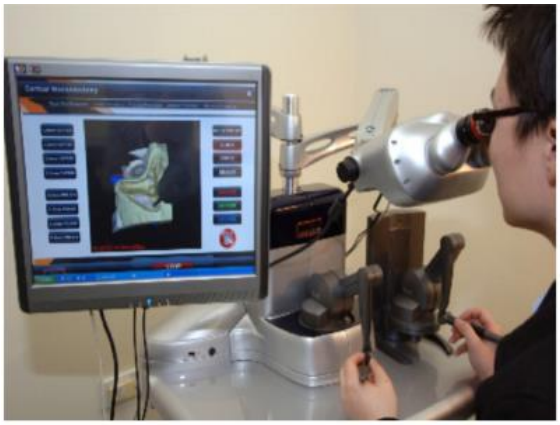

Fig. 3.11. Photograph of Mediseus temporal bone simulator showing the viewing screen, simulated microscope, and two haptic devices in use [29]

3.3. Bone

3.3.1. Composition and mechanical properties of the bone

Bone tissue consists of water, organic and inorganic phases. The inorganic phase is defined as the contaminated form of calcium phosphate, called hydroxyapatite. The organic phase consists of 90% of collagen type I and other types of collagen, such as type III and IV. In addition, it contains bone sialoprotein (BSP) and non-collagen protein. Collagen is made of long fibers collected in bunches and arranged in layers according to the direction of operation of the greatest mechanical loads to which the bone is subjected [4, 30].

Bone tissue on a micron-scale is a hierarchical composition which at the level of about 0.1 μm is a mineralized composite of collagen fibers. On a scale of 1 to 10 μm, filaments are arranged in two forms. Primary lamellar bone is a tissue that consists of concentric rings of lamellae (Figure 3.12). The most common type of cortical bone is the Havers bone. The main units of the cortical bone are osteons, which undergo a bone remodeling process. This layer, called a thin cement line, has a low content of minerals and collagen. The bone matrix consists of a woven and lamellar bone [4, 30].

The bone tissue also contains osteoclasts, bone-derived cells that originate from pluripotent bone marrow cells. On a scale of 1 to 5 mm, there are two types of bone, the cortical and the trabecular bone. The cortical bone is a tightly packed Haversian canal, the lamellar or the woven bone, while the trabecular bone is highly porous cellular solid [30].

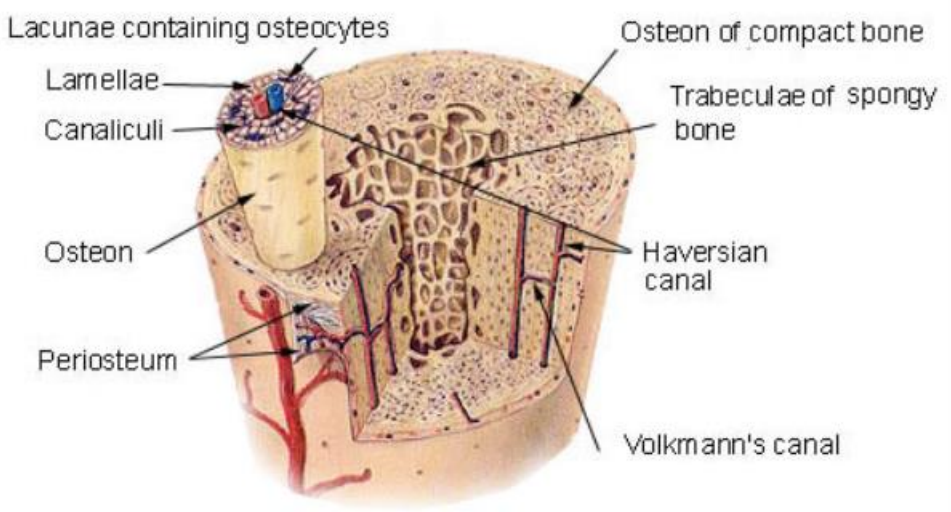

Fig. 3.12. Compact bone tissue [31]

The temporal bone contains both the cortical bone and the spongy bone, which can be seen on the CT image in Figure 3.13. In the design of the temporal bone model, the focus was on finding a material imitating the cortical bone, which is why the mechanical properties of this bone are important during the research [5].

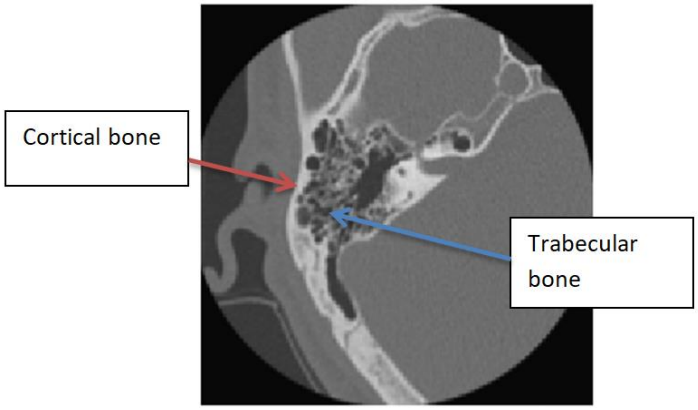

Fig. 3.13. CT image of the temporal bone with the selection of cortical and trabecular bone [5]

The internal architecture of the cortical bone varies depending on many factors. For example, there is a difference between the architecture of the "primary" lamellar bone and the lamellar bone built from secondary osteons, which is much weaker. In addition, the primary compact bone can consist of two nonlamellar tissue types. In cortical bone, anisotropy is determined by an osteonal orientation, and the solid matrix dominates the space (Figure 3.14). The principal direction of osteons in every type of compact bone is along the bone axis. Since elastic and strength properties of human cortical bone are anisotropic, it is stronger and stiffer in the case of a longitudinal load along the axis of the diaphyseal axis in comparison to the circumferential or radial transverse directions. The cortical bone can be treated as transversely isotropic and in this case, there are smaller differences in strength and the module between the circumferential or radial direction. In addition, the cortical bone is stronger during compression than in tension. The ratio of strength-to-modulus in percentages is 1.12 for longitudinal compression and 0.78 for tension [4, 32].

From a qualitative point of view, the cortical bone is a material that is elastically linear, which means that after exhibiting a marked yield point it is failed at relatively small loads. During bone loading to its yield point and then unloaded, only small permanent residual strains occur. The cortical bone exhibits viscoelastic behavior. However, the loading rate has a moderate impact on the module and the strength. In addition, mechanical properties are degraded just like damaging the material. After loading beyond the yield point, unloading and

reloading, the module has a lower value. Sometimes, when determining bone properties, it is necessary to consider its heterogeneity depending on porosity or percentage mineralization. Modeling the bone is difficult due to its constant rebuilding and the large dependence of many different parameters. From the general perspective, it is assumed that the mechanical behavior of the bone corresponds to the behavior of the fiber-reinforced composites [4, 32].

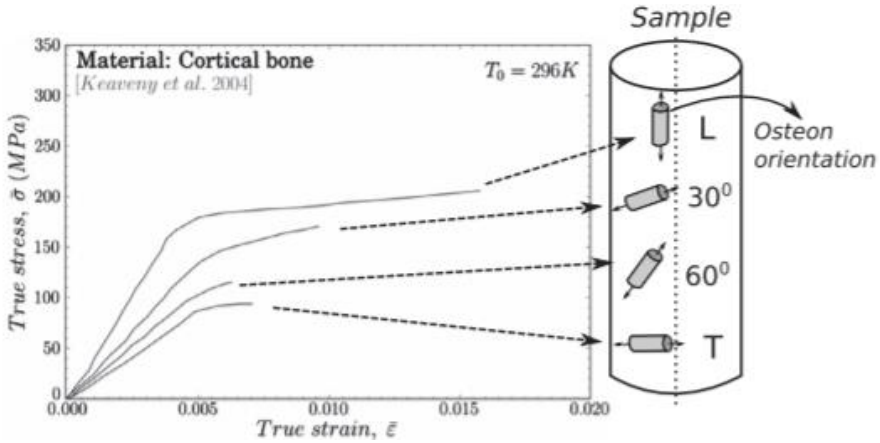

Fig. 3.14. Influence of osteon orientation on the mechanical behavior of the cortical bone [33].

3.3.2. Anatomy of the temporal bone

The temporal bone has a complex anatomy, and there are many important structures in its neighborhood, such as the internal carotid and middle meningeal arteries or various types of nerves (Figure 3.15). Four parts are distinguished in the temporal bone: squamous part, mastoid part, tympanic part and petrous part [7, 34].

In the squamous part, there is the temporal surface, in the back of which is a groove for the middle temporal artery and the cerebral surface. The mastoid part is located backward from the external auditory canal and prolongs in the mastoid process. The posterior mastoid part contains mastoid foramina, which has a mastoid branch of an occipital artery and a mastoid emissary vein. The tympanic part is located forward of the mastoid part and back and below the rocky part, and this part constitutes the front, bottom, and part of the back wall of the external acoustic meatus. From the back, this part is limited by a tympanomastoid fissure, through which the articular branch of a vagus nerve passes. The petrous part is in the shape of a pyramid in which apex, base, anterior, posterior and a bottom wall, anterior, posterior and upper border can be distinguished. The petrous part contains most of the major

nervous and vascular structures and compartments, including the carotid artery, jugular fossa and internal auditory canal [6, 7].

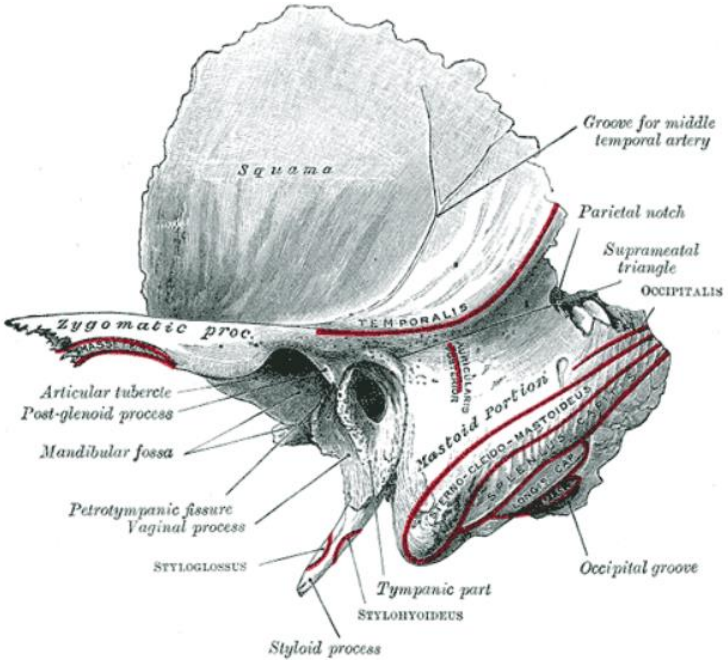

Fig. 3.15. The temporal bone [7]

3.3.3. Mechanical properties of the cortical temporal bone

The main requirement regarding the 3D model of the temporal bone is to reproduce as much as possible the anatomy and mechanical properties of the real temporal bone.

Knowledge of the mechanical properties of the bone allows conducting research to find the material that imitates it. The properties of models intended for the training of surgeons should be as close as possible to the properties of real human bones. The mechanical properties of bones of great importance in the process of creating the temporal bone model are mainly elastic modulus, tensile strength, ultimate strength, yield strength, and hardness. The values of these mechanical properties are usually examined by researchers in skull bones tests. The tests are performed on different samples including cortical bone, trabecular bone or skull composite being a combination of both bones [35-42].

It is very difficult to find tests to check the properties of the temporal bone because most of them involve examination of the entire skull or other bone of the skull. For this reason, the research was carried out for various bones of the skull, focusing as much as possible on the temporal bone. In addition, it is difficult to specify the values of mechanical parameters,

because they largely depend on the bone location, age of the donor, conditions of conservation.

Elastic modulus is one of the most important properties. An attempt to determine this parameter has been made by researchers from Dallas, J. Peterson and P. C. Dechow, whose aim was to investigate the variability of mechanical properties of cylindrical samples from the periosteal cortex of the cranial vault bones (Figure 3.16). The minimum and maximum stiffness axes in the cortical plane were determined and this was done experimentally by passing longitudinal ultrasound waves using piezoelectric transducers through each cortical specimen in nine directions with 22.5° intervals. The research was carried out in three directions due to bone anisotropy. As on a clock face, the orientation line and arrow were aligned, which was drawn on each specimen prior to bone core removal, in the direction of 12:00. Directions 1 and 9 were 180° apart, represented the same orientation, but with the emitting and receiving ultrasonic transducers reversed in position. The direction E3 has been set for the axis in which the obtained stiffness was maximum, while the direction E1 for the minimum stiffness. The direction E2 is the value between E1 and E3. The elastic constants were determined using ultrasonic velocity measurements taking into account the measurements of a series of transverse wave velocities and longitudinal velocities by the thickness of the cortex. The relationship between the material properties of the sample and the determined velocities on the basis of the linear elastic wave theory based on Hooke's law was determined. In their studies, they proved that the density of the temporal bone was the highest of all measured skull bones and was equal to 1,868 g/cm³ [35].

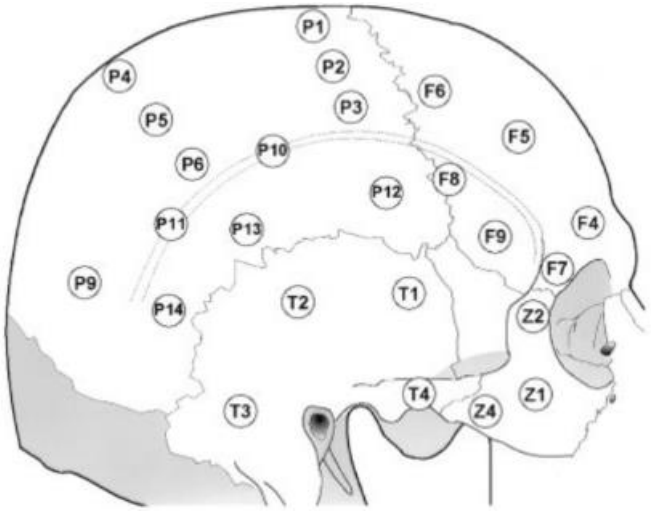

Fig. 3.16. Location of sites on the parietal, frontal, temporal, occipital, and zygomatic bones [35]

The values of Elastic modulus varied depending on the direction and the largest was for the direction of E3, and the smallest was E1. For the temporal cortical bone, the values of this parameter in direction E1, E2 and E3 were 13.4, 14.0 and 23.4 GPa, respectively. The value of anisotropy (E2 / E3) was 0.62 GPa [35].

The Elastic modulus of the left and right temporal bone was examined by J. Rahmoun et al., who included both cortical bone and spongy bone. They performed the three-point bending tests on prismatic samples and the results showed that the Elastic modulus for the left temporal bone is 5990.36 and the right 5221.69 MPa [36].

Similar tests using the three bending test were performed by R. Delille et al., who also examined the bones of the skull, treating them as a composite consisting of the cortical and trabecular bone. Their research included 19 samples taken from 20 human skulls and two samples from each skull were taken from the temporal bone. The mean value of Young's modulus for the temporal bone was 11.316 GPa [37].

Dynamic tests on the skull bones to obtain mechanical properties were performed in 1971 by J. L. Wood, examining the samples collected from the compact layers of the temporal, frontal and parietal human bone. Based on the data from the tension tests, it has been concluded that the elastic modulus of the skull bones varied from 10 to 22 GPa. The strain rates considered in this study ranged from 0.005 to 150 s^{-1}. Based on the flexure study on the "sandwich" structure of the bone, which Hubbard realized, it was found that the bones of the skull have a viscoelastic nature and the elastic modulus of parietal bone is equal to 9.5 GPa [38].

In this study of M. T. Davis et al., 47 samples from one six-year-old human cranium were tested to failure. The test was performed at strain rates approximately 0.045, 0.44, and 2.2 s^{-1} with some variation due to the variation in specimen size. They have examined in the four bending tests that the value of the effective modulus of elasticity of the cortical bone was equal to 9.87±1.224 GPa. These studies concerned the frontal and parietal regions in the six-year-old cranium [39].

Another important aspect in the process of creating a prototype of the skull bones is a load which it is able to endure (bear). Earlier, the aforementioned Jack L. Wood in his studies of stretching the samples from the cortical bone of the skull also determined the ultimate stress which ranged from 48.26 to 127.55 MPa [38].

James H. McElhaney et al., performed tests of compression and tension of specimens taken from the skull bone for the cortical bone, the diploë, and the composite. In this study,

the primary source was embalmed cadavers from which 17 entire calvariums have been obtained. The compression test was performed on the cuboid specimens at a constant velocity of 0.254 mm/min. The value of the ultimate strength in tension for the compact bone is 79.29 MPa and for the composite 43.44 MPa. For comparison, the value of the ultimate strength in compression was 96.53 MPa. The stiffness modulus in the tensile test was also determined for the cortical bone and was equal to 1.23 GPa [40].

Mechanical properties in tensile and compressive tests of the right parietal bone were also measured by F.G. Evans and H.R. Lissner. The average ultimate tensile strength of the compact bone was 70.53 MPa, while the average ultimate compressive strength was 152.24 MPa [41].

Research conducted by Hubbard showed that the flexural strength of the cranial bones is 82.00 ± 25.50 MPa. In the work of L. Falland-Cheung et al. the tensile strength of the skull bones is estimated at 67.73 ± 17.80 MPa. Bending tests were also performed on the human infant skull, taking into account the parietal and occipital bone. The mean value of the ultimate stress of the parietal bone was 23.1 ± 9.4 MPa, which is much lower than the results in the above-described studies. This show how important is the age of stiffness and endurance of the examined skulls. Unfortunately, it is problematic to find the yield strength value for the cortical bone of the skull, because this parameter has been measured for other human bones such as the femur and additionally the number of tests is limited [42, 43].

One of the articles in which the value of yield strength for the cortical bone was quoted was the work of J. Peterson et al., in which the study was conducted based on Finite Element Model of the part of a skull. For their model of the skull for cortical bone, they took the value of this parameter equal to 220 MPa [35, 44].

Table 4.2 (chapter 4.3.1) presents a summary and average values of all the mechanical parameters described above.

3.4. Drilling and milling processes

3.4.1. Drilling and milling definitions

Drilling is a method of chip machining, using tools called drills characterized by the fact that the main motion is rotational movement of the tool or workpiece and the feed motion - rectilinear motion, which can also be performed by the tool or workpiece (Figure 3.17b). The direction of the feed motion is parallel to the axis of the drill, which is

also the axis of the hole being made. Drilling can be carried out on a variety of technological machines such as drills, lathes and milling machines and machining centers [45].

Milling is a method of chip machining characterized by the fact that a multi-edged tool, called a milling cutter, performs a rotary motion, and the feed motion most often performs the workpiece, less often the tool (Figure 3.17a). Motion feeder can be straight or curvilinear. This process, the tool blades cut only on the part of the cutter's circumference, which means that cutting with individual blades is cyclically interrupted. Depending on the position of the milling cutter axis, peripheral milling, face milling, and bevel milling are distinguished in relation to the machined surface. Depending on the combination of main and feed motion, milling divided into concurrent and counter-rotating [45].

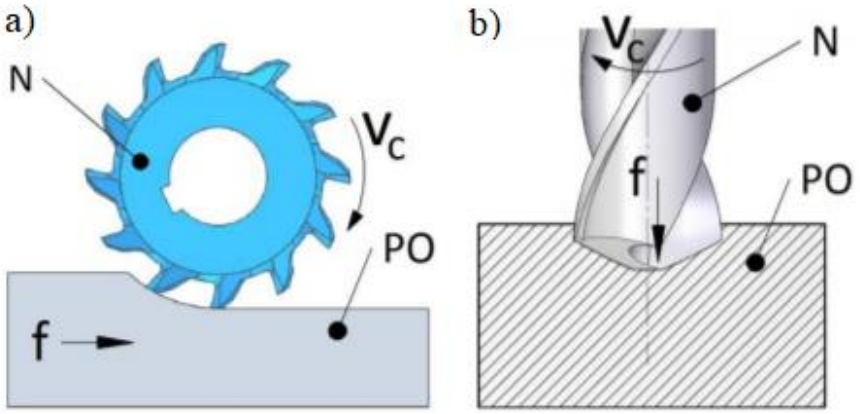

Fig. 3.17. Main motion v_c and feed f during a) circumferential milling, b) drilling [45]

3.4.2. Drilling and milling in technology and medicine

Definitions of the technical point of view were presented earlier. As can be noticed, the processes differ significantly and the purpose of the subtractive manufacturing gives different effects. In the area of Otolaryngology, the process of temporal bone milling is colloquially called drilling. The surgeon during the operation of all processes using a drill on the bone is called “drilling”, no matter how the bone is machined. This is problematic for engineers describing tests performed on bone samples or bone simulating materials. Some articles describe the real process of drilling a sample and then this does not lead to problems with understanding. However, in most articles and works where mechanical properties and haptic feedback were checked with the involvement of surgeons who performed the operation on the model, it was also called drilling, although it is actually a milling process. For example,

C. Santiuste et al in his work of studying the effect of anisotropy in cutting cortical bone uses the term "drilling", despite the fact that they actually did milling [33].

In the further part of the work, when presenting previously performed tests, only the word "drilling" to name both processes to be consistent with the authors is used. However, during the tests, both processes are distinguished and performed in accordance with the engineering definitions.

3.4.3. Drilling and milling tests in the bone

In orthopedic surgeries, bone drilling is a frequent procedure, which is why it is so important to investigate its impact on models. An important aspect is that the drilling process be clean and the holes are so arranged that they do not damage the surrounding important structures. Large forces and torques are generated during drilling, which can cause fracture of the drill and adverse histological effects. In spite of this, uncontrolled forces and heat generated during drilling may damage the surrounding tissue or lead to cracking [46].

In ear surgery, an otological drilling machine is the most important tool used during surgery (Figure 3.18). It requires the surgeon a high precision and coordination of the feet and hands. The operated area in the otological surgeon is often bent, and the anatomical structures are distorted by the disease, so that slipping the drill can lead to damage to important structures in the temporal bone such as the facial nerve, semicircular canal, sigmoid sinus or cochlea Drilling errors include such phenomena as slipping of the drill, entangled cotton swab in the high-speed rotating drill bit or drilling of unsuitable bone tissue wall [47, 48].

Fig. 3.18. The drilling process in otologic surgery [47]

One of the first bone drilling experiments involving the determination of drilling conditions and the geometry of drills suitable for surgery began already at the end of the 1950s. Among other things, the impact of the drill spindle speed on torque and thrust force, the influence of the drilling point angle on forces were investigated. The rake angle, flute geometry, and web thickness were analyzed for the geometry of the drill. Many conclusions from the research were made, but they were not fully functional in relation to the impact of drilling conditions on drilling forces. However, there are two important facts in the literature that drilling in the bone produces micro-scale fractures, and the bone's mechanical properties depend on strain, temperature, and strain rate. It has also been found that the characteristics of the formation of cracks are similar to those observed during shearing of polymers or metals [46].

Analysis of forces acting on the drill was developed by P. Sheng et al. (Figure 3.19). The drill during the operation rotates around its axis and moves along the bone. The surgeon exerts on the drill forces in two directions through the sleeve and the stem tools. One of the forces is perpendicular and the other F2 parallel to the bone, and in addition to the bone is also exerted by the reaction force F_{b1} and the friction force F_{b2} on the drill bit. The rotating drill generates the rise of driving torque T_m, which results in a resistance torque T_b on the drill bit [47].

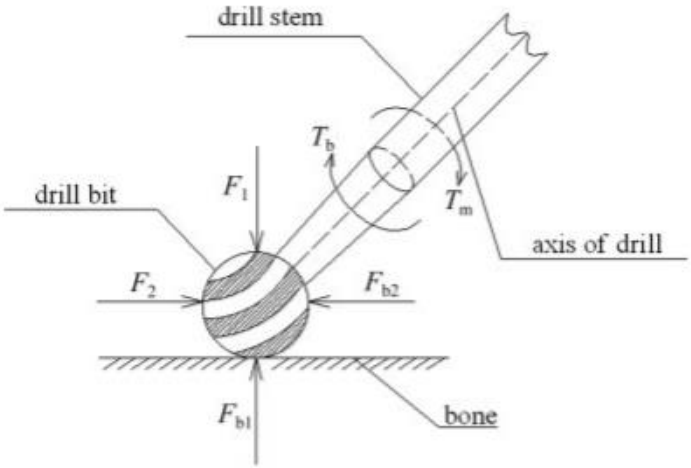

Fig. 3.19. The forces acting on the drill bit [46]

In the study, P. Sheng et al. the FACRI otologic drill was modified by equipping it with four different sensors and designed with and a new sleeve (Figure 3.20). One of the sensors was a force sensor consisting of four pieces of a strain gauge, whose task was to detect the

strain of the sleeve reflecting the forces. In addition, a current and voltage and velocity sensor consisting of a Hall effect element of eight Anico magnets were attached to the drill. The same authors, based on previous studies, have been constructing another modified otologic drill. This time they equipped it with three sensors: a force, current and voltage sensor. In addition, as before, a new sleeve was designed. In their research, they included three different drilling faults, and to integrate characteristic signals a multi-sensor information system was designed based on three back propagation (BP) neural networks presented in a "binary tree" structure [47, 48].

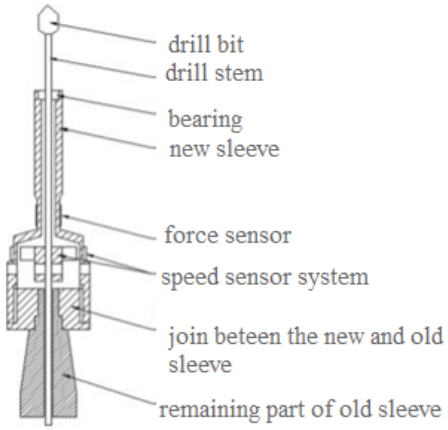

Fig. 3.20. Design drawing of sensor installation [48]

Based on their research, it can be said that the drill floats in two states, stable and unstable. An unstable state occurs when a drilling mistake occurs and the operator loses its axis. It has been difficult to apply a force sensor because the drill rotates at high-speed forces cannot be measured directly. In addition, obtaining a full picture of the operating conditions is possible with the use of a current, voltage and speed sensor, due to the possibility of interaction of varying forces with certain variables [47, 48].

The bone drilling process was also examined by W. Wang et al., who determined the relationship between rotational speed, feed rate, forces, torque, and diameter. In order to compare the results, they used two drilling methods to perform the test: on a CNC milling machine and manual drill. Each sample was attached to ATI mini40 sensor, which allowed to measure torque and forces as a function of time. The test was carried out with the maximum axis of 12,000 rpm and the test was carried out perpendicular to the long axis of the specimen. In contrast, the manual drill test used the power-tool cordless manual drill. In both cases, the

same drill bit with a diameter of 4 mm was used to compare the results more reliable. In addition, two plates were mounted to the sensor, to hold samples and to mount the sensor on a machine drill machine [49].

Bovine bone tests were also conducted by J. Lee et al., who presented the drilling process as a mechanistic model. The model made it possible to predict drilling forces in the material as a function of drilling conditions and drill geometry. Calibration experiments were also necessary due to the variability of materials parameters, which depend on the cutting and drilling conditions. For the tests, a drilling dynamometer was used to measure torque and thrust forces as a function of time, while holes were drilled using a CNC machine perpendicular to the long axis of the sample (Figure 3.21). The data was recorded at a data acquisition card and then filtered with a low-pass filter [46].

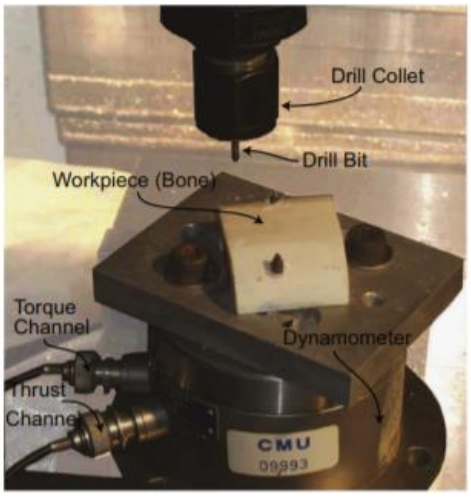

Fig. 3.21. The experimental setup used during the bone drilling experiments [46]

Although the drill-bits in the standard otologic drill are made of stainless steel, the authors decided to change them to carbide to reduce the wear rate of the drill. However, the entire geometry of the surgical drill was preserved, and an optical profilometer was used to measure the geometry of the drilling point. A pilot hole was drilled four times greater than the drilling point height to distinguish between cutting-lip forces and chisel-edge forces (Figure 3.22). As a result, the drilling area is divided into three zones. In a zone I the forces slowly increase as the drill point enters into the bone. Then the forces arise only from the cutting lips when the drill point is completely inside the bone (zone II). In zone III, after the depth exceeds that of

the pilot hole, the forces from both the cutting lips and the chisel edge are measured. This allowed noting that the entry forces in zone I were lower than after crossing zone III [46].

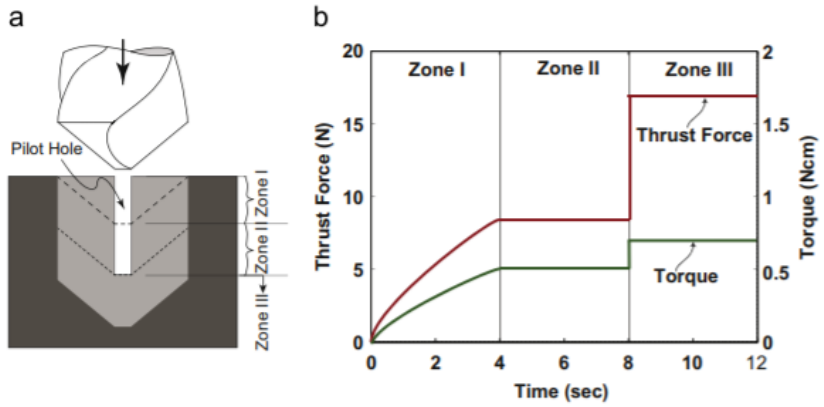

Fig.. 3.22. Drilling in the presence of a pilot hole: (a) three separate cutting zones and (b) the associated thrust force and torque [46]

Drilling research on composites used in 3D printing, whose task is to imitate human bones, were prepared by Bruce L. Tai et al. They used a steel drill bit that was driven by a clinical hand drill and the entire drilling system was set on the servo-controlled motion stage (Figure 3.23). The full speed of the hand drill was 1000 rpm and the feed rate was determined based on early tests. The samples were drilled to a depth of 5 mm. Next, an additional experiment was carried out and to avoid the material being softened by the induced heat during drilling, the rotational speed was reduced from 1000 to 330 rpm. It was necessary to scale the drill bit to a diameter of 9.5 mm, because it was impossible to print smaller unit cells for the tested 3DPIC material, due to the inadequate resolution of the 3D printer [50].

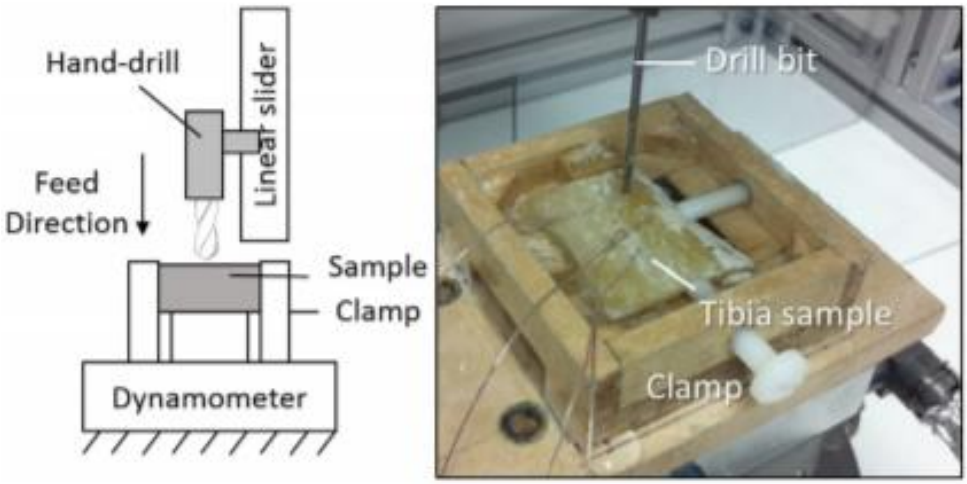

Fig.. 3.23. Experimental setup for bone drilling tests [50]

The same authors investigated the drilling thermal response using three surgical drilling tools: K-wire, twist drill and abrasive bur (Figure 3.24). K-wire is a wire with a trocar tip without cutting flutes and is used to drill deep holes or to fix bone fractures. Their advantage is effective bone cutting while removing chips. During the experiment, a twist drill with a diameter of 2.5 mm and a 2 mm K-wire was attached to the Stryker hand drill. The test was made on a bovine bone sample of 3DPIC material, in which holes with a diameter of 0.7 mm and 3 mm below the surface were drilled and two thermocouples were embedded in them. In order to maintain precision during drilling, a pilot hole was made in the samples, and one and a half millimeters from the drilled hole margin there were two holes [50].

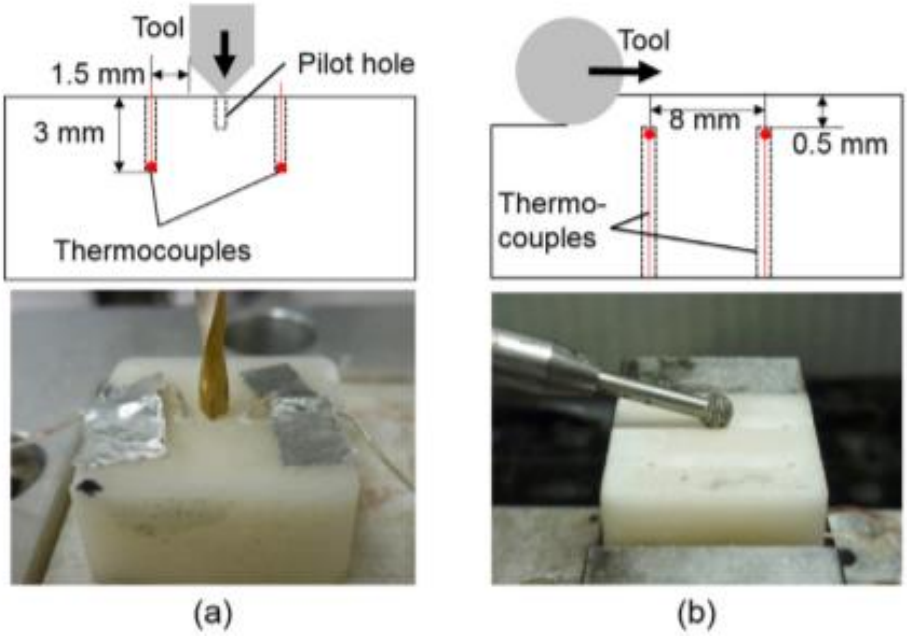

Fig. 3.24. Experimental setups for machining temperature tests: (a) drilling set up for the twist drill and K-wire, and (b) grinding setup for the abrasive burr [50]

For abrasive burr, a different configuration was used (Figure 3.25), in which a high-speed drill was used at a speed of 60000 rpm. A high-resolution translational system was built, consisting of three linear stages, on which the drill was mounted, and cutting was carried out at a depth of 0.5 mm. In order to investigate the temperature between the material interface and burr, in this case, two thermocouples under the surface were also used [50].

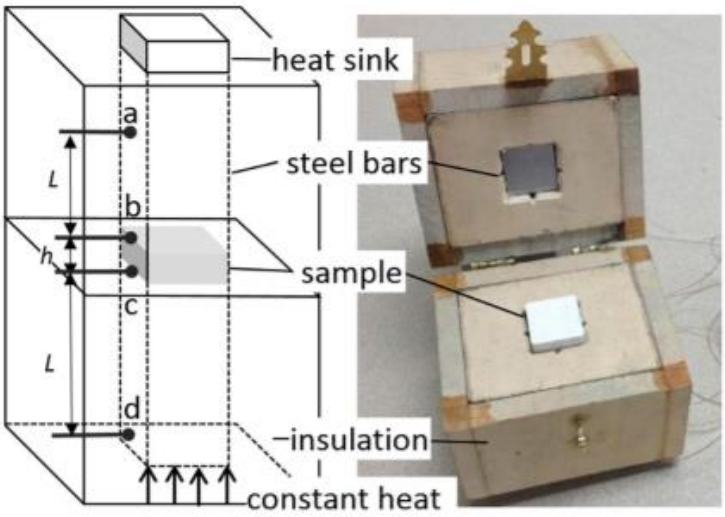

Fig. 3.25. The apparatus used for thermal conductivity measurement [50]

3.5. Validation of the mechanical response of the model

The model produced by additive manufacturing techniques should behave like a real human bone, therefore its mechanical properties should be similar to bone properties. To check this, it is necessary to perform mechanical tests on the models. The most often strives to achieve such properties as elastic modulus, flexural strength, ultimate strength, yield strength, tensile strength or compressive strength and depending on this, appropriate tests are performed. Most models for pre-operative help, also temporal bone models, are usually made of polymeric materials due to their lightweight and low production cost. The most popular tests performed on polymer samples are bending, tensile, and compression tests. The tests are performed in quasi-static or dynamic conditions. Quasi-static mechanical tests, in contrast to high-load tests, have been extensively studied by many scientists in the case of spongy, cortical and composite skull structures. The tests are performed in quasi-static or dynamic conditions because their joint statement allows obtaining conclusions on the use of commercially available bone substitutes [1, 3].

One of the methods of obtaining a module of elasticity and plasticity is the three-point bending test (Figure 3.26). It consists of determining 3 contact points between the camera and the sample and applying force to the centerline. Such a measurement method was used by J.B. Hochman at al. who examined the self-made temporal bone made of powder material using different types of infiltrators at a later stage. During the test, the sample was bent with increasing force, until the machine reached the maximum load or until the sample was broken.

On this basis, data on forces, distance and time were obtained, which allowed calculating stresses and strains [1].

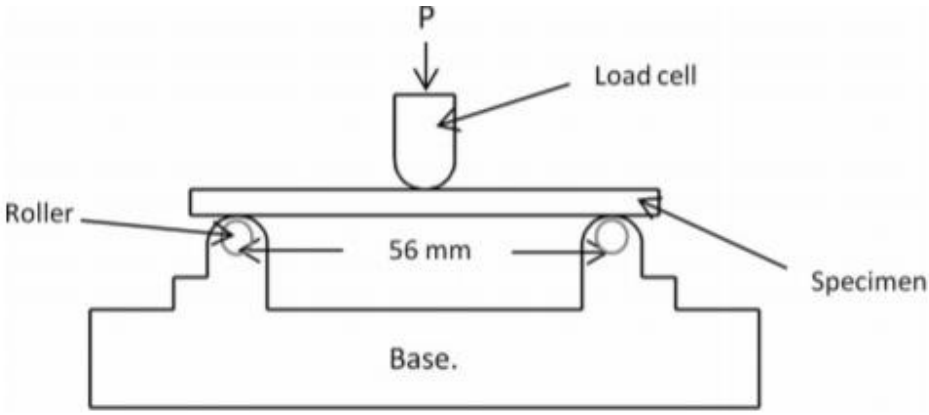

Fig. 3.26. Three-point bending fixture [51]

Another, similar test method is the four-point bending testing, in which, assuming the uniformity of the sample, the modulus and strength are equivalent to tensile strength and elastic modulus (Figure 3.27). This type of test was made by B. L. Tai et al., who tested the 3DPIC composite material containing epoxy and patch powders. The test was performed on six different samples, five of them with 3DPIC and one pure epoxide sample. The machine was equipped with a servo controlled with a maximum load of 1000 N, which controlled the loading rate of 5 mm/min. Besides, the equipment had a force transducer to measure the load force. As in the previous case, the force-deflection data allowed to calculate the strength and the module of the tested materials [50].

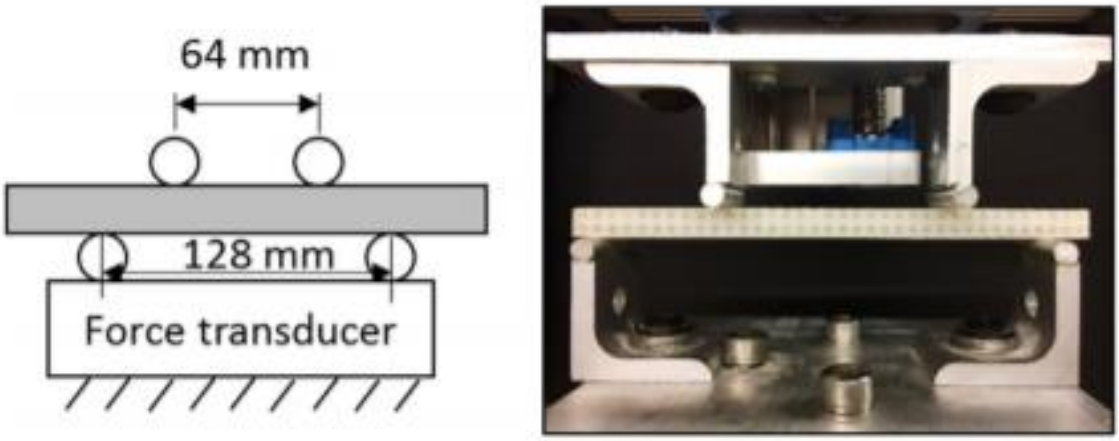

Fig. 3.27. Experimental setup for the four-point bending [50]

The quasi-static test can also be used for a servo-controlled hydraulic load frame, and an example of such a mechanism is the MTS 810. Tensile and compression tests were carried out on a hydraulically driven materials test system by W. Chen et al. who studied the behavior of two polymers PMMA and Epon 828/T-403 epoxy. An axial strain was measured using the MTS extensometer, while the load was measured by an Interface load cell [52].

A. D. Brown et al. performed a compression test on a 50 kN Shimadzu universal testing machine of commercially available bone simulants in quasi-static conditions. The samples were cylinder-shaped for transvee loading conditions and the shape of rectangular prisms for longitudinal loading conditions. In this case was necessary to set the initial crosshead speeds, which corresponded to the sampling rate 5 and 100 s^{-1} the nominal rate rates 10^{-1} and 10^{3} s^{-1}. Sometimes it is necessary to use a lubricant between the platen-specimen interfaces to minimize friction and an example of such a lubricant is Molybdenum disilicide [3].

It can be seen from the literature that one of the most commonly used dynamic testing machines is the aluminum Split-Hopkinson Pressure Bar (SHPB) system (Figure 3.28). It consists of a gas gun, incident bar, impact bar or striker, transmission bar and specimen. The principle of operation is based on the emergence of a compressive elastic wave at the impact of the incident bar, whereby the duration of the pulse is proportional to twice the length of the striker bar. The part of the wave proportional to the strength of the deforming sample is sent to the transmission bar, and the reflected wave fraction returns as tensile stress wave back to the input bar. On the transmission and incident bar, there are attached strain gauges, which record signals generated by wave propagation. As a result, strain rate, strain and stress, and their relationships are obtained. In order for the data made on SHPB to be reliable, a constant deformation rate is required after the sample has reached the stress balance. Typically, it is considered to be a time that includes four wave reflections in the sample. One of the methods to obtain an almost constant strain rate is to apply on the striker-incident bar a pulse profile that minimizes wave propagation. For example, A.D. Brown et al. who examined the synthetic bones on the described machine, used as the material shaping the pulse the value of A4 paper and cardboard fixed to the striker-incident bars interfaces. Additionally, to minimize friction, they used the previously mentioned $MoSi_2$. For the dynamic study, the authors used strain rates with values of 900, 1000 1400, 1500 and 1550 s^{-1} depending on the samples [3].

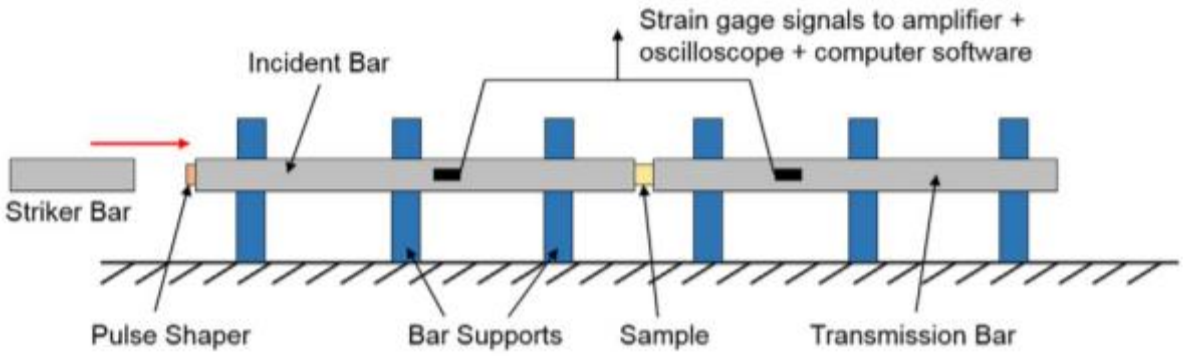

Fig.. 3.28. Schematic of a conventional Split-Hopkinson Pressure Bar system [3]

An interesting way of measuring the properties for high strain rate testing of polymers was used by the previously mentioned authors from The University of Arizona, W. Chen et al. To perform dynamic tension experiment, they modified the Hopkinson tension bar split. In the conventional split version, the Hopkinson tension bar consisting of the striker, transmission and incident bar sample is located between the bars. In this case, the researchers used a system in their system, where the tube, or striker, slides on the outer surface of the incident bar. Another modification they made was the performance of the transmission bar from high-strength aluminum alloy instead of steel, which allowed to improve the magnitude of the weak transmission signal. However, due to the sufficient strength and rigidity of the material from which the samples for the compression test were made, they used solid aluminum SHPB [52].

3.6. Additive manufacturing

3.6.1. Basic definitions

Additive Manufacturing (AM) is defined as the process of joining materials to make parts from a 3-dimensional model data one layer at a time. This process builds part usually layer by layer using powders or liquids, and in the case of polymers filaments are also used. Other terms used as a synonym for AM are: 3D printing, rapid prototyping, direct digital manufacturing, freeform fabrication, additive fabrication, additive layer manufacturing. Figure 3.29 shows the general manufacturing process using the additive method [47, 48].

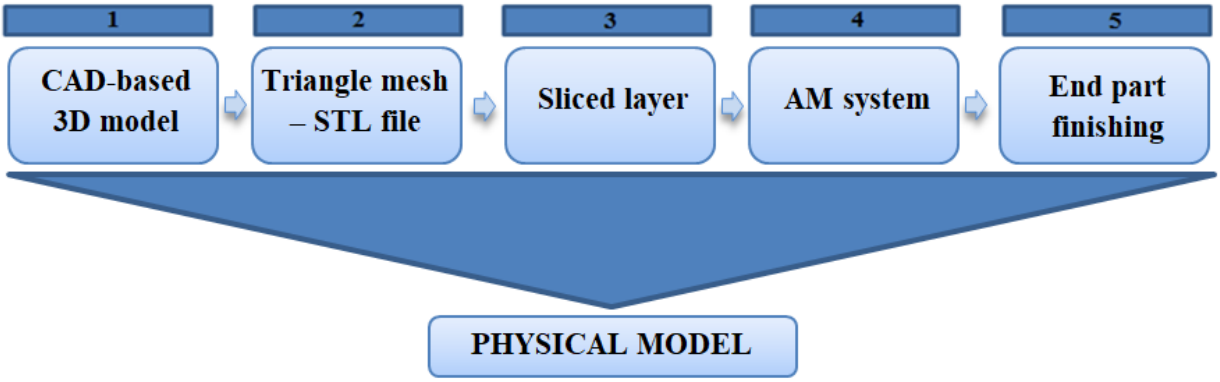

Fig. 3.29. Scheme of the process of creating a physical model [48]

3.6.2. Processes

The first Rapid Prototyping techniques appeared in the early 1980s century. There are many different methods used in Rapid Prototyping depending on the material used, its distribution, process category, state of fusion and basic manufacturing principles [54, 55].

The most commonly used techniques are [55]:

- SLA - Stereolithography (Stereolithography) (Figure 3.30b),
- SLS - Selective Laser Sintering
- LOM - Manufacture by applying material layers (Laminated Object Manufacturing),
- FDM - Fused Deposition Manufacturing (Figure 3.30a),
- 3DP - 3D printing (Three Dimensional printing).

Fused Deposition Modeling (FDM) was patented in 1989 and printers based on this technology are currently the most popular 3D printers at the consumer level for printing polymer composites, based on additive manufacturing systems. The extruded semi-liquid polymer, 3D printed on the work platform, solidifies instantly and translates sliced layers of digital data into an actual manufactured object [54].

Stereolithography (SLA) was one of the first AM techniques developed. The concept of this technique is printing with photocurable resin, usually acrylic or epoxy. This resin is exposed to ultraviolet (UV) light of a certain wavelength, as a result of which exposed 2D resin layers solidify in the photopolymerization process. During the process, the platform is immersed in the reservoir of liquid polymer to a depth of about 0.05-0.15 mm before printing and this defines the actual layer height or the depth of each slice of the entire 3D object in a .STL file. Then the UV laser reflects from the surface of the liquid polymer through the mirror and travels the whole path of the cross-sectional pattern. In the next stage, the platform

is moved down at a predefined depth, the printing cycle is repeated and part is built layer by layer at the moment the entire object is formed [54].

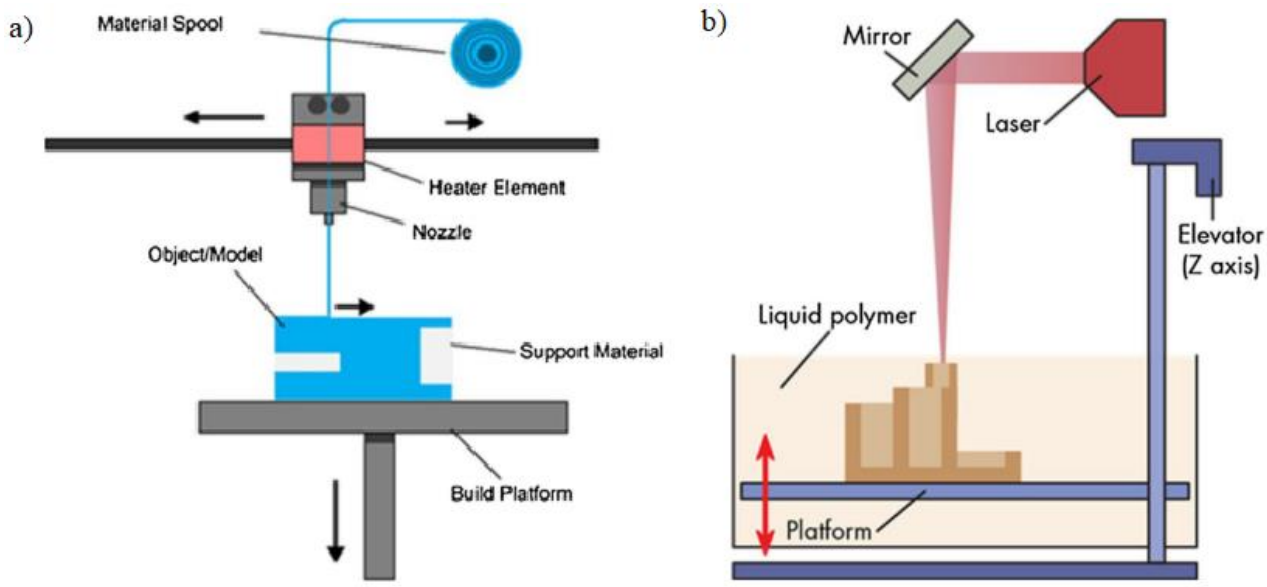

Fig. 3.30. Rapid Prototyping methods: a) FDM setup, b) SLA setup [54]

PolyJet is an advanced inkjet technology that uses photopolymers or other liquid materials instead of the ink (Figure 3.31). In this method, many print nozzles spray small droplets of the material that are subsequently cured with the UV light to form layers on the build platform. Several printheads can be used at the same time, therefore it is possible to mix colors and different building materials with different properties. Support must be used for complex printouts, and due to printing with several printheads, the wax or gel-like supporting material can be co-deposited and then removed by heating or washing with water. The materials used for Inkjet AM must be temperature-stable and have the appropriate viscosity at the temperature in the head [54, 56, 57].

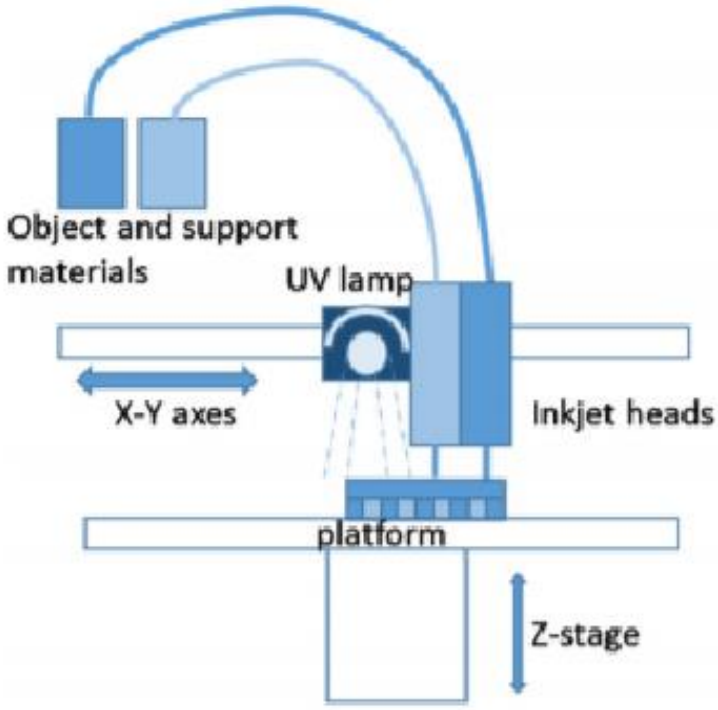

Fig. 3.31. PolyJet setup [58]

The advantage of PolyJet (JP) technology is definitely the printing of ultra-thin models with complex geometry in which the dimensions of the layer can be less than 20 μm. PolyJet technology surpasses FDM technology primarily due to the resolution. In the PolyJet technology it is possible to print ultra-thin layers with a thickness between 16 and 32 micrometers, while in the FDM technology between 0.06 and 0.5 mm [59].

Figure 3.32 shows a comparison of elements made with both additive manufacturing methods [60].

Fig. 3.32. Stratasys material comparison: Black: FDM Nylon6, White: Polyjet Rigur (PP like) [60]

In addition, this technology shows the ability to manipulate various materials and use them while printing one model. This allows for obtaining optimal and functional projects. Other advantages include the insignificant stair stepping effect. With this technique, parts with properties similar to those made of ABS thermoplastics can be obtained. However, under high load conditions, the process has a slow recovery rate, which is its disadvantage. This was proven by Yep et al., who examined the recovery rate of honeycomb-printed using PolyjetTM technology. He showed that after an hour of unloading only 80% of the shape was recovered. In the case of AM technology, the material strength is still lower than the biological bone. The disadvantage of PolyJet technology is, above all, a very high price, which strongly limits the availability of JP relative to the much cheaper FDM technique. In FDM technology, physical models are more demanding in post-processing, such as model cleaning and removal of supports (Figure 3.33) [57, 58, 59, 61].

	PolyJet 3D Printing	Fused Deposition Modeling (FDM)
Operations		
Process Time	●●●	●●◖
Pre-process	●●	●●●
Post-process	●●●	●●●
Office Environment	●●●	●●●
Ease of Use	●●●	●●●
Characteristics		
Surface Finish	●●●	●
Feature Detail	●●●	●
Accuracy	●●	●●●
Size	●●●	●●●

Figure 3.33. Comparison of PolyJet and FDM technologies [59]

3.6.3. Medical applications

In medicine, 3D printing has been used since the 2000s and since then its use has changed a bit. 3D printing is used to produce bones, various types of human organs, glasses, blood vessels, tissue, stem cells, and even drug delivery devices. At the moment, the application of AM technology in medicine can be divided into such categories as: creating prosthetics, implants, and anatomical models, tissue and organ fabrication, and pharmaceutical research concerning drug discovery, delivery, and dosage forms. In addition, one of the applications is the design and production of biomodels, surgical instruments, implants or scaffolds for tissue

engineering. In addition, the development of training models and medical devices is becoming more and more popular [62, 63].

Biomodels are physical models of anatomical structures produced on the basis of 3D digital data using the Rapid Prototyping methods (Figure 3.34). As a result, the doctor has the ability to create a direct replica of the organ or region of interest (ROI), which allows him to better understand the anatomy of the patient and plan the operation. The use of 3D models includes orthopedic, craniomaxillofacial and detective surgery [62, 64].

Fig. 3.34. Biomodel and customized implant for craniofacial reconstruction surgery [64]

RP methods also enable the production of individualized implants for patients in the case of complex defects (Figure 3.35). They are made to order, specially designed to fit perfectly in place of the transplant. Implants and prostheses can be made in almost any geometry based on X-rays, MRI or CT scans into digital .STL 3D print files. As a result, both standard and non-standard upper and lower limb prostheses and surgical implants are produced. It is used, among others, for the production of hip, spine or dental implants [63].

Fig. 3.35. Custom 3D-printed surgical and medical models generated from clinical data by researchers at the National Library of Medicine [63]

Organ and tissues can also be manufactured and it is especially useful in transplants because it solves any moral and ethical issues that may be tied to traditional transplant methods (Figure 3.36). In addition, this increases acceptance by the body, because customized organ development utilizes the patient's own cells and has contributed to research on diseases such as cancer [63, 65].

Fig. 3.36. Nose and ear 3D printed from live tissue [65]

Surgical aid tools are also important, which must also meet the appropriate requirements and be adaptable to the procedure, especially in the case of cosmetics surgery. The surgical instruments shorten the time of surgery, improve the surgeon's skills and ensure greater safety and increase accuracy. Biomedical modeling and 3D printing provide the opportunity to build models for surgical training that reproduce the patient's anatomic structure to the largest possible extent [62, 66].

Additive manufacturing techniques can also be used in pharmacology, thanks to the possibility of producing special elements to facilitate drug delivery to the human body (Figure 3.37). An example of such an application is the concept of "Polypill" tested in patients with diabetes. It is an application dealing with the dosage of drugs and solves the problems of the reaction of various drugs [65].

Fig. 3.37. Robot arm holds a 3D printed drug [65]

3.6.4. Additive manufacturing of medical models

The additive manufacturing process of medical models consists of several stages:

1. Retrieving data from medical imaging
2. Creating a 3D model using appropriate software
3. Saving the 3D model as a .STL file
4. Loading the file into the printer software
5. Physical model printout

One of the most popular methods for obtaining a model is to obtain data using high-resolution CT and/or MRI scans from cadaveric specimens for model generation (Figure 3.38). The process of creating such a model has been very well described by J. Cohen and S. A. Reyes or Austin S. Rose et al. After the scan of the model, it is necessary to convert the CT data into a 3D model using the appropriate software. The next step is segmentation using intensity thresholds to isolate bone, then post-processing of the model. The process includes grid formatting, smoothing, and manual segmentation. All artifacts must be removed or repaired to make the skeleton reproduce the anatomy as much as possible. This includes closing holes, creating bridges, smoothing or removing unnecessary elements. Finally, the model is converted to an STL file, that uses triangulation to describe the surface and geometry of a three-dimensional object that can be loaded into the printer program [67, 68, 69].

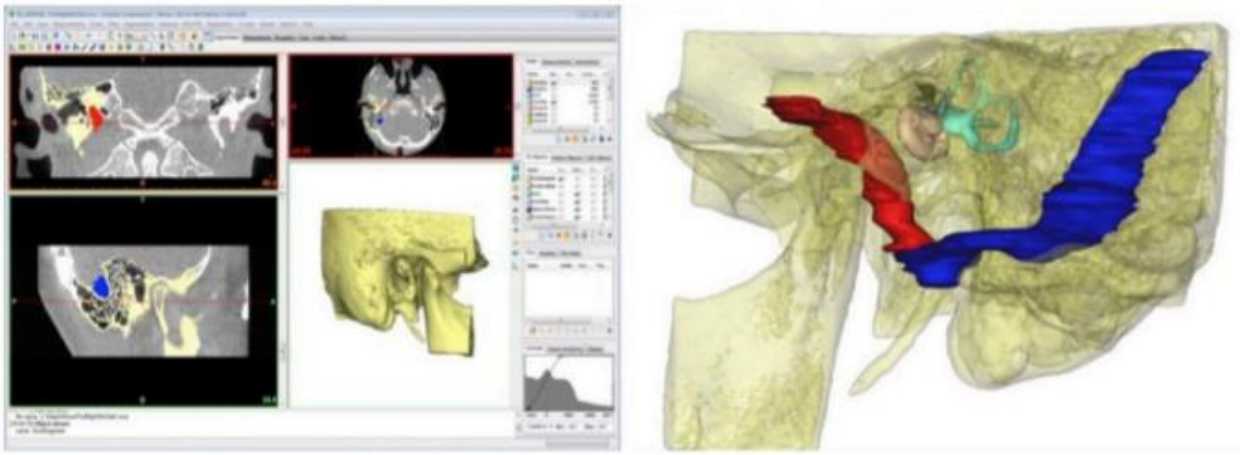

Fig. 3.38. DICOM data imported into 3D image-processing software, demonstrating bone and the segmentation of soft tissue structures [69]

Another method of obtaining a 3D model can be the mapping of bone structure and ear elements using CAD programs such as Autodesk 123D, which was made by S. R. Barber et al. They made 2D sketches that were converted into vectors using Adobe Illustrator and exported as scalable vector graphics (SVG) files. Then 2D SVG files were imported into Autodesk 123D and extruded as parametric 3D meshes and exported as Stereolithography and Polygon File Format files [70].

The STL file is then loaded into the printer software and the model is created using the chosen Rapid Prototyping technique and the appropriate material. There are many printers on the market for printing medical-related models. For example, M. J. DA. Cruz and H. W. Francis used the 3D printer Z510 from the German company 4D Concepts, and S. R. Barber Zcorp 650 inkjet printer, in which they used full color through Sculpteo. Different examples of printers are the Dimensions SST 1200es Printer and PolyJet (e.g. Objet350 Connex printer) [1, 67, 68, 70].

The material to be examined will be used in the future to print the temporal bone model, which includes both hard and soft tissues. Therefore, it is necessary to find a technology that allows the printing of two materials with different properties at the same time. In addition, the printer's resolution must be very high, because the structures of the inner ear such as the ossicles are very small. The stapes is the smallest bone in the body and has a length of about 3 mm [7].

Many manufacturers offer dual-head or more head printers that enable printing of at least two materials. The model should be manufactured from plastic, therefore in the review, the

technology using such materials was taken into account. One of the technologies that have dual-head printers are FDM. An example of such equipment is a printer from the Polish company ZMorph with a Dual Extruder head, which can simultaneously use two different filaments with similar thermal properties. This head can be used for selective printing of two materials (PLA or ABS), printing with water-soluble PVA and mixing of ABS and PLA materials. The DOUBLE P255 printer from 3DGence is another example of the Polish manufacturer. Prusa Research proposes a Multi Material Upgrade 2S printer in which it is possible to print complex and colorful objects from 5 different filaments simultaneously. The French brand Volumic has a dual stream version of the Stream 30 Dual MK2 printer that allows printing from 40 different types of materials. Other examples of dual-head printers are also Ultimaker S5 from Ultimaker or Pro2 from Raise3D [71-76].

One of the more advanced multi-material 3D printing technologies is MultiJet or PolyJet. MultiJet simultaneously prints and mixes rigid and flexible photopolymers. An example of such solutions are the ProJet MJP 5600, ProJet MJP 2500/2500 Plus printers offered by 3D Systems. A single part manufactured using the PolyJet technique can have different mechanical properties, colors, and opacities. The Connex family of printers uses several mixed resins at the same time to create digital materials. The Stratasys company offers such printers, and examples are the Objet260 Connex3 and the Objet500 Connex1 (Figure 4.2). In addition, the company has such models of multi-material printers as the Objet1000 Plus, which has the option to combine up to 14 different materials in one part [77, 78].

3.6.5. Materials for the bone models

Models intended for pre-operative planning must be characterized by high accuracy and good surface quality. They should as much as possible imitate the real anatomy of the organ and reproduce the feeling of the surgeon during operations. In addition, attention should be paid to the economic aspect, taking into account the time and costs of the prototype creation. The FDM technique allows the production of such materials like PLA, ABS, NYLON, PC, PMMA, PET-G and many more. In addition, support materials are used such as HIPS and PVA. Research of Max Haffner et al. consisted of printing and comparing five models of the temporal bone in each of the types of plastic, which included just ABS, PC, PLA, PETG and white nylon [50, 79].

Another interesting material is the 3D polymer-infiltrated composite material (3DPIC) developed by B. L. Tai et al. The material contains patch powders and an epoxy, which is 3D

printed using the binder jetting technology and then infiltrated with the epoxy to develop the desired strength. Another solution for the creation of the 3D printed temporal bone model was proposed by Jordan B. Hochman et al. who used a proprietary composite powder in his work. Polylactic acid (PLA) filament is obtained from the maize meal and does not contain heavy metals. Its unique feature is biodegradability, which ensures that it is safe [1, 50].

It would seem that Polyurethane (PU) foams are ideal bone-mimicking materials, but in reality, they are generally much weaker than real cortical bones. That is why the synthetic materials have been improved to ensure good stiffness and durability, which resulted in sawbones. They are made of a glass-fiber-reinforced epoxy and are easily machinable [50].

Similar material is Synbone, which is based on a foam material with a gradient of pores through the thickness. It simulates the outer table-cancellous-inner bone structure 6 mm thick plates and 780 kg/m³ density. A.D. Brown et al. have examined the mechanical response of Sawbone and Synbone for a quasi-static and dynamic loading. Studies have shown that the Sawbones had a nominal Young modulus (395-475 MPa) similar to the transversely loaded cranial bone with high porosity that underwent dominant diploë buckling failure mechanisms. The Synbone, on the other hand, has a nominal low strain Young's modulus equal to 1.5 GPa under a transverse load, closely matched he gave the value of the human skull [3].

Earlier mentioned by M.J. Da. Cruz, H.W. Francis used a casting powder and a bonding agent with bone-like properties. Then the material was improved by modifying the bonding agent and its concentration until the manufacturer found them to be good enough. Austin S. Rose et al. in his work to create a model of temporal bone used PolyJet technology and materials consisting of different proportions of multiple thermoset polymers. Thanks to this, various anatomical structures have unique biomechanical properties. This technology allows obtaining a multi-material bone model in which it was easy to distinguish between soft tissues and cortical bone structures [21, 68].

.

4. The methodology of the research

4.1. Research plan

Figure 4.1 shows a schematic of the tasks performed during the project implementation. The research included in the work was part of a project leading to the creation of a temporal bone simulator for training surgeons. Each of the project members got the appropriate scope of tasks. This thesis contains all the tasks presented below and the selection of appropriate parameters to perform the tests described in this work. Some decisions, such as the number of samples, the number of tests performed and some parameters selected during the compression and drilling test, have been imposed by supervising institution.

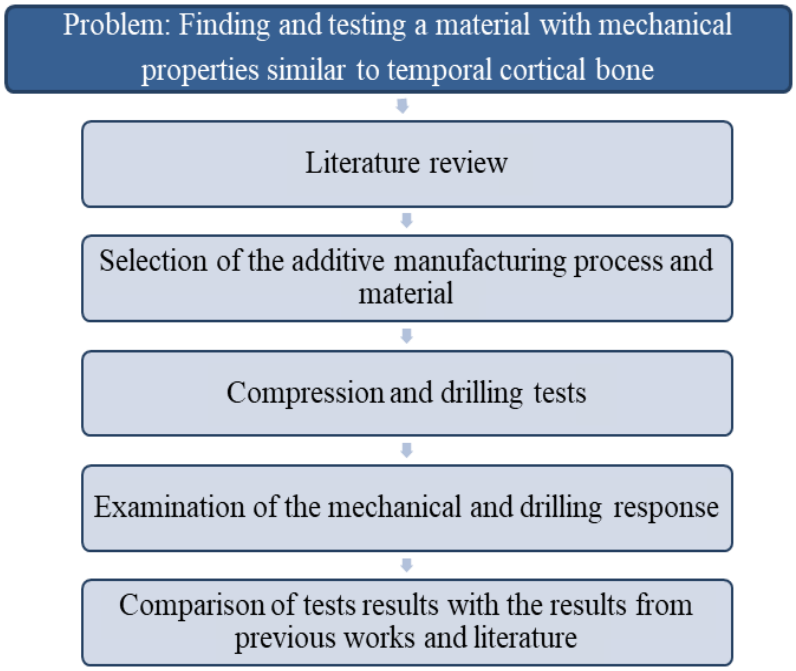

Fig. 4.1. A schematic representation of the research plan (own source)

The aim is to perform tests on samples made with Rapid Prototyping technology from a selected material that has mechanical properties as close as possible to real temporal cortical bone.

The whole research plan includes literature analysis and a practical part consisting in performing and analyzing results of appropriate tests. The literature analysis consisted of getting acquainted with the methods and materials used by researchers in previous works. The

first step was to find the mechanical properties of the cortical bone of the temporal bone. Analysis of previous tests and results allowed obtaining the value of the mechanical properties of human bones, which are necessary to compare with the results of tests obtained in this work. On this basis, it was possible to select the optimal measurement method and parameters to perform the test. The next step was to find the manufacturing method that meets all the necessary model requirements. After finding the technology, it was necessary to find a material that can be used in the selected method of additive manufacturing and properties similar to the cortical bone.

To test the mechanical properties of the material, compression tests were carried out under quasi-static conditions. Next, drilling tests on the selected material have been carried out in order to find the forces and torque, whose values were previously tested by other project members in real bone drilling tests. These parameters allowed comparing the behaviour of the material with the behaviour of the bone during drilling.

All test results made on the tested material were compared with the results from previous works and data found in the literature in relation to the bone.

In addition, a questionnaire was created for later research in cooperation with surgeons. The questionnaire includes questions to validate the quality and usefulness of the test material, from the viewpoint of the surgeon.

4.2. Manufacturing

4.2.1. Chosen production method

Based on a detailed analysis of additive manufacturing methods, the appropriate technology was selected to meet the model requirements. The temporal bone model must be manufactured out of two materials with different mechanical properties. One of them should imitate hard tissue and the other one - the soft tissue. In addition, the simulator for surgeon training must have good surface quality for even the smallest elements, such as auditory ossicles.

The initial multi-material requirement limited the choice of technology to FDM or PolyJet. Both technologies have the ability to depose two materials at the same time (in a single layer), therefore the main factor in the choice of method was resolution and post-processing. In that comparison, the PolyJet is better, so it was selected as a preferred technology. After a wide research, it was decided to cooperate with the Cadindus company, based in Mulhouse, France, which had both a PolyJet 3D printer and suitable materials in its

offer. The samples were manufactured on a Connex 3 printer (Figure 4.2). The design capacity of the printer (X, Y, Z) is 490 x 390 x 200 mm and it has a choice of 14 materials, including 46 colors [80].

Fig. 4.2. Connex 3 printer [80]

4.2.2. Material selection

When selecting the material, the main goal was to ensure that its mechanical properties were similar to those of real skull bones, found in the literature [1, 3, 21, 50, 68, 79].

The range of materials has also been limited to the PolyJet technology because it allows the precise reproduction of the smallest bone structure of the ear. In addition, this technology allows you to print a model containing material that imitates hard tissue and soft tissue at the same time. Materials designed for the chosen technology proposed by the Stratasys company were analyzed. The most important properties that appear in the data sheet of PolyJet materials are tensile strength, elongation at break, modulus of elasticity, flexural strength, hardness, and density. The focus was on materials with the highest modulus of elasticity and high tensile strength [59].

Attention has also been paid to the temperature properties because when drilling the temporal bone, the drill-bit generates heat and the material must withstand the right temperature so that it does not melt. For this reason, the High Temperature Material

(RGD525) was initially considered which has the highest modulus of elasticity of all the materials presented in the datasheet and is equal to 3200-3500 MPa, which most closely approximates the modulus of elasticity of the human bone (Table 4.1). It also has very good temperature properties. However, after consulting with the company that produces the samples, it turned out that the heat treatments that are necessary after printing to reach higher mechanical properties cannot be used in for materials that can imitate the soft tissue. This prevents its use because in the future the bone model will be manufactured from two materials with different properties at the same time [59].

Another material used in the PolyJet technology, which was taken into account was the RGD720 material, whose Young's modulus is in the 2000-3000 MPa range. In addition, its other mechanical properties have quite high values, for example, tensile strength is between 50-65 MPa [59].

The last considered material was VeroWhite, which has properties similar to RGD720, but the greater value for flexural strength. In the project, bending tests will not be performed, therefore this parameter was not significant. Considering the value of Young's modulus, it would be best to choose High Temperature Heat-Resistant material. However, as mentioned above, it could not be used due to heat treatment temperature. Materials VeroWhite, RGD720 and VeroPureWhite have the same value of tensile strength and Young's modulus. Materials RGD720 and VeroPureWhite have a higher value of flexural strength than the VeroWhite. After consulting with the Cadindus company and the research funding institution, due to the limited availability of materials, it was decided to choose the VeroPureWhite [59].

Table 4.1. Comparison of mechanical properties of selected materials [59]

	VeroWhite Polyjet Material	High Temperature Heat-Resistant PolyJet Material	RGD720 PolyJet Material	VeroPureWhite PolyJet Material
Tensile Strength [MPa]	50-65	70-80	50-65	50-65
Elastic Modulus [GPa]	2-3	3.2 - 3.5	2-3	2-3
Flexural strength [MPa]	60-70	110-130	80-110	75-110
Shore Hardness D	83-86	87-88	83-86	83-86
Density [g/cm^3]	1.18-1.19	1.17-1.18	1.18-1.19	1.17-1.18

4.3. Mechanical properties testing methodology

Two types of compression tests were performed: with and without unloading.

The dimensions of the samples for compression test without unloading were determined based on ASTM D695 - Standard Test Method for Compressive Properties of Rigid Plastics. The standard assumes a cylindrical or prism shape of samples whose length is twice its principal width or diameter. The preferred dimensions of the samples are 12.7 mm in diameter by 25.4 mm for the cylinder and 12.7 to 12.7 to 25.4 mm for the prism. During the 3D printing of cylindrical shapes mentioned in the standard with additive manufacturing techniques, it would be necessary to create support which during the removal could change the size of the sample. For this reason, the parallelepiped shape of the specimens was chosen with the preferred dimensions preserved. To perform the experiment, 30 samples of material VeroPureWhite were manufactured (Figure 4.3) [80].

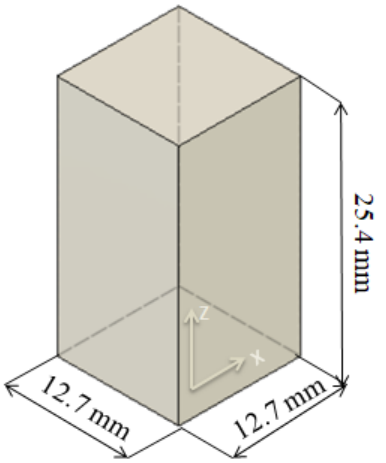

Fig. 4.3. The sample with dimensions and a reference framework (own source)

Both cortical and cancellous bones have anisotropic mechanical properties and this should be taken into account during experimental studies on samples taken directly from the bones, as well as on materials that should imitate them. The main directions of the anisotropy of these materials are related to the loads they are subjected to under physiological conditions. Samples for testing were manufactured in various orientations, to examine the effect of the print direction on the mechanical properties of the material (Figure 4.4). A framework was applied to each of the manufactured samples. During the compression testing, all the samples

are placed vertically, taking the longest edge as the height. As a result, the samples were loaded in the X, Y and Z directions.

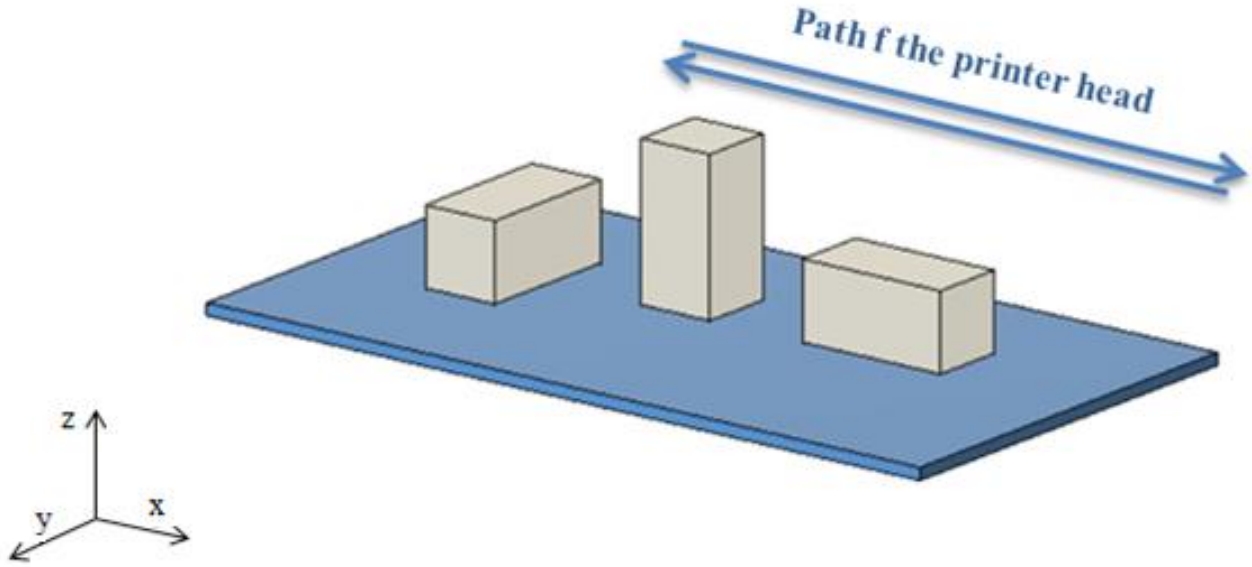

Fig. 4.4. Different printing orientations tested (own source)

The samples were marked with a marker from 1 to 10 for each direction X1-X10, Y1-Y10, and Z1-Z10 respectively. The samples were then measured using an electronic caliper and weighed. On this basis, the volume and density were calculated, which is the ratio of the mass and volume of the sample. Compression tests were carried out using an Instron 5585 H machine equipped with a video extensometer to measure the strain of the sample and controlled by Bluehill software (Figure 4.5). The capacity of the cell was 100 kN. The tests were performed for a strain rate equal to 0.01, 0.001 and 0.1 s^{-1} and an initial load of 30 N was applied. It should be noted that the values of strain rate obtained during machining are very high but that it was necessary to first determine the behavior of the material in quasi-static conditions and small strain rates. Two points were drawn on the machine plates between which the sample was placed in order to track their motion during the test and calculate the strain of the sample. Maximal value of strain of 0.4 was chosen according to the literature [59].

Fig. 4.5. Experimental equipment - an Instron 5585 H (own source)

The maximum value of displacement was calculated based on the formula:

$$\varepsilon_{nom} = \frac{\Delta l}{l_0}, \left[\frac{mm}{mm}\right] \tag{4.1}$$

where: ε_{nom} - nominal strain, Δl- displacement, l_0 - initial length of the sample. On this basis, an initial deformation value of 10.16 mm was imposed linearly on the specimen.

The Young's modulus was calculated by determining the linear regression for the linear section of the curve. The relationship between true and nominal strains and stresses can be maintained thanks to the fact that with large plastic deformations the volume remains

unchanged. To present the data, true stress and true strain were used which were calculated from the formulas respectively:

$$\sigma_{true} = \frac{Fl}{S_0 l_0} = \sigma_{nom}(1 + \varepsilon_{nom}), [MPa] \tag{4.2}$$

$$\varepsilon_{true} = \ln(1 + \varepsilon_{nom}), \left[\frac{mm}{mm}\right] \tag{4.3}$$

where: F-force, S_0 - an initial cross-section of the sample, l_0 - initial length of the sample, l - length after test, σ_{nom} - nominal stress, ε_{nom} - nominal strain, σ_{true} - true stress, ε_{true} - true strain.

The results of the mechanical properties of the tested material will be compared with the mechanical properties of the temporal cortical bone from the literature. Table 4.2 presents the averaged values of individual mechanical properties determined on the basis of the previous tests described in sub-chapter 3.3.3. The results from the last row of the table will be used to compare with the mechanical response of the VeroPureWhite material.

Compression tests with unloading were made on 10x10x10 mm cubic samples manufactured with PolyJet technology from VeroPureWhite. Four samples were used for the test. As before, the samples were measured and weighed to determine the density. The tests were performed at a strain rate 0.001 s^{-1}. Unloading was performed three times, the first time at the strain before peak strength, the second time in the plateau phase and the last at the end of the test. The test was performed on the same machine as the previous Instron 5585 H and was run-up to a maximum force of 6000 N.

Table 4.2. Summary of mechanical properties for temporal bone [35-44]

	Elastic Modulus [GPa]	Tensile strength [MPa]	Compressive strength [MPa]	Flexural strength [MPa]	Density [g/cm^3]	Hardness [μHV]	Loading type	Sample information
[38, 42]	11,73 ± 0,95	-	-	82,00 ± 25,50	-	-	Flexure	Parietal, temporal, frontal, parietal bones; composite samples
[37]	11,316	-	-	-	-	-	-	Frontal, parietal, temporal occipital bones; “sandwich” structure samples
[39]	9,87 ± 1,22	-	-	-	-	-	-	Frontal, parietal bone
[36]	5,61	-	-	-		-	-	Temporal bone; composite samples
[43]	-	67,73 ± 17,80	-	-	-	-	-	Temporal, frontal, parietal, occipital bones
[41]	-	70,53	152,24	-	-	-	Tension Compression	Parietal bone, cortical bone
[35]	E1 E2 E3 13,40 14,00 23,40	-	-	-	1,868	32,9	Ultrasonic test	Temporal bone; the cortical bone
[40]	-	79,29	-	-	-	-	Tension	Parietal, frontal, occipital bones; the cortical bone
Values of published studies used for comparison	**10,39 (mean)**	**72,52 (mean)**	**152,24**	**82,00 ± 25,50**	**1,868**	**32,9**	-	-

4.4. Machining tests methodology

Samples from VeroPureWhite material manufactured using PolyJet technology for drilling test had dimensions of 40x20x20 mm³ (Figure 4.6). Three samples were prepared in the same orientation. Two samples were used for the test, which was numbered “1” and “2”.

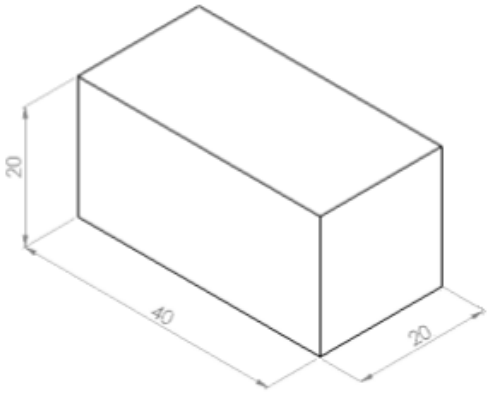

Fig. 4.6. The sample with dimensions for drilling test (own source)

Different values of the parameters were used. For the cutting speed (v_c) parameter, the values 10, 20, 32 m/min were taken. The feed rate (*f*) tested for each feed rate was equal to 40 μm/rot. The drilling depth in all tests was 5 mm. These test parameters have been chosen to facilitate the comparison between the obtained results and machining response measurements of bone from the literature and on-going experimental studies on bone samples. These parameters were established on the basis of a PhD thesis, in which similar tests were carried out on other materials [76].

Drilling tests were carried out on a machine designed by Martin Boillat, a student from Ecole Nationale d'Ingénieurs de Metz, who was a participant in the project on the development of a physical temporal bone simulator. The machine is designed to perform milling and drilling processes on samples taken from cadavers and samples from materials that are a substitute for bones (Figure 4.7). The machine frame was made of the MakerBot Replicator 2X 3D printer. The machine is equipped with a compact spindle with a tool rotation speed of 100 to 30.000 rpm and an air-cooled spindle kit. This drilling test has been followed by a drill-bit with diameter 3.1 mm. Strengths are measured with a Kistler Type 9345B 2-components sensor coupled with a Kistler Type 5017B charge amplifier. The Y and X axes are equal to the machine base, while the Z axis is oriented upwards. The appropriate stiffening and anti-vibration parts have also been designed to get the most accurate results.

To test the effect of the printing orientation during drilling on the mechanical response of the material, the test was carried out 4 times for each parameter set. The first 2 tests were done with the Z+ axis of the sample collinear to the test bench's Z+ axis, and the last 2 with the Z+ axis of the sample pointing the opposite direction (towards Z- of the test bench).

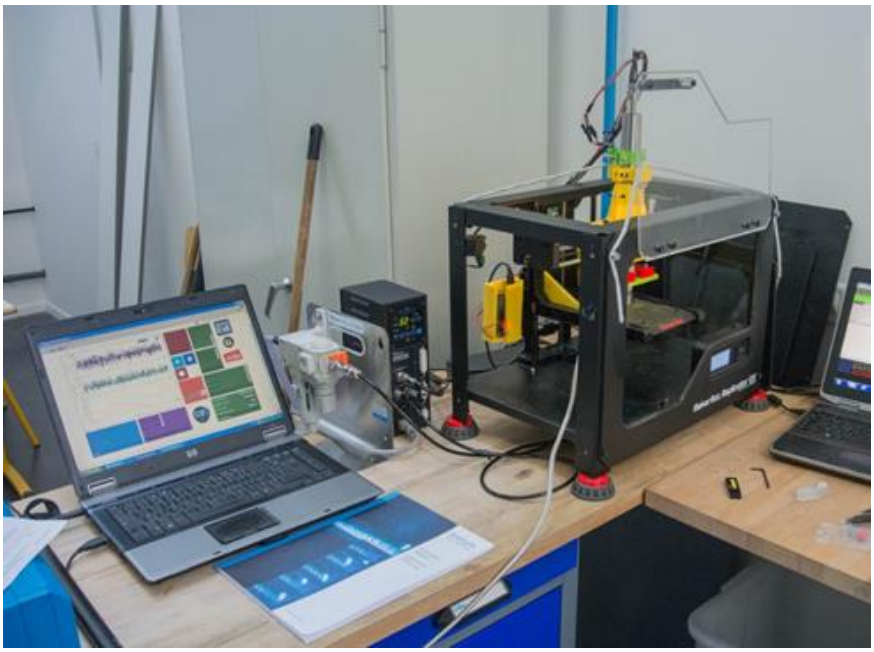

Fig. 4.7. Experimental setup for drilling and milling tests (own source)

4.5. Model assessment methodology

Material assessment by surgeons is very important because they will work with the temporal bone model. A questionnaire was created to evaluate the examined material for the temporal bone model and it can be found in Annex C. It is based on a five-point Likert scale and consists of two parts. The scale includes a grade based on five levels where: 1 – unlike, 2 – very different, 3 – similar, 4 - very similar and 5 – identical. The questions were created in comparison to the cadaveric temporal bone and real temporal bone. The first part covers issues related to haptic feedback, such as sensations during drilling, tissue sensation, and the effect of irrigation, vibration, and acoustic properties. The second part is focused on the general characteristics and the questions in it are related to the safety of the material, generation of the dust and the general purpose of the material [66].

The questionnaire was not filled by any surgeon in the scope of this work – it was not planned as part of these studies. This will be realized in the future.

5. Research results

5.1. Mechanical test results

5.1.1. Manufactured samples

Table 5.1 shows the measured dimensions and weight for each of the samples, as well as the parameters calculated based on them, such as volume and density. The weight of all the samples was virtually identical and varied by a maximum of 0.01 grams. The average density of the material was 1.17 g/cm³, which corresponds to the density given in the datasheet from the manufacturer. The exact results for each sample are provided in the table in Annex A.

Table 5.1. Measured and calculated parameters for samples (own source)

N° Sample	Dimension [mm]			Weight [g]	Volume [mm³]	Density [g/cm³]
	length	width	high			
X	12.65 ± 0.03	12.71 ± 0.02	25.36 ± 0.02	4.76 ± 0.01	4078.37 ± 13.57	1.17 ± 0.01
Y	12.65 ± 0.03	12.66 ± 0.03	25.36 ± 0.07	4.77 ± 0.01	4063.38 ± 14.19	1.17 ± 0.01
Z	12.66 ± 0.02	12.67 ± 0.04	25.38 ± 0.06	4.77 ± 0.01	4071.44 ± 19.58	1.17 ± 0.01
Mean	12.65 ± 0.02	12.68 ± 0.04	25.37 ± 0.06	4.77 ± 0.62	4071.06 ± 0.01	1.17 ± 0.01

5.1.2. The behavior of tested samples

Based on the results for sample number X6, the appearance, and character of the stress-strain curve was described. The presented shape of the curve is the typical answer obtained for all samples (Figure 5.1).

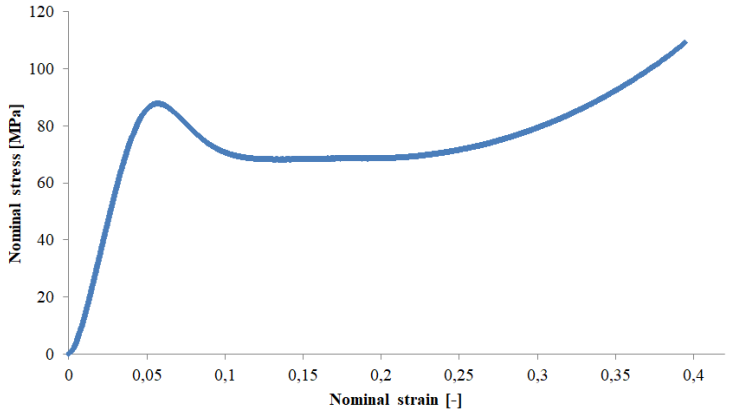

Fig. 5.1. The stress-strain curve for one of the tested samples (own source)

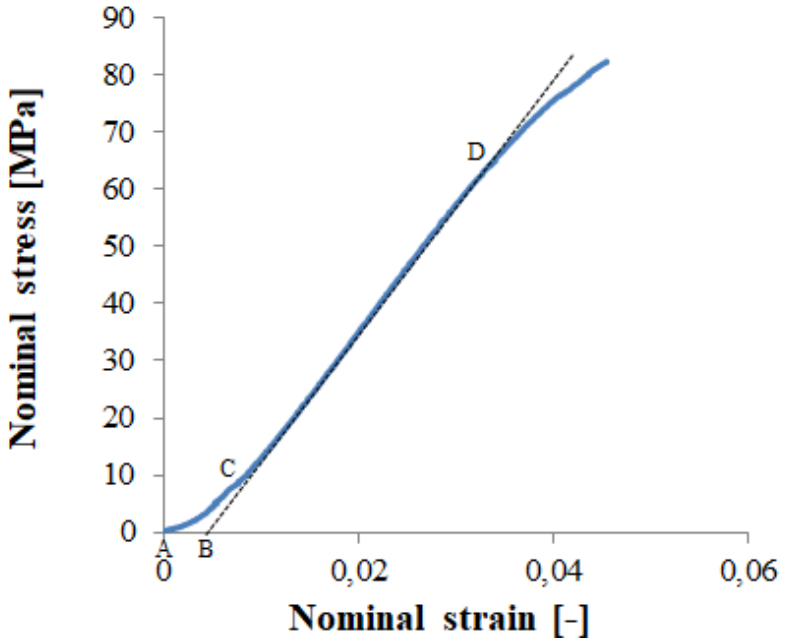

Fig. 5.2. The stress-strain curve with Hookean Region for one of the tested sample (own source)

At the beginning of the nominal or engineering stress-strain curve, there is a region, *AC*, which does not represent the properties of the material (Figure 5.2). This region is an artifact caused by taking a slack and seating or alignment of the specimen. Then, a linear part, *CD*, can be noticed, which can correspond to elastic behaviour. Along the line *CD* at any point by the strain at the same point, the elastic modulus of the material can be determined. The slope of the curve then tends to gradually decrease, showing a non-linear response. This can also be called the viscoelastic answer. This behavior is caused by intermolecular interactions and the movement of various polymer side groups. Then plastic deformation occurs. After exceeding the peak strength, the stresses decrease with a simultaneous increase in deformation. This is the phenomenon of strain softening. At higher strains, the stress begins to increase again when the material hardens. In relation to polymers, this phenomenon is called strain hardening. Then it comes back-stress during unloading behavior. This behavior is referred to as kinematic hardening after unloading and it is assumed that this effect is associated with self-stresses, called back-stresses growing internally during the first loading of the material, which facilitates reverse deformation [80, 82].

Differences in nominal and true stress-strain curves are illustrated in Figure 5.3, for samples loaded in the X axis at a strain rate 0.001 s^{-1}.

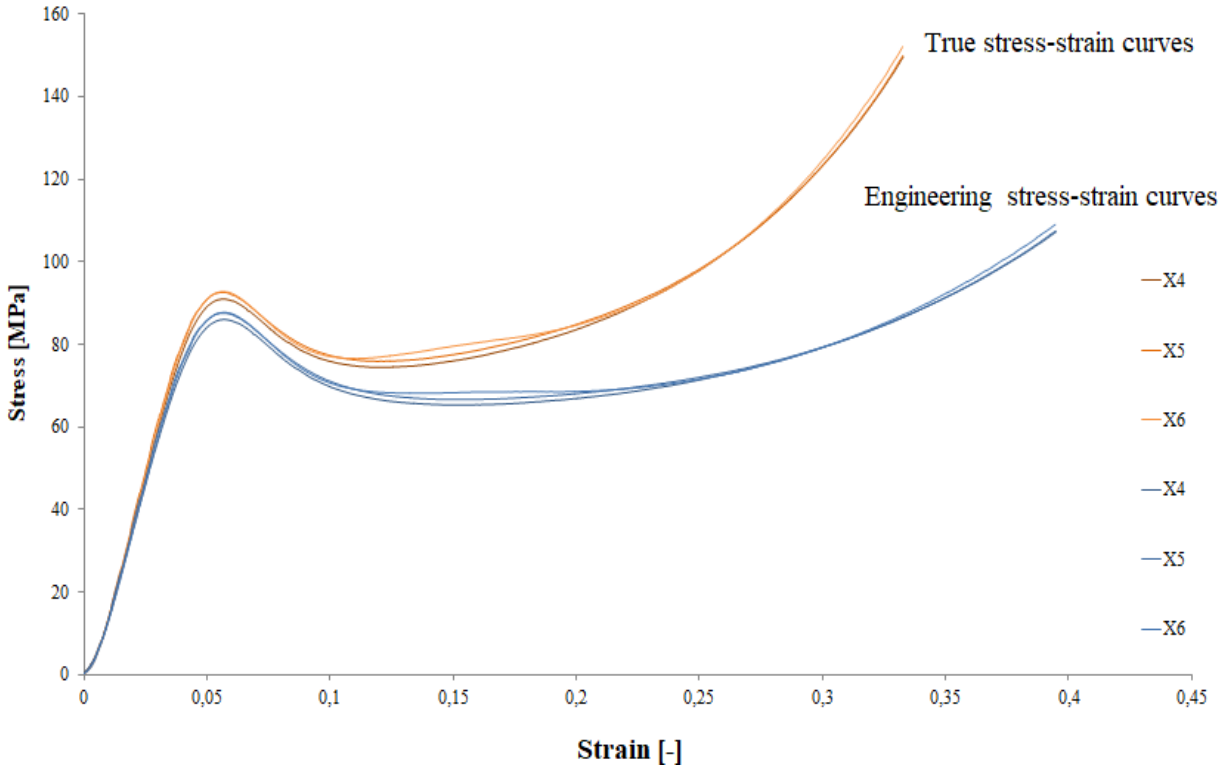

Fig. 5.3. Comparison between nominal and trues stress-strain curves for sample loaded in X-axis at strain rate 0.001 s^{-1} (own source)

Because there is an elastic region on the stress-strain curve, it was possible to determine Young's modulus for all samples. Table 5.2 shows the average values of peak stress and Young's modulus in the case of each type of sample (X,Y, and Z). The exact results for each sample are provided in the table in Annex B.

Table 5.2. Young modulus and peak strength of tested samples (own source)

N° Sample	Young modulus [GPa]	Peak strength [MPa]
X	2.36 ± 0.19	98.71 ± 8.96
Y	2.53 ± 0.21	102.66 ± 11.92
Z	2.55 ± 0.18	99.81 ± 9.15
Mean	2.48 ± 0.21	10.39 ± 9.92

The average value of Young's modulus for samples was 2.48 GPa. The average value of peak strength is 100.44 MPa. It should be noted that peak stress is not a value for compressive strength and cannot be equated. The peak strength value for most samples occurred around 0.05 strain.

5.1.3. Influence of the different strain rates

Curves were generated that included samples manufactured in the same orientation and loaded at different strain rates equal to 0.1, 0.001 and 0.1 s^{-1}.

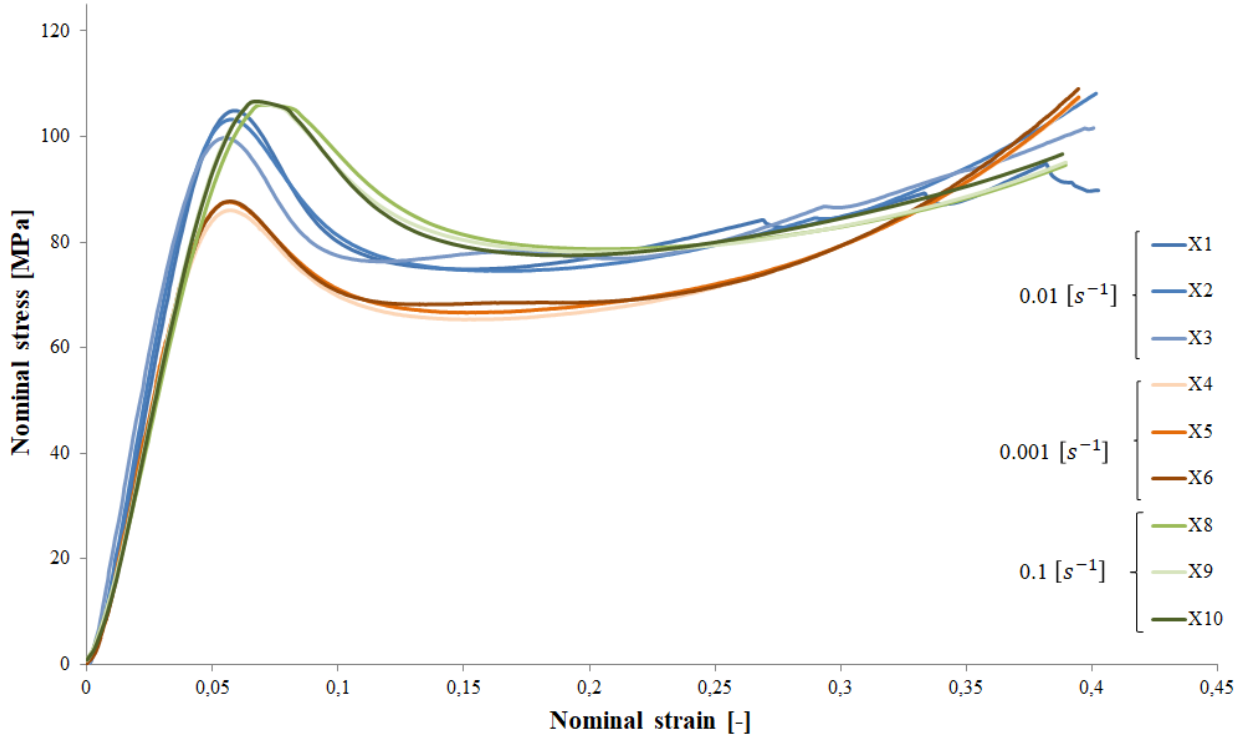

Fig. 5.4. Nominal stress-strain curves of samples 3D printed in X orientation at different strain rates (own source)

In the case of samples loaded in the X-axis, first of all, a clear difference between the peak strength values at different strain rates can be seen (Figure 5.4). For samples loaded at strain rate 0.001 s^{-1} the mean value of the peak stress is 87.11 MPa, for 0.01 s^{-1} the value is 102.64 MPa and for 0.1 s^{-1} the parameter is equal to 106.38 MPa. This means that along with the increase in the strain rates, the peak strength increases. The same phenomenon slightly applies to the average value of Young's modulus, which for strain rate 0.001, 0.01 and 0.1 s^{-1} is 2.26, 2.60 and 2.21 GPa, respectively.

Since the experiments did not always lead to the fracture of the samples, it is difficult to determine the value of the compressive strength of the material. The value of this parameter should correspond to the stress that the sample can withstand before breaking. However, some of the samples broke during the test and this is indicated in the curve by a fluctuation of

stress. For samples that broke the value of compressive strength was determined as the stress just before the break. For samples without cracks, as the value of this parameter, stress at strain equal 0.35 was assumed. For X1, X2, X3, and X6 samples that have burst the value of compressive strength is successively around 85, 86, 79 and 70 MPa (Table 5.3). Samples X4, X5, X8, X9, X10 did not break, so in this case, compressive strength strain was read as a value of stress at strain 0,35. The average value of compressive strength for X samples is 90.89 MPa.

Table 5.3. The compressive strength values for X samples (own source)

	Compressive strength [MPa]	Strain [-]
X1	85	0.28
X2	86	0.30
X3	79	0.16
X4	90	0.35
X6	70	0.12
X5	88	0.35
X8	88	0.35
X9	88	0.35
X10	90	0.35

In the case of samples loaded at a strain rate of 0.01 s^{-1}, fluctuations in the curve covering the plateau section are seen. This was the result of the cracking of the samples under stress, which can be seen in Figure 5.5.

Fig. 5.5. Samples 3D printed loaded in X-axis after compression (own source)

In the samples X1, X2 and X3, cracks appeared along the path of the printer head. In the X1 and X2 samples, the hole is in the middle of the sample, while X3 on the edges. The visible small "peaks" on the curve indicate the moment of the cracking of the sample. Sample X1 also has a specific shape, like barrel shape, and is different from the others, which more closely matches the typical shape of the samples undergoing compression testing.

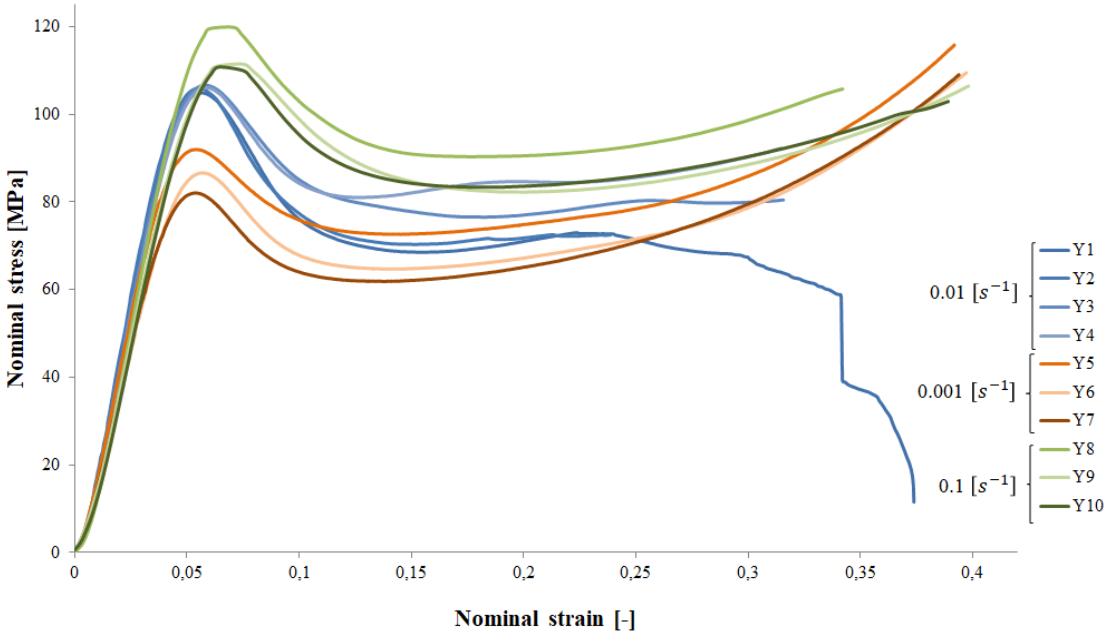

Fig. 5.6. Nominal stress-strain curve of samples 3D printed in Y orientation at different strain rates (own source)

As in the case of samples loaded in the X-axis, the peak strength and Young's modulus of the samples loaded in the Y-axis increases as strain rate increases. The average value of these parameters for strain rate 0.001, 0.01 and 0.1 s^{-1} are 87.86, 105.93 and 114.04 MPa for peak strength and 2.31, 2.70 and 2.51 GPa for Young's modulus, respectively.

The first tested sample Y1 has been completely destroyed, which is clearly visible in the curve, where the significant drop of stress is observed (Figure 5.6). For this reason, for the next three samples tested, the maximum strain value was reduced and an additional sample was tested for a strain rate of 0.01 s^{-1}. For sample Y1 it is possible to determine the compressive strength value and it is equal to about 70 MPa (Table 5.4). In Y2, Y3 and Y4 samples there are cracks, which also result in fluctuations in stress-strain curves. In Y2 and Y3 samples, cracks are on the edges and Y4 inside (Figure 5.8). Assuming the value of compressive strength as stress before the appearance of a crack in the sample for Y2, Y3, and Y4, the value of this parameter is approximately 70, 85 and 89 MPa. Samples strained in the direction of the Y-axis at a strain rate 0.001 s^{-1} were not destroyed.

The Y8 sample loaded at the strain rate 0.1 s^{-1} was twisted and its shape resembles the Y2, Y3, and Y4 specimens. Y6 and Y7 samples have a barrel shape, while the rest of them are deformed in the shape of the letter "X" (Figure 5.7).

Table 5.4. The compressive strength values for Y samples (own source)

	Compressive strength [MPa]	Strain [-]
Y1	72	0.18
Y2	72	0.23
Y3	80	0.26
Y4	83	0.17
Y5	98	0.35
Y6	90	0.35
Y7	90	0.35
Y8	106	0.35
Y9	92	0.35
Y10	93	0.35

Fig. 5.7. Samples 3D printed loaded Y-axis after compression (own source)

In the curves of samples loaded in the Z-axis, it can also be seen that peak stress increases along with the strain rates (Figure 5.8). The average parameter values for the strain rates 0.001, 0.01 and 0.1 s^{-1} are 88.62, 100.45 and 107.71 MPa.

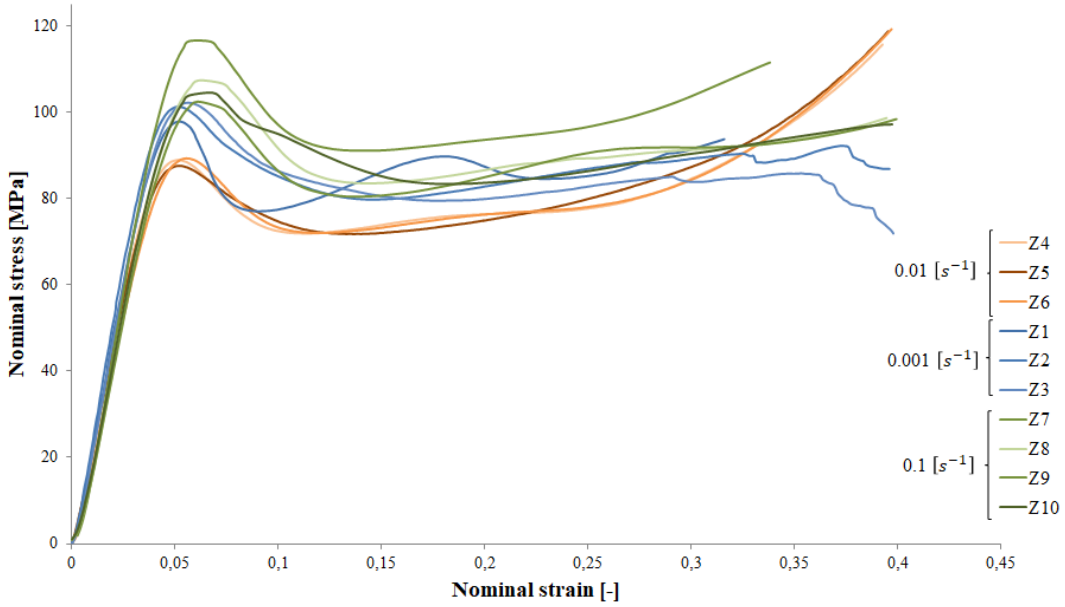

Fig. 5.8. Nominal stress-strain curve of samples 3D printed in Z orientation at different strain rates (own source)

The Young's modulus also increases as the strain rate increase, and the average values are 2.39, 2.68 and 2.57 GPa. Again samples loaded at strain rate 0.001 s^{-1} were not destroyed. The peak strength value for the Z7 sample is much higher than for the reserve of samples loaded at the strain rate 0.1 s^{-1}. The test conditions may have influenced this, as the tests on Z8-Z10 samples were done at significantly higher temperatures. As in the X and Y samples, in the Z samples at strain rate 0.01 s^{-1} cracks have appeared and this is noticeable on the stress-strain curves, on which the fluctuation of the lines can be seen. The pre-fracture stresses for Z1, Z2, and Z3 samples were approximately 90, 87 and 85 MPa, respectively (Table 5.5). The values of the same parameters for samples Z8, Z9, and Z10, which also cracked during loading at a strain rate of 0.1 s^{-1} were 89, 87 and 98 MPa, respectively. Almost all of the samples were deformed in a similar way, that is, they adopted a similar shape after the tests (Figure 5.9).

Table 5.5. The compressive strength values for Z samples (own source)

	Compressive strength [MPa]	Strain [-]
Z1	85	0.15
Z2	90	0.27
Z3	85	0.30
Z4	72	0.14
Z5	99	0.35
Z6	72	0.14
Z7	95	0.23
Z8	90	0.23
Z9	92	0.24
Z10	98	0.08

Fig. 5.9. Samples 3D printed loaded in Z-axis after compression (own source)

5.1.4. Influence of printing orientation

In this part, curves were generated for samples manufactured rinted in different orientations but loaded with the same strain rate. The goal was to show the effect of printing orientation on the mechanical response.

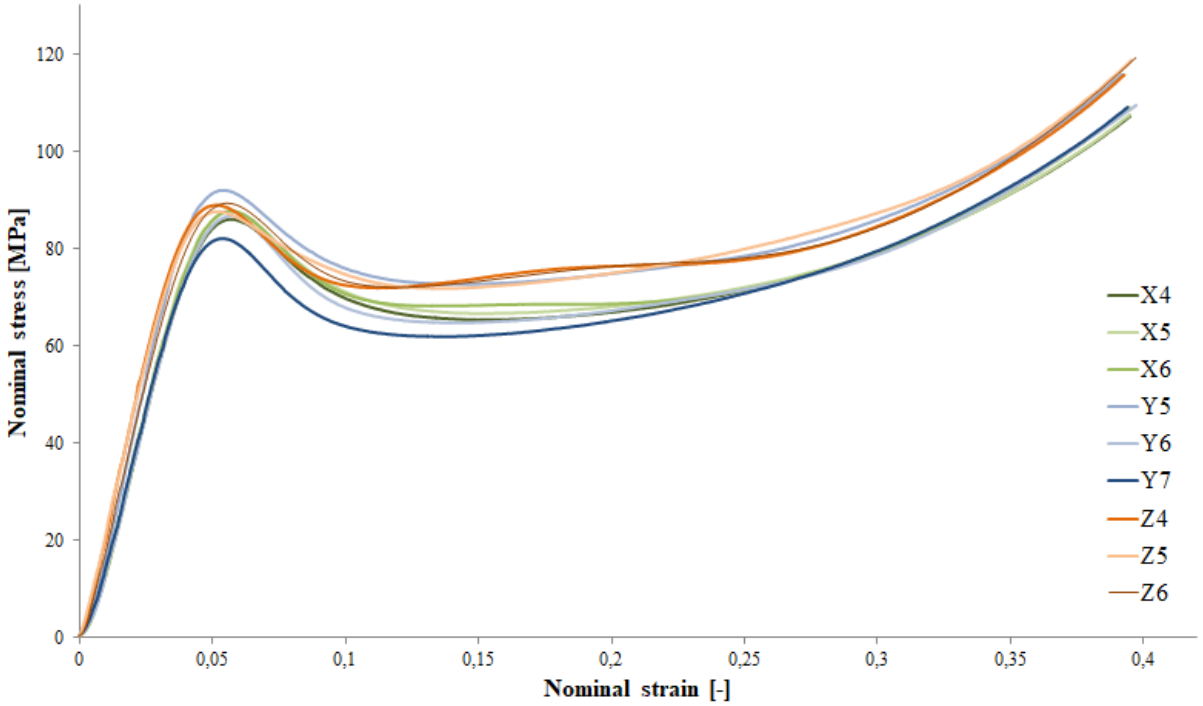

Fig. 5.10. Nominal stress-strain curve of samples 3D printed in different orientation at rates strain rate 0.001 s^{-1} (own source)

The stress-strain curves of all samples loaded with a load speed of 0.001 s^{-1} have a similar profile (Figure 5.10). The differences are virtually unnoticeable, especially in the elastic region, until the strain of approximately 0.05 the curves practically overlap. The peak strength values, in this case, are very similar to each other and the average value are about 87.54 MPa. The same applies to Young's modulus, whose average value is about 2.32 GPa. The curves for samples prin manufactured ted in the same orientation are similar except for samples loaded in the Y axis. In this case, after the peak stress, the stress difference at the same strain value is significant, in particular for the Y5 sample for which the peak strength is much higher than for the sample with the same printing orientation Y7. It can be seen in Figure 5.12 that the appearance of the X, Y, and Z loaded samples is similar and the deformation is small. In most cases, samples have barrel shapes.

Fig. 5.11. Samples loaded in X, Y, and Z orientation after compression a strain rate 0.001 s^{-1} (own source)

In the case of loading samples in three directions at a strain rate of 0.01 s^{-1}, differences in the elastic region are also small (Figure 5.12).

The behaviour of the Y samples is slightly different from the other directions as the peak stress values for Y-weighted samples are higher than those compressed in the X and Z axes. Most of the samples, regardless of orientation, were destroyed and cracked (Figure 5.13). In most cases of broken samples, the cracks appear along with the material application direction during production. Samples X1 and X2 differ in shape from the others and have a barrel shape. The variant also applies to the cracks that were found inside of these samples.

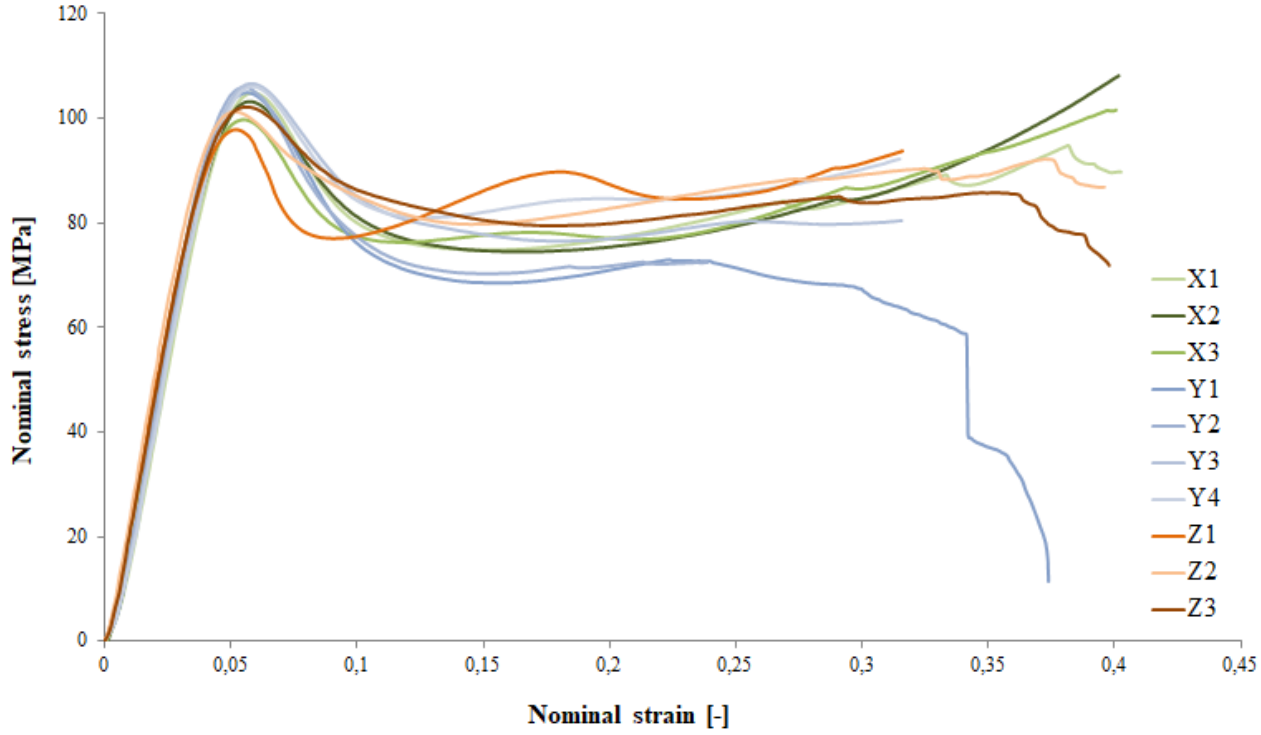

Fig. 5.12. Nominal stress-strain curve of samples 3D printed in different orientation at rates strain rate 0.01 s^{-1} (own source)

Fig. 5.13. Samples loaded in X, Y, and Z orientation after compression a strain rate 0.01 s^{-1} (own source)

Figure 5.14 shows the stress-strain curve for all samples at strain rate s^{-1}, where a small effect of orientation may be visible. In the elastic region, slightly larger differences are noticeable than in other strain rates.

Samples loaded in the Y axis have higher values of the stresses than in the Z and X axes. The samples loaded in the X and Y axis at this strain rate were not destroyed in contrast to samples loaded in the Z axis. All samples deformed in a similar way (Figure 5.15).

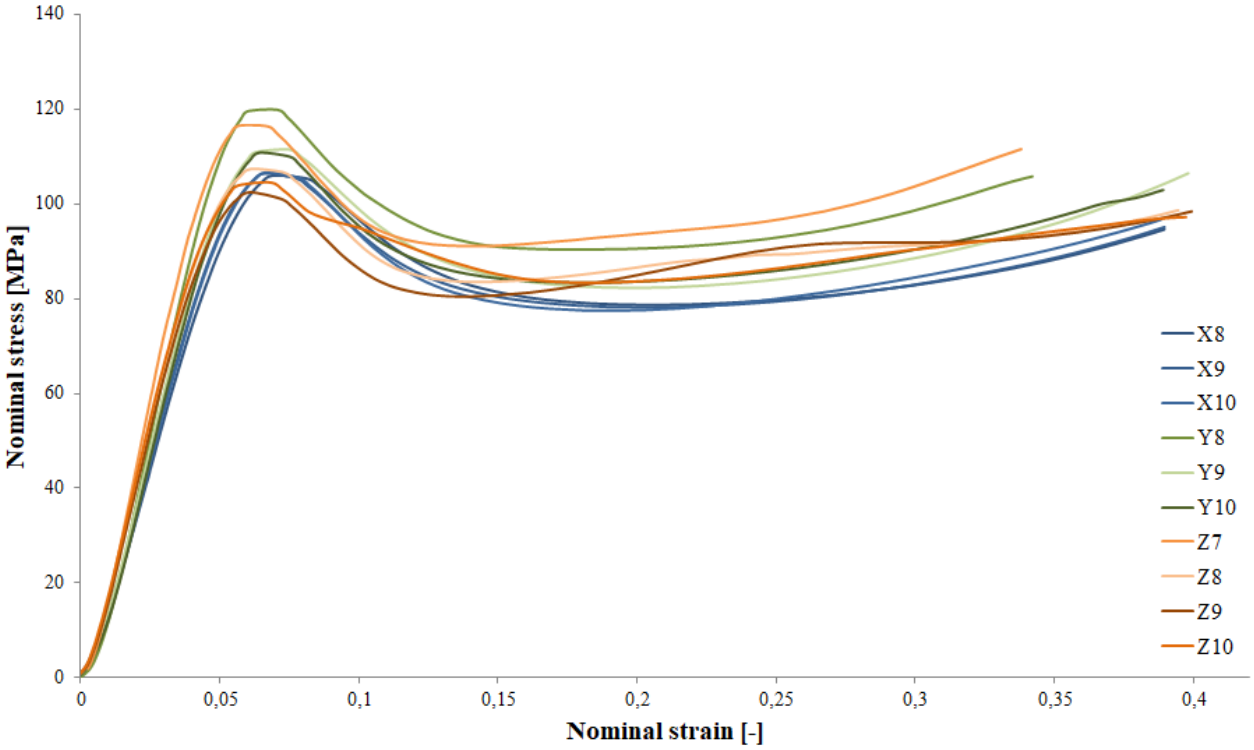

Fig. 5.14. Nominal stress-strain curve of samples 3D printed in different orientation at rates strain rate 0.1 s^{-1} (own source)

Fig. 5.15. Samples loaded in X, Y, and Z orientation after compression a strain rate 0.1 s^{-1} (own source)

5.1.5. Compression test with unloading

Table 5.6 presents the dimension, weight, and parameters calculated on their basis for samples used for compression test with unloading.

Table 5.6. Measured and calculated parameters for cubic samples (own source)

N° Sample	Dimension [mm]			Cross section area [mm²]	Weight [g]	Volume [mm³]	Density [g/cm³]
	length	width	high				
X2	9.99	10.02	9.99	100.07	1.15	999.33	1.15
X3	10.03	10.00	9.99	100.33	1.16	1002.67	1.16
X4	10.05	9.91	9.94	99.60	1.15	990.31	1.16
X5	10.03	10.01	10.00	100.47	1.15	1004.67	1.14
Mean	10.03	9.99	9.98	100.12	1.15	999.24	1.16

Figure 5.16 shows the characteristic curves obtained as results of the loading of the cubic samples. The shape of all curves is identical. The X4 sample has much lower stress values than the rest, but no clear reason for this phenomenon has been found. It is possible that a mistake was made in the axis designation along which the sample was loaded, however, after testing, it was impossible to read the framework from the sample wall. In each case, significant non-linearity during unloading can be seen. In the beginning, when analyzing compression tests without unloading, it was not possible to state the viscoelastic behaviour.

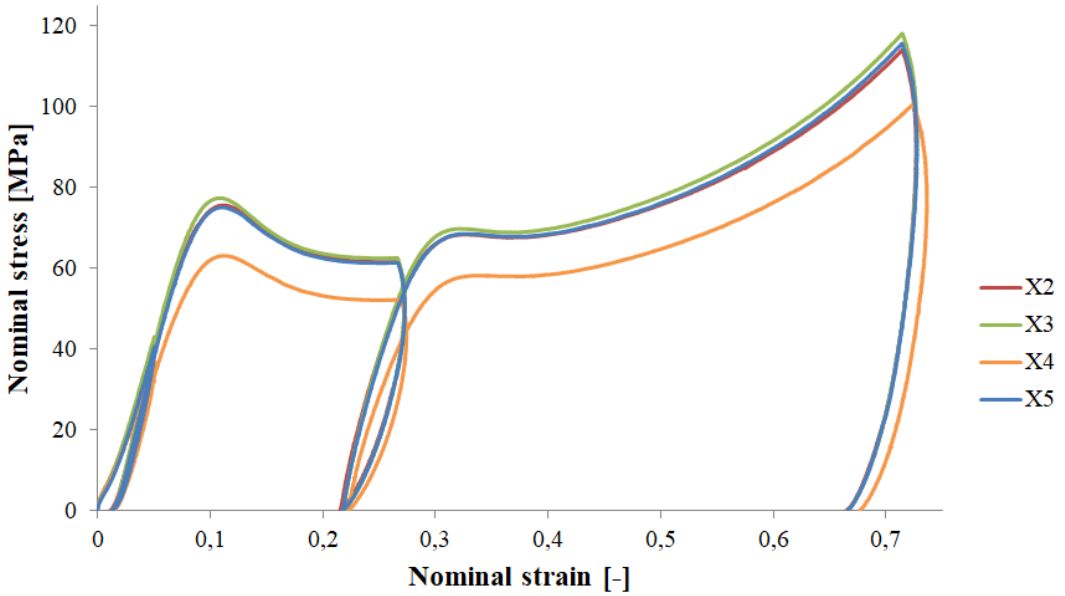

Fig. 5.16. A stress-strain curve in compression test with the unloading of one of the cubic sample at strain rate 0.001 s^{-1} (own source)

Figure 5.17 shows samples after performing the compression test with unloading. All samples deformed in the same way, flattened and took a barrel shape.

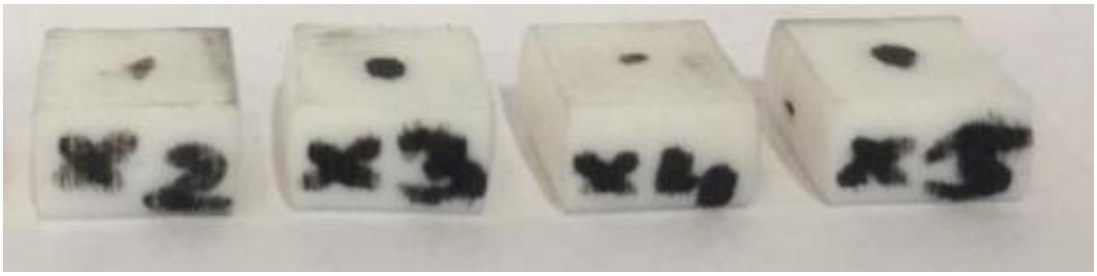

Fig. 5.17. Samples after compression test with the unloading (own source)

5.2. Machining test results

5.2.1. Influence of printing orientation

For drilling, the force values are more important than the torque values. The torque values during the drilling of the tested material were so small that it was impossible to analyze them because they could only be interferences. Therefore, the results are presented for forces only (Figures 5.18, 5.19, 5.20). In order to investigate the effect of the print orientation on the results, the data from these 4 consecutive tests were plotted together and compared. Curves were generated for all sets of parameters of cutting speeds and feed rates.

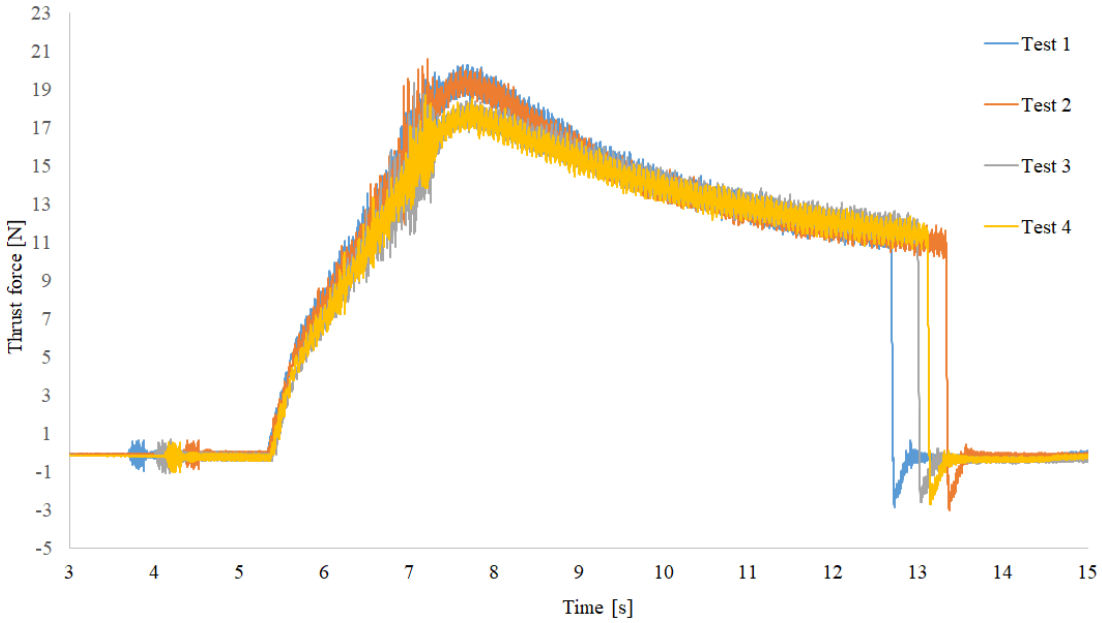

Fig. 5.18. Plotting of thrust force measurements for 4 consecutive drilling tests on Verowhite at v_c = 10 m/min and f = 0.04 mm/rot (own source)

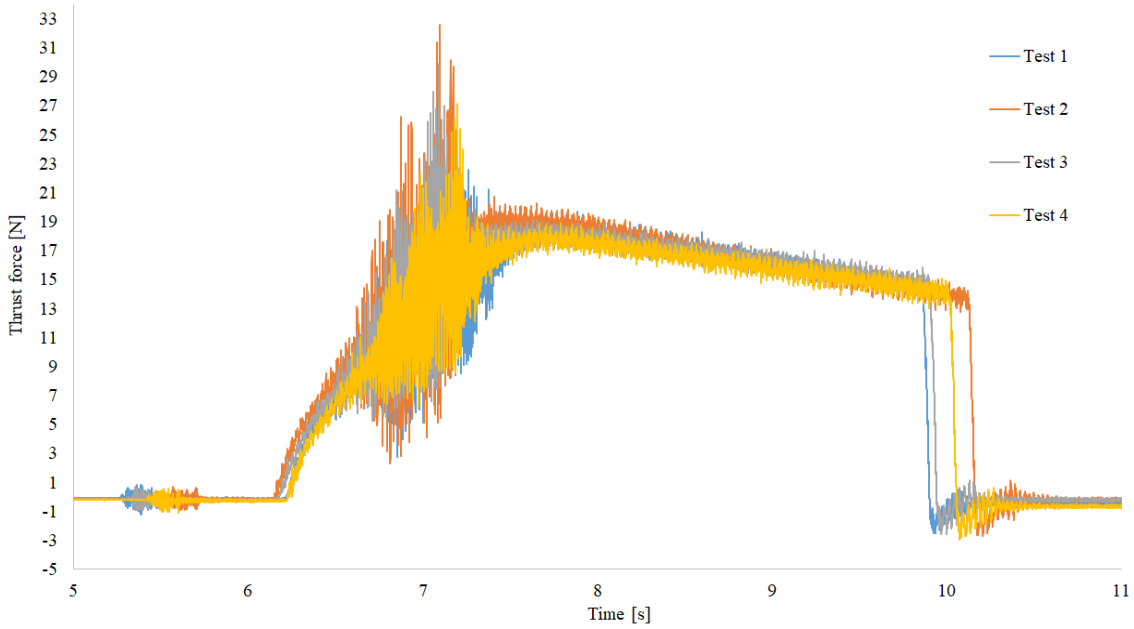

Fig. 5.19. Plotting of thrust force measurements for 4 consecutive drilling tests on Verowhite at v_c = 20 m/min and f = 0.04 mm/rot (own source)

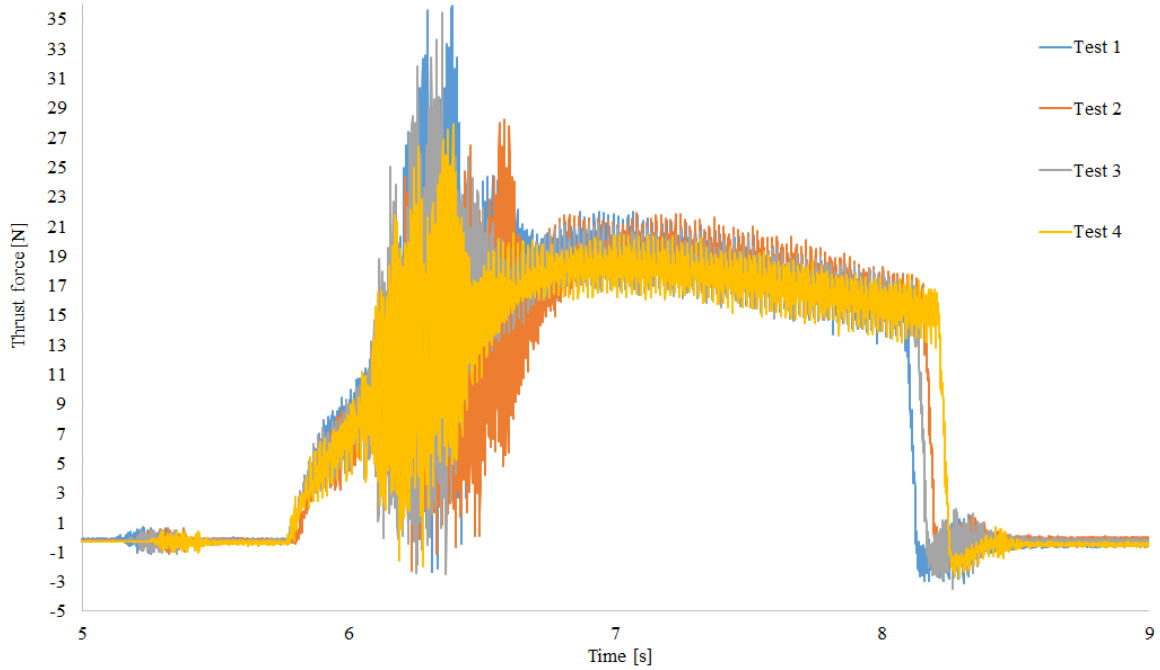

Fig. 5.20. Plotting of thrust force measurements for 4 consecutive drilling tests on Verowhite at v_c = 32 m/min and f = 0.04 mm/rot (own source)

As can be seen in the figure, the differences between individual measurements are not significant. The orientation of 3D printed samples is not very important for mechanical response to drilling.

5.2.2. Comparison with bone samples

The purpose of the drilling tests was to compare the results to tests on bone samples that were previously made under similar conditions. Alexis Jacquillard performed a drilling test for samples of femoral diaphyseal porcine bone using a CNC machine [81]. In this study, the axial force was measured during testing with a feed of 40 µm/rot and cutting speeds of 10, 20 and 32 m/min, which can be compared with the test done on the VeroPureWhite samples. For drilling in the test, a dental drill with a 3.2 mm drill diameter was used and the drilling depth was equal to 4 mm. Figure 5.21 shows axial efforts curves during the drilling of VeroPureWhite (on the test bench) and bone (on the CNC). It is clearly visible that the behavior of the polymer material under drilling is similar to bone behavior. There is a rapid increase of efforts before the plateau phase. The maximum value for thrust force for cutting speed 10 and 20 m/min is 17 N for VeroPueWhite and around 19 N for bone.

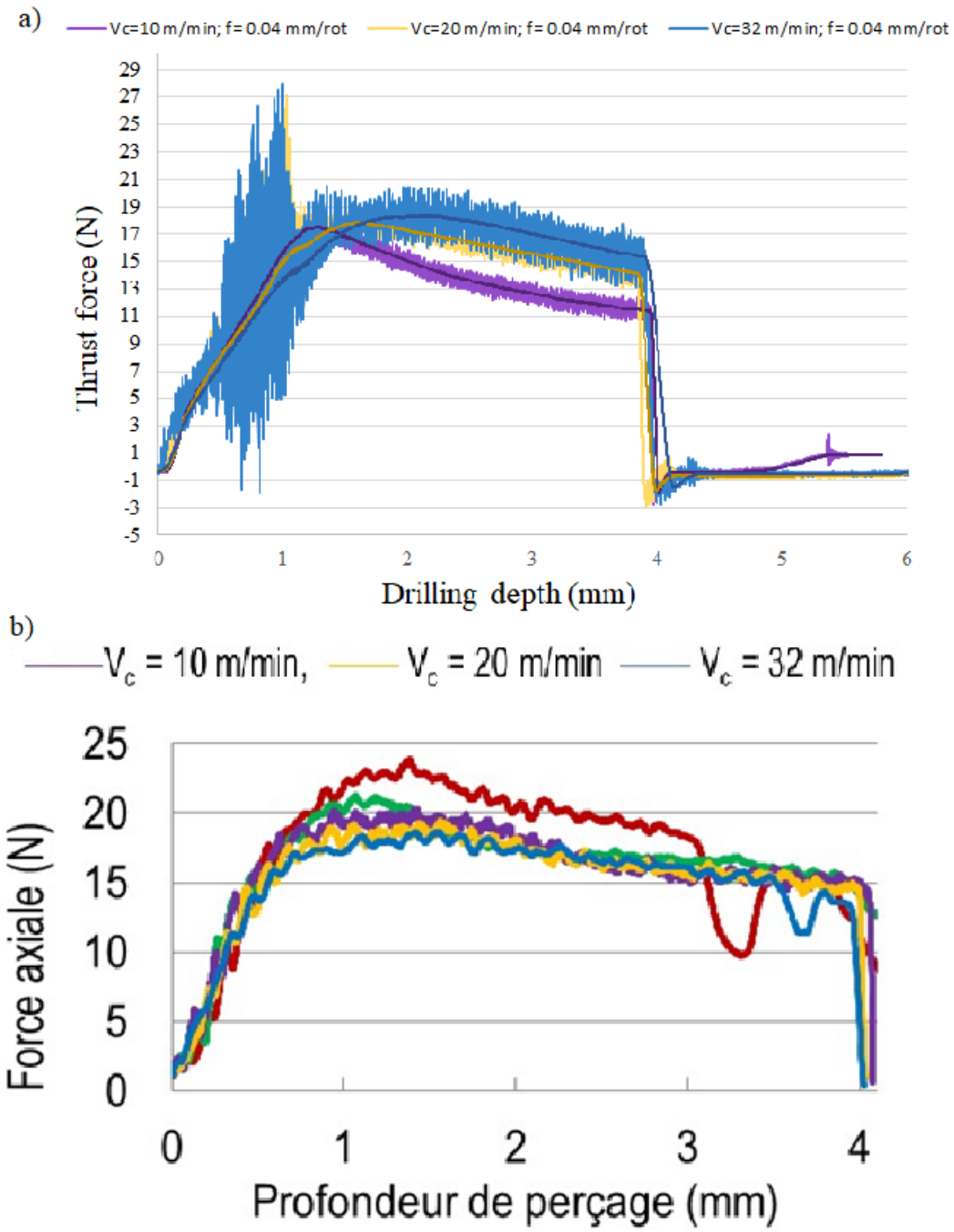

Fig. 5.21. Comparison of thrust force measured between : a) VeroPureWhite on the left (own source), b) bone sample on the right [81] with Vc = 10, 20, 32 m/min and f=0.04 mm/rot

The results obtained on the VeroPureWhite material can also be compared with the results obtained in studies carried out by Amewoui et al., submitted to Medical Engineering and Physics Journal in 2019 [85]. The study measured both forces and torque arising during porcine cortical bone drilling. The test used cutting speed equal to 2, 5, 10 and 20 m/min at a

feed rate of 0.04 mm/rot. Figure 5.22 shows a comparison of the thrust forces and Figure 5.23 torque for tests performed on samples of polymer material and bone. Thrust force results for cutting speeds of 10 and 20 m/min are very similar to those obtained on the test bench, with the same evolution of efforts throughout the drilling with a rapid increase up to a plateau, followed by a reduction of efforts. This could be caused by the temperature rise. In contrast, torque measurements made on VeroPureWhite samples had a lower amplitude than the results obtained for bone. The maximum value of torque for VeroPureWhite is equal to approximately 0.05 Nm, while for porcine bone it was 0.09 Nm.

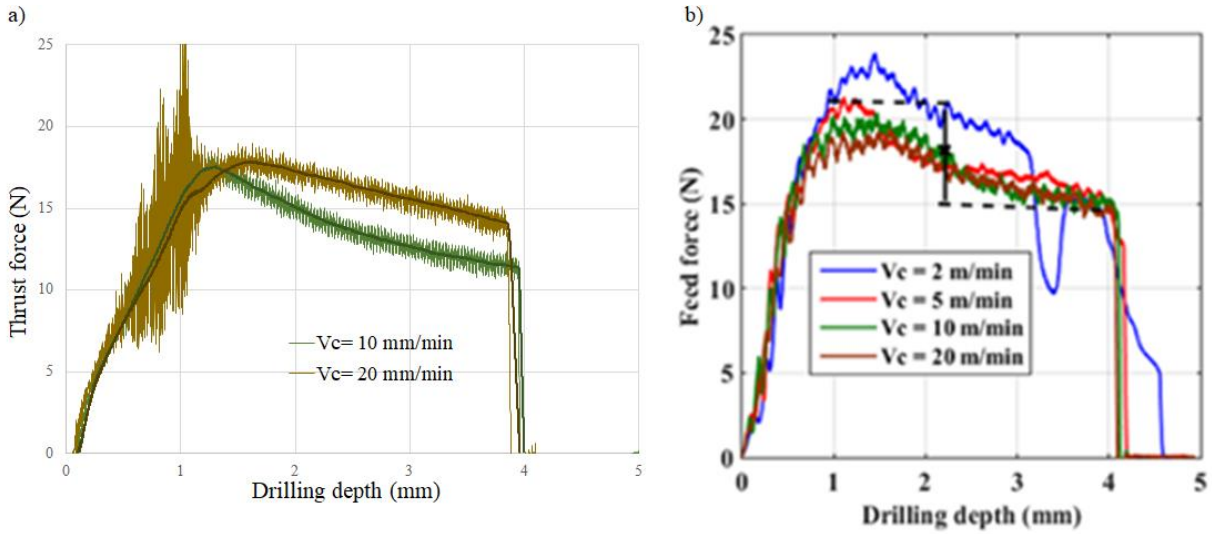

Fig. 5.22. Comparison of axial force acquired for: a) VeroPureWhite (own source) , b) porcine bone samples [85] with Vc = 10; 20 m/min and f = 0,04 mm/rot

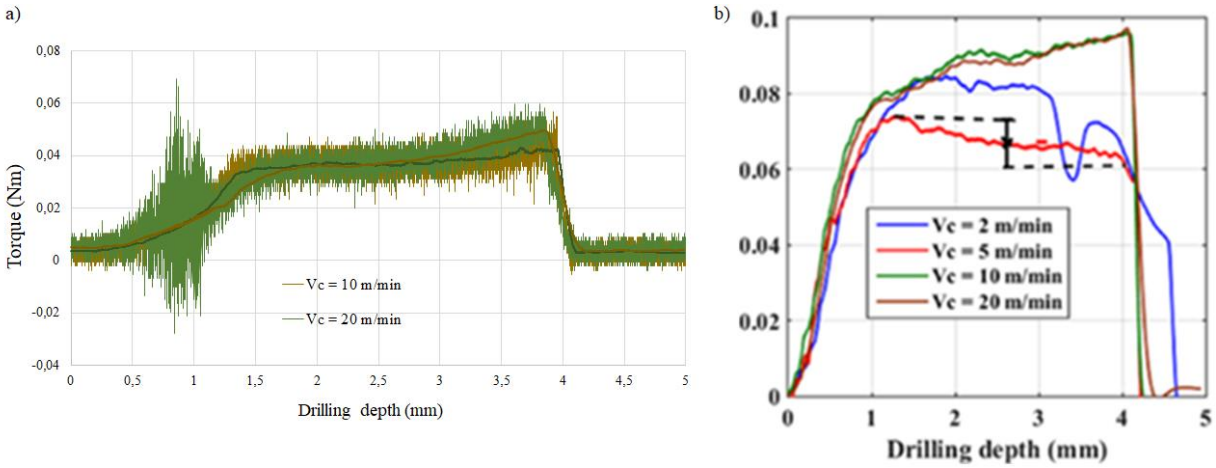

Fig. 5.23. Comparison of torque acquired for: a) VeroPureWhite (own source), b) bone samples [85], with Vc = 10; 20 m/min and f = 0,04 mm/rot

A very important issue when drilling bones is the formation of chips that cause limited visibility of the operating area. In addition, the surgeon's health is at risk due to the inhalation of dust. During drilling of the VeroPureWhite material, a lot of chips were also formed. The influence of the cutting speed on the formation of chips could also be noticed. The faster the values of cutting speed, the chips were less. In Figure 5.24, the chips formed at the cutting speed are visible - they wrap around the drill.

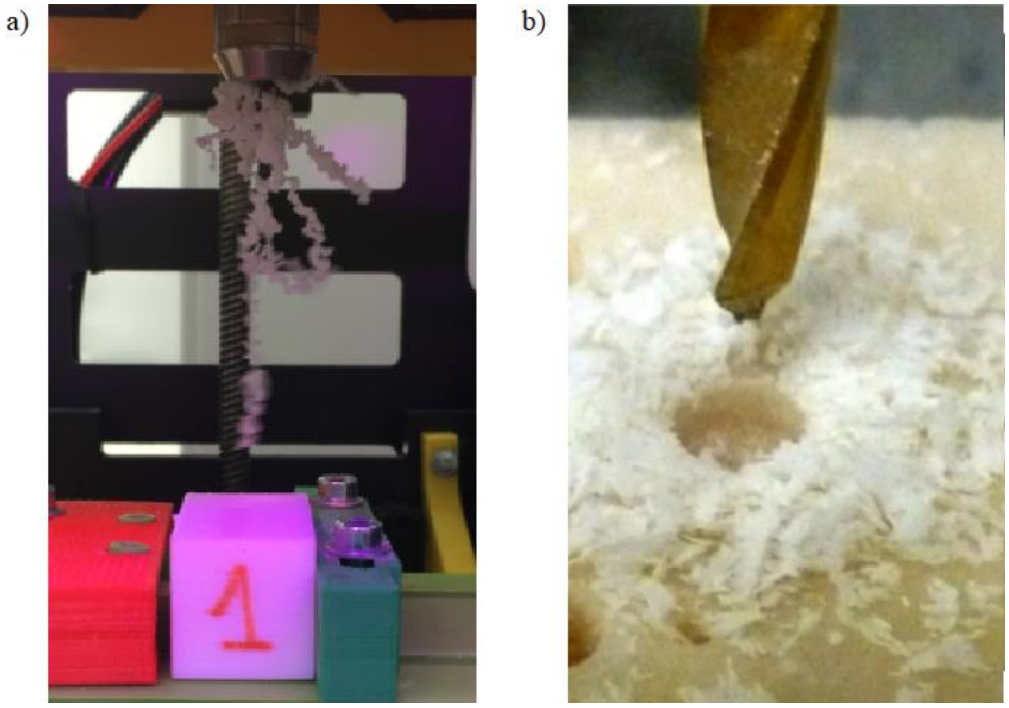

Fig. 5.24. Chips created during drilling: a) sample of VeroPureWhite material (own source), b) the bovine cortical bone [50]

5.3. Results discussion

5.3.1. Mechanical test results discussion

The dimensions of the samples of the tested VeroPureWhite material do not deviate significantly from the intended dimensions given to the manufacturer, and measurement errors are less than 0.5%. The average values of the sample dimensions do not differ much from the intended dimensions given to the manufacturer for their production. The percentage

error of the measurement for the width is 0.39%, for the length only 0.16% and for the height of 0.12%. The average density equal to 1.17 g/cm³ calculated for all samples corresponds to the range given by the manufacturer.

The stress-strain curve for all samples had the same shape including elastic region, peak stress and strain softening. After the softening phase, some of the curves had fluctuations, which was the result of the samples breaking. This applied mainly to samples loaded in the Y direction.

For nominal and true stresses and strains, the results for the other samples were similar. True stresses have higher values than nominal stresses at the same strain values but the elastic region curves overlap.

The Young's modulus values between the specimens were also similar. According to the manufacturer modulus of elasticity should be in the range of 2 to 3 GPa and the average of this parameter for all samples was equal to 2.48 GPa, so the result coincides with the assumptions It was not possible to determine the compressive strength for all samples, as it is not known exactly at which point the sample broke. Only one Y1 sample has been destroyed and the value of this parameter can be determined for it.

The influence of strain rate on the mechanical parameters of the material can be observed on the basis of the curves. The peak strength and Young's modulus increase with increasing strain rate. Additionally, it is visible that for a strain rate of 0.001 s^{-1} the results are more stable than for 0.01 s^{-1} and 0.1 s^{-1} At strain rate 0.01 s^{-1} the samples manufactured in each direction were bursting.

The influence of the orientation of printing the samples can also be slightly noticed. Samples loaded in the Y-axis have higher peak stress at the same strain rates compared to samples loaded in the X and Z axis. Z-samples have slightly higher peak strength values than X. The most unstable results were obtained for samples loaded in the Y-axis, transverse to the direction of application of the material during manufacture.

All samples Y cracked during the test. There is also a large difference between the results for the same print orientation. For samples Y, the difference between stresses at the same strain rate was the highest. In the case of X and Z samples, the differences were not so large, but they did exist. This indicates that the process of producing samples was not repetitive and their behavior is slightly different despite the same orientation of printing.

Samples deform in different ways during the compression tests. In the case of polymers, the most common shape is the barrel shape when the sample begins to bulge outward on the

sides. The frictional force is not constant for the entire cross-section of the specimen. Due to this, when the sample reaches the shape of the barrel there is a phenomenon called barrelling. A uniform compression of the sample would occur in the absence of friction, which in practice is difficult to achieve [82, 83, 84].

Samples after the test took a different shape and it was either a barrel shape or an "X" shaped pattern. Cracks appeared on the edges or inside the specimens. However, in any case, the cracks were along the direction of material application through the printer head. At a strain rate of 0.01 s^{-1}, it can be observed that all samples have been damaged, but in different ways and one of them has even been completely destroyed. Again, the innaccuracy of the production process can be a reason behind it.

In the case of a compression test with unloading, again, the dimensions of the samples did not differ significantly from the intended dimensions given to the manufacturer. The percentage error for length was 0.25%, for width 0.13%, and for high 0.19%.

It can be concluded that the VeroPureWhite material has viscoelastic behavior. In the observation of viscoelastic phenomena, the important role is played by time. After unloading stresses and strains begin to decrease as time passes. After removing the force the material slowly begins to return to the previous dimensions. The sample, however, does not reproduce its original length, because, during the deformation stress, the material flow has occurred, causing plastic deformation (Figure 5.18).

5.3.2. Comparison of mechanical properties of VeroPureWhite and cortical bone

Based on the literature, the density of the temporal bone is approximately 1.8 g/cm³, which is a higher value than the result obtained for the tested material, which is equal to 1.17 g/cm³ [70]. Young's modulus for cortical temporal bone is equal to 10.39 GPa (Table 4.1), which significantly exceeds the value obtained for the VeroPureWhite material equal to 2.50 GPa. However, it should be noted that the temporal bone has a relatively high elastic modulus compared to other skull bones. The compressive strength value for the temporal cortical bone is equal to 152.24 MPa [47]. Unfortunately, during the test, it was difficult to determine the specific compressive strength value for the samples, because each of them was cracked in various places, and only one was completely destroyed. The average value of compressive strength for samples with cracks was 82.71 MPa manufactured in three directions that did not break was 92.82 MPa. The mean value of this

parameter for samples with cracks was 82.71 MPa and because this value is higher than for fracture samples, it has been used to compare the compressive strength of polymeric material to cortical bone. From the datasheet of materials, the tensile strength for VeroPureWhite, which is equal to 50-65 MPa, can be read and this value is less 10 MPa lower than for the temporal bone. PolyJet bending tests were not carried out, but the manufacturer gives information about flexural strength. The value of this parameter is in the range from 75 to 110 MPa, which coincides with flexural strength for cortical temporal bone [70]. Comparison of the parameters of the tested VeroPureWhite material resulting from compression tests and from the datasheet manufacturer is presented in Table 5.7. The values in the table shown below for temporal bone were taken from Table 4.2 and are the average of the values found in the literature.

Table 5.7. Comparison of the parameters of material VeroPureWhite and temporal bone [59, own source]

	VeroPureWhite compressive tests results	VeroPureWhite from datasheet	Temporal bone
Compressive strength [MPa]	92.83	-	152.24
Tensile strength [MPa]	-	50-65	72.52
Flexural strength [MPa]	-	75-110	82.00±25.50
Young Modulus [GPa]	2.50	2-3	10.39
Density [g/cm³]	1.17	1.17-1.18	1.8
Rockwell Hardness	-	73-76	-

The cortical bone is an anisotropic material, therefore, the mechanical properties vary depending on the direction of the load. The stiffness and strength are higher when the direction of the osteons coincides with the load direction. This was proven by O. Mayeur et al. in their research, subjecting the cortical bone to compression tests in four loading directions (Figure 5.25) [87].

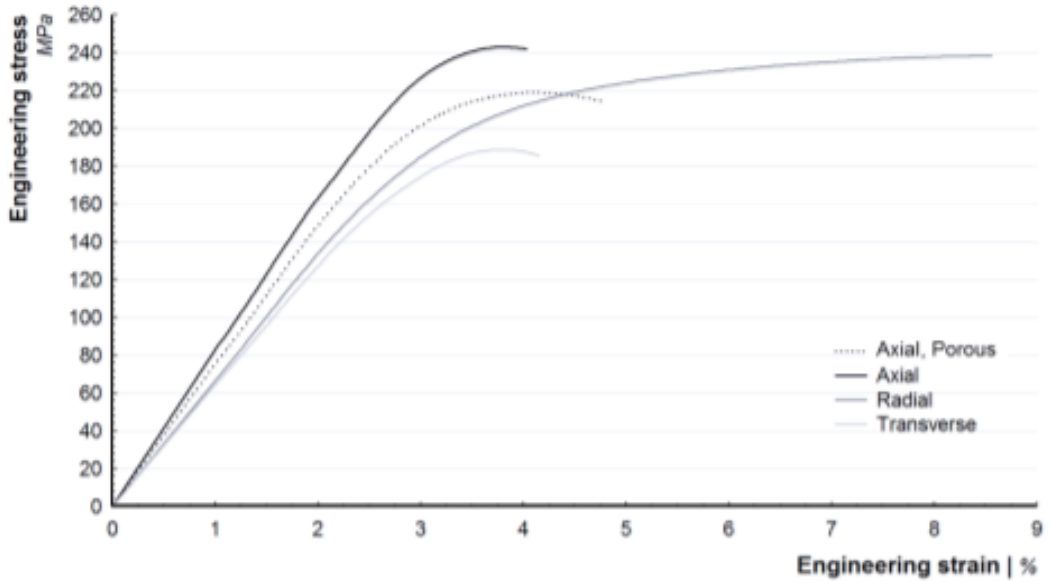

Fig. 5.25. Stress-strain curves of cortical bone of bovine femur in the compression function of the 4 loading direction configuration at strain rate 0.05 s^{-1} [86]

For the cortical bone, it was proven that the direction of the load affects the mechanical properties. To prove the similarity of the results with respect to the direction of the load between the cortical bone and the VeroPureWhite material, a certain condition would have to be met. The stresses obtained as a result of loading the tested VeroPureWhite samples in the axis along which the material was applied during printing should have the highest results. Material during the printing of samples was applied in the direction of the X axis, which means that the load along this axis should give the highest stress results. The results show that the samples loaded in this axis usually have the lowest stress values. Figure 5.26 shows an example of samples manufactured in different orientations but loaded at a strain rate of 0.001 s^{-1}. For this reason, it is not possible to determine the relationship between the material and the bone in this matter. Based on the results obtained for the VeroPureWhite, it appears that the direction of the print has some influence on the mechanical response, but it has not been proven directly that the material shows anisotropy [33].

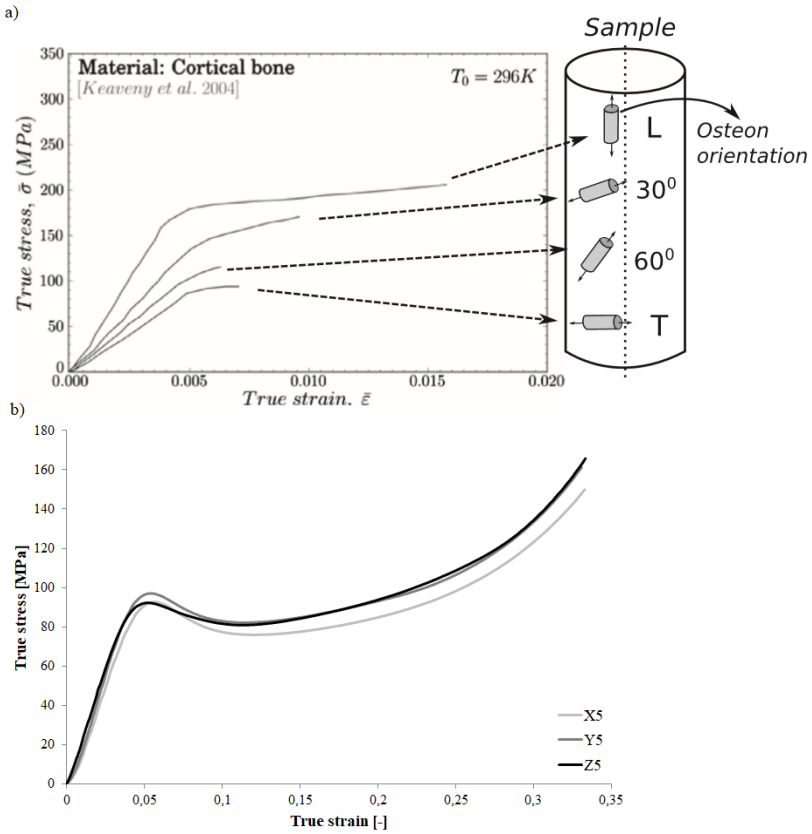

Fig. 5.26. The stress-strain curves obtained as a result of compression test: a) influence of osteon orientation on the mechanical behavior of bone [33], b) VeroPureWhite (own source)

The results for the cortical bone loaded in the room temperature compression test showed the dependence of the strain rate on the mechanical properties. The impact of the strain rate on strength is illustrated in Figure 5.28. The maximum stresses and Young's modulus have raised with increasing strain rates. The curve in Figure 5.28a shows the mechanical response of the cortical bone to the same strain rates as those used during the study on the VeroPureWhite material. The polymer material also showed an upward trend in maximum stress as the strain rate increased. The shape of the curve differs from the curve obtained for human bones. However, note the scope of the strain, because the cortical bone is shown for small strain values up to 0.020. The cortical bone has much higher values of true stress than VeroPureWhite with a very small strain. For a true strain equal to about 0.005 the true stress for cortical bone is around 80 MPa at strain rate 0.001 s^{-1}, while for the polymer for samples showed in Figure 5.27 the same value of stress is reached at strain equal to 0.04. It is not possible to see what character the curve has at higher values of strain in case of cortical bone. In the elastic region, the curves almost overlap each other in the case of VeroPureWhite,

while for the bone from the beginning the difference in stresses can be seen. In addition, in case of the cortical bone in quasi-static condition, there is no softening [33].

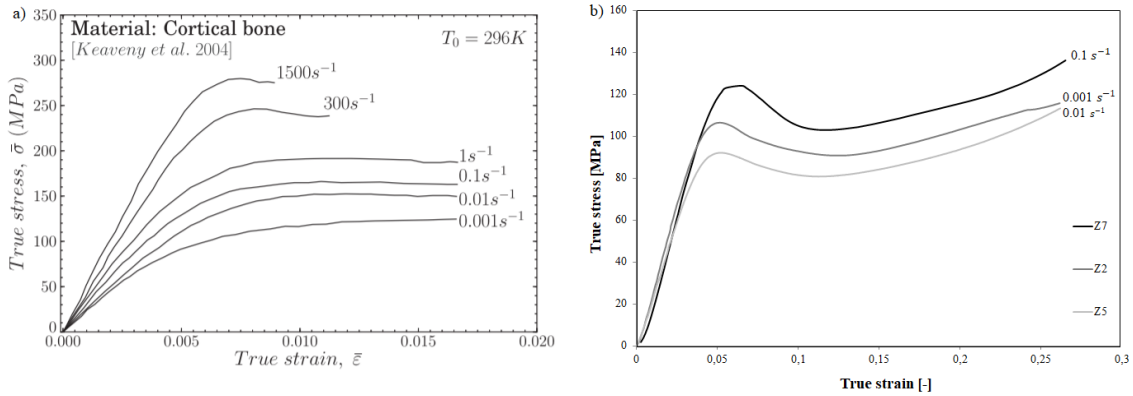

Fig. 5.27. Stress-strain curve as a function of strain rate obtained from compression tests: a) cortical bone [86], b) VeroPureWhite (own source)

As previously mentioned, the bone is viscoelastic. The results of the compression test with unloading on the cubic samples prove that the VeroPureWhite material is also viscoelastic. In this case, it is one of the common features between the cortical bone and the tested material.

5.3.3. Machining test results discussion

It can be concluded that the VeroPureWhite material shows a very similar mechanical response to drilling as porcine bone, especially in terms of the axial force produced. These results are very promising for the development of a new anatomical model, as they make VeroPureWhite a potentially adequate material for the replication of real bone drilling haptic. However, it is important to relativize these results, as the test bench with which both characterizations were done was different. Moreover, these results were obtained with porcine femoral bone, which response may differ from the human temporal bone. Therefore, to make results more reliable, more tests should be performed, starting with human temporal bone tests on the developed test bench.

In fact, the rotation of the otological drill is very fast, so in the future, it would be good to test in dynamic conditions because it would correspond to more real surgery. During bone drilling, dust is generated that can irritate the surgeon's distal cord. For this reason, during a real surgery, the area of operation is poured over with special water. In addition, the drill produces heat. Therefore it is necessary to examine the thermal effect of drilling the tested material VeroPureWhite.

Summary

The aim of the study was to find a material suitable for printing a model for training surgeons. All the activities stated in the research plan were realized with success. However, due to the limitations of the model requirements, it was a very difficult process. Models intended for surgical training are very important, because only in this way they can improve their skills. Models should have appropriate properties to mimic the temporal bone and the inner ear elements both visually and mechanically to the greatest extent possible. That is why it is so important to find a suitable material that has a mechanical response that is the most similar to the bone.

Limitations of the material selection are related to production technology. Most of the pre-surgical models are produced using additive techniques. The temporal bone model is to be manufactured out of two materials with different properties. One material should imitate the cortical bone and the other one – the soft tissue. Therefore, the selected 3D printer must be able to print two materials at the same time. In addition, due to the small structures of the middle ear must have a very good resolution. The only readily available technology that meets both conditions is the PolyJet.

One of the important conclusions obtained on the basis of mechanical tests is that the manufacturing process is not always perfectly repeatable. The orientation of the printing affects the mechanical behavior of the material. The research was aimed at finding the dependence of the VeroPureWhite on the cortical bone in the aspect of the anisotropy, but at the moment no similarities were found. Although the material has many similarities to bone behavior, such as dependence on the effect of strain rate and viscoelastic behavior, this is not enough to decide on its use.

Mechanical tests allow the determination of parameters such as Young's modulus or maximum stresses. The mechanical response of the material intended for the temporal bone model is not ideal compared to the bone properties. Stiffness and strength of the material are lower than for the temporal cortical bone. The VeroPureWhite material has relatively good mechanical parameters, but to decide on its usefulness, more tests are needed.

The VeroPureWhite material has similar behavior and thrust force values as when drilling bones. However, in order for the comparison to be more reliable, it would be worth testing drilling at higher rotational speeds. In addition, it is necessary to check the thermal aspect. The disadvantage of the material is also the formation of chips during processing, which significantly impedes work on it.

At this moment it is not fully possible to indicate whether the VeroPureWhite material could be used for the temporal bone model intended for surgeons' training. It is necessary to perform more tests, but it has many features that provide for this, it might be appropriate.

Successors who are acquiring the results of research should focus on testing the material VeroPureWhite under dynamic conditions. In addition, they should perform drilling tests on the test material and human bone in cooperation with the surgeon, using a professional otological drill and compare the results.

Acknowledgment

I would first like to thank my thesis advisor Ph.D. Anne-Sophie Bonnet at National School of Engineers of Metz. The door to Prof. Bonnet office was always open whenever I ran into a trouble spot or had a question about my research or writing.

I would also like to acknowledge Dr Cécile Parietti-Winkler, who helped me in preparing for the project and showed me how the real surgeon's work looks like.

I would also like Ph.D. Julien Cappelle, who helped me do all the tests and took care of my safety.

Finally, I would like to thank the institution Oticon Medical-Neurelec that supported and financed the entire project.

Literature

[1] HOCHMAN J.B., KRAUT J., KAZMERIK K., UNGER J.B., *Generation of a 3D Printed Temporal Bone Model with Internal Fidelity and Validation of the Mechanical Construct,* 2014, Otolaryngology–Head and Neck Surgery, Vol. 150, pp. 448–454, DOI: 10.1177/0194599813518008

[2] OKADA D. M., DE SOUSA A.M., HUERTAS R. de A., SUZUKI F. A., *Surgical simulator for temporal bone dissection training*, Brazilian Journal of Otorhinolaryngology, 2010, pp. 575- 578, DOI: 2010;76(5):575-8

[3] BROWN A.D., WALTERS J.B., ZHANG Y.X., SAADATFAR M., ESCOBEDO-DIAZ J.P., HAZELL P.J., *The mechanical response of commercially available bone simulants for quasi-static and dynamic loading*, Journal of the Mechanical Behavior of Biomedical Materials, Vol. 90, pp. 404–416, DOI: 10.1016/j.jmbbm.2018.10.032

[4] KEAVENY T. M., MORGAN E. F., YEH O. C., *Bone Mechanics*, Chapter 8, Standard Handbook of Biomedical Engineering & Design, edited by KURTZ. M, 2004, 8.1-8.11

[5] MOORE K. L., DALLEY A. F., AGUR A. M. R., *Clinically Oriented Anatomy*, Lippincott Williams & Wilkins, 2014

[6] LUERS J. Ch., HUTTENBRINK K., *Surgical anatomy and pathology of the middle ear*, Journal of Anatomy, 2016, Vol. 228, pp. 338-353, DOI: 10.1111/joa.12389

[7] WALOCHA J., *Anatomia prawidłowa człowieka. Czaszka.* Podręcznik dla studentów i lekarzy, Wydawnictwo Uniwersytetu Jagiellońskiego, 2013

[8] PRACY R., *Congenital anomalies of the ear*, In Scott-Brown's Otolaryngology. 5th Edition, Vol. 6, Butterworth and Co. Ltd, pp. 54–64

[9] PENG T., RAMASWAMY A. T., KIM A. H., *Common Otologic Surgical Procedures Clinical Decision-Making Pearls and the Role of Imaging*, Neuroimaging Clinics of North America, 2019, Vol. 29, pp. 183-196, DOI: 10.1016/j.nic.2018.09.008

[10] LABADIE R. F, FENLON M., CEVIKALP H., HARRIS S., GALLOWAY R., FITZPATRICK J. M., *Image-guided otologic surgery,* International Congress Series, 2003, Vol. 1256, pp. 627-632, DOI: 10.1016/S0531-5131(03)00273-5

[11] BRACKMANN D, SHELTON C., ARRIAGA M., *Otologic Surgery, 4th Edition*, Elsevier, 2015, ISBN 9780323299770

[12] ACHIM V., LINKE S., DAHLMANN C., *Otoryno-layngologia*, Urban and Fischer, 2007,

[12] ZAGZOOG N., YANG V. X. D., *State of Robotic Mastoidectomy: Literature Review,* World Neurosurgery, 2018, Vol. 116, pp. 347-351, DOI: 10.1016/j.wneu.2018.05.194

[13] ZAGZOOG N., YANG V. X. D., *State of Robotic Mastoidectomy: Literature Review,* World Neurosurgery, 2018, Vol. 116, pp. 347-351, DOI: 10.1016/j.wneu.2018.05.194

[14] AGUS M., GIACHETTI A., ZANETTI G., ZORCOLO A., *Real-Time Haptic and Visual Simulation of Bone Dissection*, 2002, Vol. 12, No. 1, pp. 110-112, DOI: 10.1109/VR.2002.996524

[15] WANG H., LIN J., LEE K., TAI Ch., WANG L., CHANG H., HSU Y., CHAI Ch., HO K., *Analysis of Mastoid Findings at Surgery to Treat Middle Ear Cholesteatoma*, Otolaryngology-Head & Neck Surgery, 2006, DOI: 10.1001/archotol.132.12.1307

[16] HIRAUMI H., SATO H., ITO J., *Papercraft temporal bone in the first step of anatomy education*, Auris Nasus Larynx, 2017, Vol. 44, pp. 277-281, DOI: 10.1016/j.anl.2016.07.017

[17] DEDMON M. M., XIE D. X., OÇONNELL B. P., DILLON N. P., WELLBORN P. S., BENNERR M. L., HAYNES D. S, LABADIE R. F., RIVAS A., *Endoscopic Ear Surgery Skills Training Improves Medical Student Performance*, Journal of Surgical Education, 2018, Vol. 75, pp. 1480-1485, DOI: 0.1016/j.jsurg.2018.04.015

[18] RYAN P., WUESTHOFF C., PATEL N., *Getting started in endoscopic ear surgery*, Journal of Otology, 2018, DOI: 10.1016/j.joto.2018.10.002

[19] JAVIA L., SARDESAI M.G., *Physical Models and Virtual Reality Simulators in Otolaryngology*, Otolaryngologic Clinics of North America, 2017, Vol. 50, pp. 875-891, 2017, Vol. 50, 875-891, DOI: 10.1016/j.otc.2017.05.001

[20] GEORGE A., P. DE R., *Review of temporal bone dissection teaching: how it was, is and will be*, The Journal of Laryngology & Otology, 2010, Vol. 124, pp. 19-125, DOI: 10.1017/S0022215109991617

[21] Da CRUZ M.J., FRANIS H.W., *Face and content validation of a novel three-dimensional printed temporal bone for surgical skills development*, 2015, pp. 23-29, DOI: 10.1017/S0022215115001346

[22] https://www.phacn.de/en/hno/felsenbein/, [access: 10.03.2019]

[23]http://www.collinmedical.fr/portfolio-item/os-temporal-de-simulation-chirurgicale, [access:10.03.2019]

[24] https://www.temporalogix.com/3d-temporal-bone.html, [access: 10.03.2019]

[25] https://www.kezlex.com/en/about/, [access: 10.03.2019]

[26] https://www.temporal-bone.com/buy-temporal-bones/cat_1.html, [access: 10.03.2019]

[27] ARORA A., LAU L. Y.M., AWAD Z., DARZI A., SINGH A., TOLLEY N., *Virtual reality simulation training in Otolaryngology*, International Journal of Surgery, 2014, Vol. 12, 87-94, DOI: 10.1016/j.ijsu.2013.11.007

[28] ZIRKLE M., ROBERSON D. W., LEUWER R., DUBROWSKI A., *Using a Virtual Reality Temporal Bone Simulator to Assess Otolaryngology Trainees*, The Laryngoscope, 117:258 –263, 2007

[29] ZHAO Y.C., KENNEDY G., HALL R., LEARY *Differentiating levels of surgical experience on a virtual reality temporal bone simulator*, S. O., Otolaryngology-Head and Neck Surgery, 2010, Vol. 143, pp. 30-35, DOI: 10.1016/j.otohns.2010.03.008

[30] LESZCZYCKI T., *Wybrane zagadnienia modelowania w biomechanice kości,* Instytut Podstawowych Problemów Techniki polskiej Akademii Nauk, ISBN 978-83-89687-24-1, Warszawa, 2007

[31] https://training.seer.cancer.gov/anatomy/skeletal/tissue.html, [access: 12.03.2019]

[32] MARTIN R.B., *Determinants of the mechanical properties of bones*, Journal of Biomechanics, 1991, Vol. 24, pp. 79-88, DOI: 10.1016/0021-9290(91)90379-2

[33] SANTIUSTE C., RODRIGUEZ-MILLAN M., GINER E., MIGUELEZ H., *The influence of anisotropy in numerical modeling of orthogonal cutting of cortical bone*, Composite Structures, 2014, Vol. 116, pp. 423-431, DOI: 10.1016/j.compstruct.2014.05.031

[34] CHEN Y. J., MAFEE M. F., *Computed tomography imaging technique and normal computed tomography anatomy of the temporal bone*, Operative Techniques in Otolaryngology, 2014, Vol. 25, No. 1, pp. 3-12, DOI: 10.1016/j.otot.2013.11.002

[35] PETERSON J., GECHOW P. C., *Material properties of the human cranial vault and zygoma,* The Anatomical Record Part A: Discoveries in Molecular, Cellular, and Evolutionary Biology banner, 2003, pp. 785-786, DOI: 10.1002/ar.a.10096

[36] RAHMOUN J., AUPERRIN A., DELILLE R., NACEUR H., DRAZETIC P., *Characterization and micromechanical modeling of the human cranial bone elastic properties*, Mechanics Research Communications, 2014, Vol. 60, pp. 7–14, DOI: 10.1016/j.mechrescom.2014.04.001

[37] DELILLE R., LESEUER D. POTIER P. MARKIWEICZ E., *Experimental study of the bone behaviour of the human skull bone for the development of a physical head model*, Taylor & Francis, 2014, Vol. 12, No. 2, DOI: 10.1080/13588260701433081

[38] WOOD J. L., *Dynamic response of human cranial bone*, Journal of Biomechanics, 1971, Vol. 4, pp. 1-12, DOI: 10.1016/0021-9290(71)90010-8

[39] DAVIS T. M., LOYD A.M., SHEN H. H., MULROY M. H., NIGHTINGALE R. W., MYERS B. S., BASS C. D., *The mechanical and morphological properties of 6 year-old cranial bone*, Journal of Biomechanics, 2012, Vol. 45, pp. 2493-2498, DOI: 10.1016/j.jbiomech.2012.07.001

[40] McELHANEY A. H., F0GLE J. L., MELVIN J.W., HAYNES R. R., ROBERTS V. L., ALEM N. M., *Mechanical properties of Cranial Bone,* Journal of Biomechanics, 1970, Vol. 3, pp. 495-511, DOI: 10.1016/0021-9290(70)90059-X

[41] EVANS F. G., LISSNER H. R., *Tensile and Compressive Strength of Human Parietal Bone,* Journal of Applied Physiology, American Physiological Society, 1957, Vol. 10, pp. 493-497, DOI: 10.1152/jappl.1957.10.3.493

[42] HUBBARD R. P., *Flexure of layered cranial bone, Journal of Biomechanics,* 1971, Vol. 4, pp. 251-263, DOI: 10.1016/0021-9290(71)90031-5

[43] FALLAND-CHEUNG L., WADDELL J. N., CHUN Li. K., TONG D., BRUNTON P., *Investigation of the elastic modulus, tensile and flexural strength of five skull simulant materials for impact testing of a forensic skin/skull/brain model,* Journal of the Mechanical

Behavior of Biomedical Materials, 2017, Vol. 68, pp. 303-307, DOI: 10.1016/j.jmbbm.2017.02.023

[44] SHEN P., FENG G., CAO T., GAO Z., LI X., *Automatic identification of otologic drilling faults: a preliminary report*, THE INTERNATIONAL JOURNAL OF MEDICAL ROBOTICS AND COMPUTER ASSISTED SURGERY, Volume 5, Pp. 284-290, 2009

[45] ZALESKI K., MATUSZAK J., *Podstawy obróbki ubytkowej*, Politechnika Lubelska, 2016, ISBN: 978-83-7947-224-6

[46] LEE J., GOZEN B.A.,. OZDOGANLAR O.B, *Modeling and experimentation of bone drilling forces,* Journal of Biomechanics, Volume 45, Pp.1076–1083, 2012

[47]] SHEN P., FENG G., CAO T., GAO Z., LI X., *Automatic identification of otologic drilling faults: a preliminary report*, THE INTERNATIONAL JOURNAL OF MEDICAL ROBOTICS AND COMPUTER ASSISTED SURGERY, Volume 5, Pp. 284-290, 2009

[48] SHEN P., FENG G., CAO T., GAO Z., LI X., *An Intelligent Otologic Drill*, Journal of Otology, Volume 5, No 2, Pp. 104-110, 2010

[49] WENG, SHI Y., YANG N., YUAN X W., *Experimental analysis of drilling process in cortical bone,* Medical Engineering & Physics 36, Pp. 261–266, 2014

[50] TAI B.L., KAO Y., PAYNE N., ZHENG Y., CHEN L., SHIH A.J., 3D *Printed composite for simulating thermal and mechanical responses of the cortical bone in orthopaedic surgery*, Medical Engineering and Physics 000, Pp.1–8, 2018

[51] LEÓN O.L.D., ARROYO R.L., CASTRO R.R., VÁZQUEZ A.L., *MECHANICAL CHARACTERIZATION OF BONE ALLOGRAFTS, ENRICHED WITH MESENCHYMAL CELLS,* Complex Systems, 2017, DOI: 10.2495/DNE-V11-N4-722-730/026

[52] W. CHEN, F. LU, M. CHENG, *Test Method. Tension and compression tests of two polymers under quasistatic and dynamic loading,* Polymer Testing 21, Pp. 113-121, 2002

[53] MIECIELICA M., *Techniki szybkiego prototypowania – Rapid prototyping*, Przegląd Mechaniczny, Tom 2, 2010

[54] DIZON J. R. C., ESPERA A. H., CHEN Q., ADVINCULA R. C., *Mechanical characterization of 3D-printed polymers,* Additive Manufacturing, 2018, Vol. 20, pp 44-67, DOI: 10.1016/j.addma.2017.12.002

[55] PAJĄK E., DUDZIAK A., GÓRSKI F., WICHNIAREK R.., *Techniki przyrostowe i wirtualna rzeczywistość w procesach przygotowania produkcji,* Agencja ReklamowoPromocyjna ,,Promocja 21" sp. z o.o., Poznań 2011

[56] LIGONM S. C., LISKA R., STAMPFL J., GURR M., MULHAUPT R., Polymers for 3D Printing and Customized Additive Manufacturing, American Chemical Society, 2017, pp. 10241-10242, DOI: 10.1021/acs.chemrev.7b00074

[57] STANSBURY J. W., IDACAVAGE M. J., *3D printing with polymers: Challenges among expanding options and opportunities*, Dental Materials, 2016, Vol. 32, pp. 54-64, DOI: 10.1016/j.dental.2015.09.018

[58] GOH G. D., AGARWALA A., GOHMM G. L., DIKSHIT V., SINGM S. L., YEONG W.Y., *Additive manufacturing in unmanned aerial vehicles (UAVs): Challenges and potential,* Aerospace Science and Technology, 2017, Vol. 63, pp. 140–15, DOI: 10.1016/j.ast.2016.12.019

[59] https://www.stratasys.com/materials/search, [access: 30.05.2019]

[60]https://www.reddit.com/r/3Dprinting/comments/993wop/stratasys_material_comparison_black_fdm_nylon6/, [access: 16.03.2019]

[61] IBRAHIM D., BROILO T.L., HEITZ C., DE OLIVEIRA M.G., DE OLIVEIRA H.W., NOBRE S.M.W., DOS SANTOS FILHO J.H.G, SILVA D.N., *Dimensional error of selective laser sintering, three-dimensional printing and PolyJet models in the reproduction of mandibular anatomy*, 2009, Journal of Cranio-Maxillofacial Surgery, Vol. 37, pp. 167-173, DOI: 10.1016/j.jcms.2008.10.008

[62] L.C.HIEU, N. ZLATOV, J. V. SLOTEN, E. BOHES, L. KHANH, P. H. BINHM P.ORIS, Y. TOSHEV, *Medical rapid prototyping applications and methods,* Assembly Automation 25/4 , Pp 284–292, 2005

[63] VENTOLA C.L., *Medical Applications for 3D Printing:Current and Projected Uses*, Pharmacy and Therapeutics, 2014

[64] JARDINI A.L., LAROSA M.A., FILHO R.M., ZAVAGLIA C. Amelia de Carvahlo, BERNARDERS L.F., LAMBERT C.S., CALDERONI D.R., KHARMANDAYAN P., *Cranial reconstruction: 3D biomodel and custom-built implant created using additive manufacturing*, Journal of Cranio-Maxillo-Facial Surgery, Volume 42, Pp 1877-1884, 2014

[65] https://all3dp.com/2/3d-printing-in-medicine-the-best-applications/,[access: 16.03.2019]

[66] GIBSON I., CHEUNGM L.K., CHOW S.P., CHEUNG W.L., BEH S.L., SAVALNI M., LEE S.H., *The use of Rapid Prototyping to assist medical applications,* Association Française de Prototypage Rapide, 2004

[67] COHEN J.. REYES S. A.. *Creation of a 3D printed temporal bone model from clinical CT data*. American Journal of Otolaryngology-Head and Neck Medicine and Surgery. 2015. Vol. 36. pp. 619-624. DOI: 10.1016/j.amjoto.2015.02.012

[68] ROSE A.S., WEBSTER C.E., HARRYSSON O.L.A., FORMEISTER E.J,. RAWAL R.B..ISELI C.E.. *Pre-operative simulation of pediatric mastoid surgery with 3D-printed temporal bone models*. International Journal of Pediatric Otorhinolaryngology. Vol. 79. pp. 740-744. DOI: 10.1016/j.ijporl.2015.03.004

[69] ROSE A. S., KIMBELL J. S, C. E. WEBSTER, O. L.A. HARRYSSON, E. J. FORMEISTER, C. A. BUCHMAN, *Multi-material 3D Models for Temporal Bone Surgical Simulation,* Annals of Otology, Rhinology & Laryngology 1–9, 2015

[70] BARBER S. R., KOZIN E. D., DEDMON M., LIN B. M., LEE K., BLACK N., REMENSCHNEIDER A. K., LEE D. J., *3D-printed pediatric endoscopic ear surgery simulator for surgical training,* International Journal of Pediatric Otorhinolaryngology, 90, 113-118, 2016

[71]https://zmorph3d.com/index.php/pl/produkty/glowice/dual-extruder, [access: 20.05.2019]

[72]https://3dgence.com/double/, [access: 20.05.2019]

[73] https://www.prusa3d.com/about-us/, [access: 20.05.2019]

[74]https://www.imprimante-3d-volumic.com/en/detail-et-description-dune-imprimante-3d-volumic/982-stream-30-dual-mk2.cfm [access: 20.05.2019]

[75] https://www.raise3d.com/products/pro2-3d-printer, [access: 20.05.2019]

[76] https://ultimaker.com/en/products/ultimaker-s5, [access: 20.05.2019]

[77]https://www.3dsystems.com/3d-printers/plastic#multijet-printers-mjp,[access:20.05.2019]

[78]https://www.stratasys.com/3d-printers/objet1000-plus [access: 20.05.2019]

[79] HAFFNER M.. QUINN A.. HSIEH T.. STRONG E. B.. STEELE T.. *Optimization of 3D Print Material for the Recreation of Patient-Specific Temporal Bone Models*. Annals of Otology. Rhinology & Laryngology. 2018. Vol. 127(5). pp. 338–343, DOI: 10.1177/0003489418764987

[80] http://www.cadindus.fr/, [access: 20.05.2019]

[81] JACQUILLARD A., Analyse expérimentale du perçage de l'os, Master Thesis, ENIM, Université de Lorraine, 2015

[82] MORELLE X., *Mechanical Characterization and Physics-Based Modeling of a Highly-Crosslinked Epoxy Resin*, Université catholique de Louvain – Institute of Mechanics, Materials and Civil Engineering, 2015

[83]https://www.polymerservice-merseburg.de/en/plastics-testing/mechanical-tests/compression-test.html, [access: 10.06.2019]

[84] MUHAMAD K., HAMIRUDDIN N.A., RAZAK R.A., *Effect of Steel Fibre Contents with High Strength Fibre Reinforced Concrete*, The Journal of Scientific and Engineering Research, 2018, pp. 112-121, DOI: 10.7324/IJASRE.2018.32648

[85] AMEWOUI F., LE COZ G., BONNET A. S., MOUFKI A., *An analytical modelling with experimental validation of bone temperature rise in drilling process*, Medical Engineering and Physics, 2019 (in press)

[86] MAYEUR O., CHAARI F., HAUGOU G., DELILLE R., *Quasi-static and dynamic behaviour of the bone structures with fine geometric and materials modelling aspects*, The European Physical Journal Conferences, 2012, PP. 3-5, DOI: 10.1051/epjconf/20122603008

Figure

Tables

Annex A

N° Sample	Dimension [mm]			Cross section area [mm²]	Weight [g]	Volume [mm³]	Density [g/cm³]
	length	width	high				
X1	12.61	12.69	25.36	160.06	4.77	4058.66	1.18
X2	12.62	12.71	25.38	160.36	4.77	4069.35	1.17
X3	12.65	12.69	25.34	160.44	4.74	4065.65	1.17
X4	12.64	12.69	25.4	160.44	4.77	4074.74	1.17
X5	12.63	12.72	25.36	160.65	4.75	4074.18	1.17
X6	12.68	12.72	25.37	161.33	4.76	4092.99	1.16
X7	12.66	12.72	25.4	161.08	4.78	4090.83	1.17
X8	12.70	12.73	25.37	161.59	4.77	4098.90	1.16
X9	12.67	12.71	25.40	160.99	4.76	4089.23	1.16
X10	12.64	12.69	25.36	160.49	4.76	4069.12	1.17
Y1	12.67	12.69	25.32	160.78	4.76	4071.01	1.17
Y2	12.64	12.63	25.34	159.64	4.77	4044.83	1.18
Y3	12.66	12.63	25.51	159.9	4.77	4078.41	1.17
Y4	12.66	12.64	25.37	160.02	4.77	4059.23	1.18
Y5	12.66	12.66	25.41	160.28	4.77	4072.6	1.17
Y6	12.67	12.7	25.27	160.91	4.77	4065.63	1.17
Y7	12.59	12.67	25.28	159.52	4.76	4032.55	1.18
Y8	12.68	12.65	25.38	160.36	4.76	4069.93	1.17
Y9	12.64	12.69	25.38	160.40	4.77	4070.46	1.17
Y10	12.67	12.68	25.35	160.66	4.76	4069.124	1.17
Z1	12.64	12.64	25.38	159.77	4.77	4054.95	1.18
Z2	12.64	12.63	25.34	159.64	4.76	4044.83	1.18
Z3	12.66	12.63	25.51	159.9	4.77	4078.41	1.17
Z4	12.66	12.64	25.37	160.02	4.77	4059.23	1.18
Z5	12.66	12.66	25.41	160.28	4.77	4072.6	1.17
Z6	12.67	12.7	25.27	160.91	4.77	4065.63	1.17
Z7	12.69	12.71	25.34	161.25	4.78	4086.01	1.17
Z8	12.66	12.71	25.40	160.87	4.77	4086.54	1.17
Z9	12.67	12.76	25.43	161.63	4.76	4110.71	1.16
Z10	12.64	12.64	25.38	159.77	4.78	4055.483	1.18
Mean	12.65	12.68	25.37	160.46	4.77	4071.06	1.17

Annex B

N° Sample	Young modulus [GPa]	Peak strength [Mpa]
X1	2.54	104.92
X2	2.62	103.23
X3	2.65	99.77
X4	2.22	86.01
X5	2.28	87.60
X6	2.27	87.73
X8	2.13	105.99
X9	2.26	106.45
X10	2.25	106.68
Y1	2.76	104.94
Y2	2.79	106.00
Y3	2.68	106.68
Y4	2.55	106.12
Y5	2.5	91.98
Y6	2.22	86.65
Y7	2.22	82.06
Y8	2.73	119.87
Y9	2.40	111.46
Y10	2.41	110.80
Z1	2.62	97.88
Z2	2.79	101.27
Z3	2.62	102.21
Z4	2.52	88.94
Z5	2.32	87.61
Z6	2.32	89.32
Z7	2.86	116.49
Z8	2.52	107.37
Z9	2.41	102.46
Z10	2.51	104.52
Mean	2.50	101.03

Annex C

Questionnaire

Evaluation of the PolyJet material for the Temporal Bone Model based on a five-point Likert scale

Name: _____ PG year*: _____

Date: _____

N° Sample:_____

*The postgraduate year

Part I - Haptic feedback – Comparing 3D Printed Temporal Bone (PTB) and Cadaveric Temporal Bone (CTB) and Real Temporal Bone.

The scale includes a grade based on five levels where:

1 – unlike, 2 - very different, 3 – similar, 4 - very similar, 5 – identical

Please mark with a cross and a response to a scale of 1 to 5 (1 = unlike, 5 = identical)

1. The depth perception of the material is realistic.

   1 ☐ 2 ☐ 3 ☐ 4 ☐ 5 ☐

2. The tissue feel of the material is realistic.

   1 ☐ 2 ☐ 3 ☐ 4 ☐ 5 ☐

3. Drilling and feedback of the material are realistic.

   1 ☐ 2 ☐ 3 ☐ 4 ☐ 5 ☐

4. The application of suction and irrigation to the bone material is realistic.

   1 ☐ 2 ☐ 3 ☐ 4 ☐ 5 ☐

5. Working on the sample allows similar vibrational properties as on a cadaveric model.

   1 ☐ 2 ☐ 3 ☐ 4 ☐ 5 ☐

6. Working on the sample allows similar acoustic properties as on a cadaveric model.

   1 ☐ 2 ☐ 3 ☐ 4 ☐ 5 ☐

7. The overall similarity to CTB.

   1 ☐ 2 ☐ 3 ☐ 4 ☐ 5 ☐

Part II – General characteristics

The scale includes a grade based on five levels where:

1 – poor, 2 - some value, 3 – average, 4 – excellent, 5 – superior

Plea mark with a cross and a response to a scale of 1 to 5 (1 = poor, 5 = superior)

1. This material is suitable for the temporal bone model designed for teaching anatomy.

   1 ☐ 2 ☐ 3 ☐ 4 ☐ 5 ☐

2. This material is suitable for the temporal bone model as an overall training tool.

   1 ☐ 2 ☐ 3 ☐ 4 ☐ 5 ☐

3. This material is "safe" in the temporal bone laboratory in comparison to the cadaveric temporal bone.

   1 ☐ 2 ☐ 3 ☐ 4 ☐ 5 ☐

4. While working with the bone simulating material. simulated bone dust was formed

   Yes ☐ No ☐

5. If simulated bone dust was generated during work. it caused any irritation (skin. lungs. membranes. mucous. eyes) in comparison to a cadaveric temporal bone.

   Yes ☐ No ☐ No bone dust ☐